EPFL

Additive manufacturing of ceramics by two-photon lithography, volumetric 3D printing and high-resolution endo-printing.

Présentée le 11 mars 2022

Faculté des sciences et techniques de l'ingénieur
Laboratoire de dispositifs photoniques appliqués
Programme doctoral en photonique

pour l'obtention du grade de Docteur ès Sciences

par

Georgia KONSTANTINOU

Acceptée sur proposition du jury

Prof. A. Radenovic, présidente du jury
Prof. C. Moser, directeur de thèse
Prof. P. Colombo, rapporteur
Prof. C. Liberale, rapporteur
Prof. Y. Bellouard, rapporteur

■ École
polytechnique
fédérale
de Lausanne

2022

Acknowledgements

I would like to thank my thesis director, Professor Christophe Moser for believing in me and giving me the opportunity to do this PhD in his lab. I would like to thank him for his encouragements, support and continuous discussions during these five years.

I would also like to thank Professor Demetri Psaltis for the collaboration and help. Additionally, I would like to thank Professor Juergen Brugger for the fruitful discussions in the ceramic meetings. I take the opportunity to thank the postdocs Dr. Boniface, Dr. Loterie, Dr. Sasikumar, Dr. Morales, Dr. Deng, Dr. Wang, Dr. Clement, Dr. Jang, Dr. Nianias, Dr. Makowska and Dr. Blugan for the help during my PhD. Special thanks to a former colleague and friend, Dr. Kakkava about the fruitful discussions all these years.

Many thanks to my office mates, Babak, Chiara, Jorge, Enrico, Emilio, Andreas and Zahra for the amazing environment. And to all the LAPD members for the great moments, Max, Roberto, Manon, Damien, Dino, Paul, Jan, Harry, Timothé, Gael, Mathieu and Matthieu, Laura, Qianyi, Leo, Ugur, Ilker, Ulas and Mustafa. Special thanks to Sabrina for the administrative support. Thanks to the members of Laboratory of Optics of Professor Psaltis, Eirini, Giulia, Ye, Pooria, Ahmed, Navid, Steven, Amir, Kyriakos, Joowon, Sylvain, Elizabeth and Marilisa for the time we spent together. Special thanks to Lorenz from the Microsystems Laboratory I and to my good friends Eirini Tagkoudi and Iliana Spartali for the fun we had all these years.

Many thanks to the members of my thesis committee, Prof. Radenovic, Prof. Bellouard, Prof. Colombo and Prof. Liberale for reviewing my work.

Finally, I would like to thank my friends in Greece for their continuous support, my brother and of course special thanks to my parents for the encouragement.

Lausanne, 16th November 2021   Maya

There is a crack in everything, that's how the light gets in

Leonard Cohen

To my parents

Abstract

Additive manufacturing is a growing sector of industrial production that allows the fabrication of parts with complex geometries and reduced waste. The context of this thesis is light-based additive manufacturing technologies.

In the first part of the thesis, we explore the micro-fabrication of a highly viscous, preceramic resin with a commercially available two-photon 3D-printer. The micro-additive manufacturing of ceramics with a preceramic polymer formulation was successfully achieved. We report on the printing parameters of the preceramic polymer and pyrolysis conditions that ensured a ceramic conversion with minimum deformation and shrinkage without cracks and porosity.

In the second part of the thesis, a complete set-up of a fiber endo-printer is presented that yields smooth objects with submicrometer lateral resolution. We introduce a transmission matrix method for scanning and tuning the size of the focused spot and adjust the fabrication speed. We include an exposure dose correction, which significantly improves the surface quality of the print.

In the third part of the thesis, we explore centimeter scale fabrication of a preceramic resin formulation with a volumetric tomographic printing technology that allows to produce support-free, complex shapes, more challenging to produce with a conventional layer-by-layer printing technology. We report on the details of the pre-processing and post-processing steps, including formulation protocol, printing parameters and pyrolysis step that produces a high-fidelity ceramic object.

Keywords

Additive manufacturing, 3D printing, ceramics, preceramic polymers, two-photon polymerization, wavefront shaping, optical fibers, digital holography, transmission matrix

Résumé

La fabrication additive est un secteur en pleine expansion de la production industrielle qui permet de fabriquer des pièces aux géométries complexes et de réduire les déchets. Le contexte de cette thèse est celui des technologies de fabrication additive basées sur la lumière.

Dans la première partie de la thèse, nous explorons la micro-fabrication d'une résine précéramique hautement visqueuse avec une imprimante 3D à deux photons disponible dans le commerce. La fabrication micro-additive de céramiques avec une formule de polymère précéramique a été réalisée avec succès. Nous rapportons les paramètres d'impression du polymère précéramique, les conditions de pyrolyse qui ont assuré une conversion céramique avec un minimum de déformation et de rétraction sans fissures et porosité.

Dans la deuxième partie de la thèse, nous présentons la mise en place complète d'une endo-imprimante à fibre qui produit des objets lisses avec une résolution latérale submicrométrique. Nous introduisons une méthode de matrice de transmission pour balayer et régler la taille du point focalisé et ajuster la vitesse de fabrication. Nous incluons une correction de la dose d'exposition qui améliore considérablement la qualité de surface de l'impression.

Dans la troisième partie de la thèse, nous explorons la fabrication à l'échelle centimétrique d'une formulation de résine précéramique avec une technologie d'impression tomographique volumétrique qui permet de produire des formes complexes impossibles à réaliser avec une technologie d'impression conventionnelle couche par couche. Nous présentons les détails des étapes de prétraitement et de post-traitement, y compris le protocole de formulation, les paramètres d'impression et l'étape de pyrolyse qui produit un objet en céramique de haute fidélité.

Mots-clés

Fabrication additive, l'impression 3D, céramique, polymère précéramique, polymérisation à deux photons, adaptation de front d'onde, fibre optique, hlographie digitale, matrice de transmission

Contents

List of Figures

List of Tables

List of Equations

Chapter 1   Introduction

Additive manufacturing (AM) or three-dimensional printing (3D printing) is a computer-aided process, which creates 3D objects by depositing the material layer-by-layer and it is known for almost 40 years in its modern implementation. Dr. Hideo Kodama invented the first light-based 3D printer (VAT photopolymerization) and his work was published in 1981 [1], [2]. However, it was Charles W. Hull (CTO of 3D Systems Corp.), who saw the commercial potential and independently developed the same idea. He was granted a patent in 1986, in which he coined the name "stereolithography", still in use today. The first commercial 3D printer was released in 1988 [1]–[3]. In Figure 1.1, the first commercial 3D printer is presented along with the first object fabricated with this 3D printer.
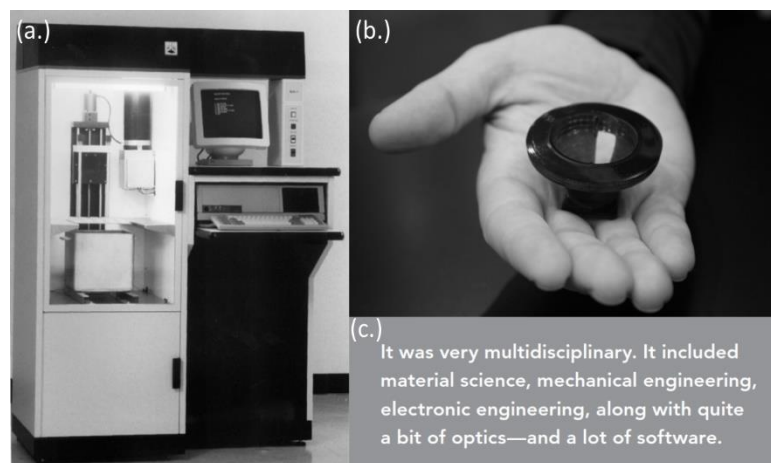
Figure 1.1 : (a.) The first stereolithography 3D printer, SLA 1, (b.) The first 3D printed part fabricated by the same 3D printer, (c.) Charles W. Hull text, source for a, b, c: [3]

In this light-based 3D printing technology, the object is built layer-by-layer by solidification of a UV curable material in liquid form upon ultraviolet light exposure for a certain amount of time.

The feedstock in AM depends on the technology and it can be liquid polymers, alloys, metals, powders, thermoplastic materials, glass, types of ink, composites etc. In Stereolithography (SLA) and Digital Light Processing (DLP), the resin gets solidified upon exposure to UV-light (Vat photopolymerization) due to its photosensitivity. In Selective Laser Sintering (SLS), which is a Powder Bed Fusion process, a high-power laser fuses the powder onto the powder bed. In Fused Deposition Modeling (FDM), the nozzle extrudes a heated thermoplastic material and in 3D Inkjet Printing (3DIP), cartridges (inkjet-heads) jet the ink on specific positions of the bed to be cured by the light [4]–[6]. In Figure 1.2, we present the 3D printing technologies depending on the feedstock. This illustration is a simplified version of the AM map by 3dpbm [7].
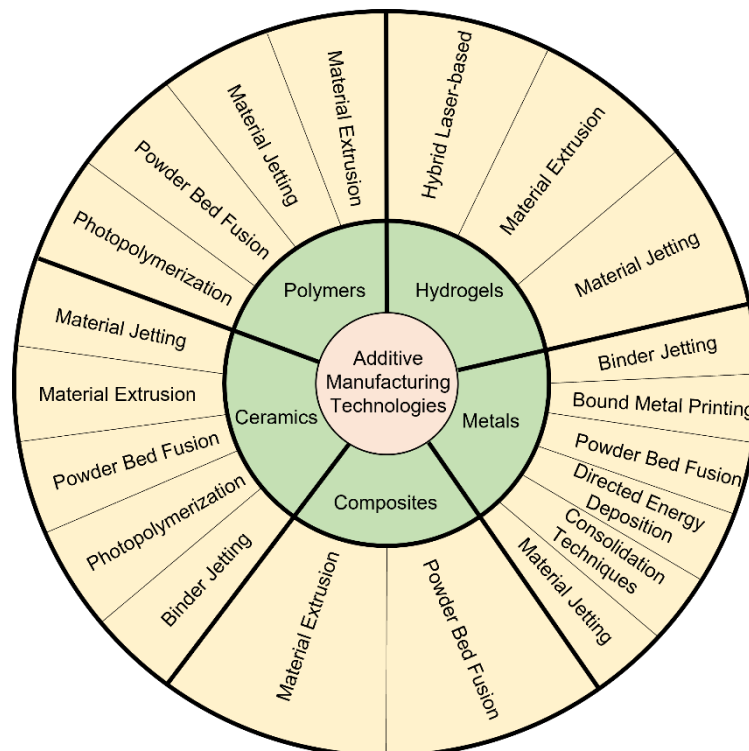
Figure 1.2: AM technologies for each kind of feedstock. Simplified by the AM map by 3dpbm [7].

Shape fidelity or sometimes-called shape accuracy is defined by the comparison between the morphology of the printed part and the digital model. The spatial resolution is related to the minimum feature size of the print. Both parameters are important in AM. The range of resolution starts from approximately 300 nanometers to 250 micrometers and depends on the technology [8], [9].

The main advantages of AM technologies are: a) design of complex parts, b) rapid prototyping and design iterations in a more efficient rate, c) customization and print-on-demand, d) low-cost prototyping, e) ease of access and f) environmentally friendly by reduced waste and stock. On the other hand, there are limited materials that can be used in AM, the build volume of the part is restricted, the post-processing steps are often challenging and it is also quite possible that design inaccuracies occur.

Applications have been expanded to several fields of the industrial sector such as aerospace, automobile, machine tool production, healthcare and medical, dentistry and dental technology, architecture, construction, food or even production of diamonds [10]–[14]. A good review of applications is also given in [8], [15]. It is expected that the development of AM technologies is leading to the fourth industrial revolution in which mass customization occurs, consumers can become producers and 3D printing will diffuse in specific industrial sectors as well [16]–[18]. Decentralized manufacturing and on-demand manufacturing can lead, as it was mentioned above, to environmental benefits, for example better control regarding the products in stock, better usage of feedstock and lower energy consumption in industry [19]–[21]. Plastic, metal and polymer-based printed objects are the most common materials encountered in 3D printers but there is a wider range of materials that can be used [8]. An important class of materials, ceramics, has comparatively received less attention in AM [22].

1.1   Motivation for this thesis' work

Ceramics are materials widely used in industry. For instance, cardiac, nerves or brain electrodes, used in medical industry, can be modified and improved by replacing traditional materials with ceramics [23]–[25]. For instance, fibrosis is often observed in medical devices such as pacemakers with metal electrodes after a certain period. It is caused by tissue inflammation that creates a layer of scar tissue at the electrode and this reduces the electrical performance of the device. Conductive ceramics have been proposed as an alternative option that reduces fibrosis [26]. Other features of ceramics such as their performance at high-temperatures (thermal insulators) and acidic environments (filters) in combination with the previously mentioned benefits of AM technologies, are additional reasons that several AM technologies are being

developed to fabricate ceramic components [27], [28]. In this work, we investigate the use of two light-based technologies: 1. two-photon polymerization and 2. volumetric 3D printing to produce crack-free and low-shrinkage 3D objects with sub-micrometric resolution at the micrometer scale and micrometric resolution at the centimeter scale respectively. We investigated the protocols for the preparation, printing and pyrolysis of a commercially available preceramic resin.

Secondly, we explore the use of two-photon 3D printing via endoscopy. Endo-fabrication demonstrated by Morales et al. [29] in our group allowed fabrication in inaccessible areas such as in the body by using an optical fiber. Endoscopic surgery has been already used for cases such as endometriosis, endonasal approach etc. Optical fiber probes could be also used for 3D printing in parallel photonic wire bonds in inaccessible areas on a photonic integrated circuit (PIC). Due to their thin diameter, typically 50 to 100 µm, a multimode optical fiber can be inserted to deliver focused light to either perform ablation or to print by photopolymerization [29]–[32]. Due to the light scrambling in a multimode fiber, a spatial light modulator must be used to modulate the wavefront in order to focus and scan a spot at the output of the fiber. The work presented in [29] was limited in resolution, speed and flexibility as will be explained in more details. My work goes a step further by providing a major improvement in terms smoothness (200 nm step instead of 1 µm) and printing speed (5 times faster).

This thesis is organized as follows: In this introduction chapter, light-based additive manufacturing technologies used for the fabrication of ceramic components are reviewed. The two-photon polymerization mechanism is introduced for the fabrication of micro-structures out of a photosensitive resin. The digital control of a femtosecond laser light beam through a multimode optical fiber is explained and lastly a new novel single-photon Volumetric 3D printing technology is presented. Overall, three different light-based technologies are investigated in this thesis. The formulation of a preceramic polymer was first tuned to a 2-photon printer and then adapted to a volumetric 1-photon printer. The performance of the fabricated parts was evaluated and compared.

My work explores two-light based AM technologies using a pre-ceramic polymer formulation in Chapter 2 and Chapter 4 and secondly explores the limits of an endoscopic micro-fabrication AM technology using photopolymers in Chapter 3. Specifically, the work of this thesis focuses on micro (µm) and macro (cm) -scale additive manufacturing by photopolymerization, using commercially available

preceramic resins, which show exceptional properties once pyrolysed (Chapter 2 and Chapter 4). In Chapter 3, the thesis focuses on microadditive manufacturing of polymers through a multimode optical fiber for printing in inaccessible areas.

In the first part, I fabricated ceramic structures using a two-photon 3D printer and a newer technology called volumetric 3D printing by reverse tomography, which is a single photon printing process. I investigated the preprocessing and applied post-processing protocols, which are necessary for the success of the printing step in two-photon and volumetric 3D printing of ceramics as well as the polymer to ceramic conversion.

In the second part, I built an endoscopic fiber-based 3D printer and used it to fabricate smooth 2D and 3D micro-structures. This work focused on a) printing high-resolution microstructures and b) printing faster by point-spread function engineering. In Figure 1.3, the three AM technologies, used in my thesis, are illustrated along with a printed object obtained from each 3D-printer.
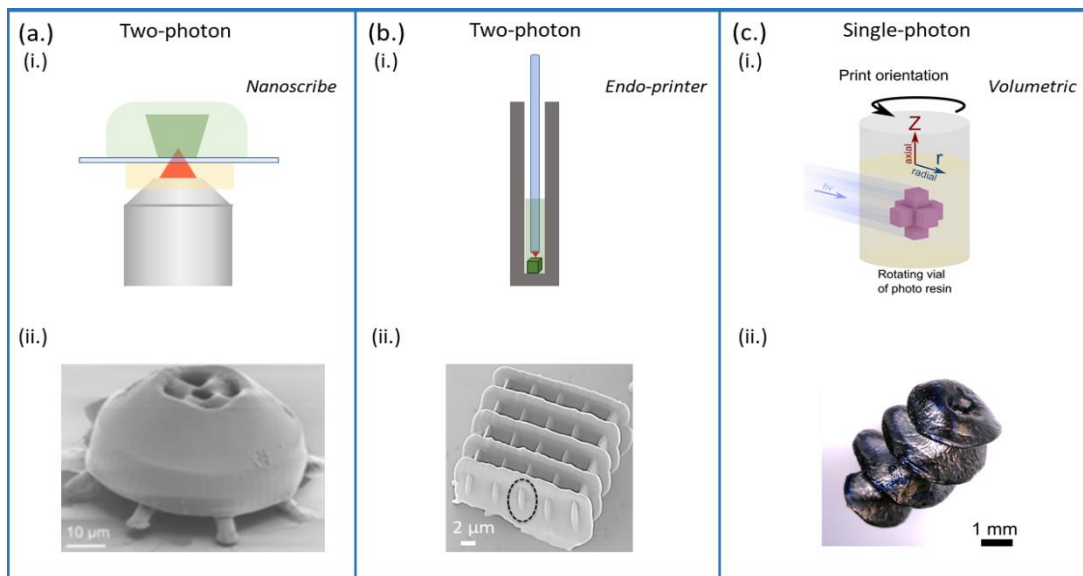
Figure 1.3: (a.i) 3D printing with an objective lens, oil-immersion configuration of the Nanoscribe 3D printer is illustrated, (a.ii) SEM image showing the fabricated pyrolysed part, (b.i) Illustration of a two-photon endoprinter highlighting the access to confined areas, (b.ii) The fabricated part is presented with one voxel highlighted, (c.i) The Volumetric 3D printer is illustrated showing the rotating vial, (c.ii) A 3D-printed and pyrolysed mm-scale object is presented.

1.2 Light and polymer-based additive manufacturing of ceramics

1.2.1 Ceramics

The word "ceramic" is a noun and adjective and comes from the Greek word "κεραμεικό", which means "pottery". Consequently, it is used to attribute the type of material used for the referred "pottery" object. That material, in some cases, has properties similar to the ones used in the past for potteries [33], [34]

Ceramics are solid compounds, and they consist of non-metallic, metallic and inorganic components. They are formed by applying heat or heat and pressure and can be amorphous but are typically crystalline in nature. They belong to one of the three large classes of solid materials along with metals and polymers and are formed by bonds, which are strong ionic or covalent. Ceramics are microstructure-dependent, a grain in a ceramic part can be from 1 to 50 mm. The size, the shape, the presence or absence of porosity, the ceramic phase, the grain boundaries and the distribution of the grains, along with all the above, explain the fact that the class of ceramics has this diversity of superior properties.

Ceramics are hard, brittle, refractory, prone to thermal shock, wear-resistant, electrically, and thermally insulative, chemically inert, non-magnetic and usually oxidation-resistant. However, because of this microstructure-dependence, the above generalization can have exceptions as well. Correspondingly, the range of applications of ceramics is wide depending on the desired properties.

For instance, ceramics are being used as filters for the purification of exhaust gases (zeolites), as cutting tools, as ferrules for optical fibers, as corrosion-resistant materials for Sodium lamps, as windows (soda-lime glasses) and as substrates for electronic packaging and electrical insulators in general. For nuclear applications, they are used as fusion reactor linings and as heating elements for furnaces.

The raw materials for shaping ceramics can be powders, polymer fibers, volatile molecules and preceramic polymers. In the next paragraph, we focus on preceramic polymers, which then results in polymer derived ceramics after pyrolysis [34]–[36].

1.2.2   Polymer Derived Ceramics (PDCs)

The production of ceramics from molecular precursors was firstly reported in the early 1960s by Verbeek and Yajima [37], [38] . Polymer derived ceramics are silicon-based ceramics, fabricated from preceramic polymers (PCPs), which are used as precursors. The PDCs are usually amorphous, and they can include silicon carbide, silicon oxycarbide, silicon nitride and silicon oxynitride. The preceramic polymer can be cured thermally or upon light exposure to obtain solidification. The resulted solid part is called a green body or green part.

The composition, the number of phases, the phase distribution and the microstructure of the final PDC depend on the molecular structure and the type of the preceramic polymer. For this reason, the final physical and chemical properties of the fabricated PDCs can be varied and tuned by the design of the molecular precursor, which affects the ceramic yield.

A simplified molecular structure of an organosilicon polymer, which can be used as a precursor for the synthesis of ceramics is presented, in Figure 1.4. On the molecular level, the group X of the polymer backbone and the substituents R1 and R2 (functional groups), which are attached to silicon, can be selected to design the preceramic compound. The variety of group X explains the different classes of silicon-based polymers, for instance poly(organosilanes), poly(organocarbosilanes), poly(organosiloxanes), poly(organosilazanes) and poly(organosilylcarbodiimides). Different functional groups result in different final properties [39].

$$\left[\begin{matrix} R^1 \\ | \\ Si-X \\ | \\ R^2 \end{matrix} \right]_n$$
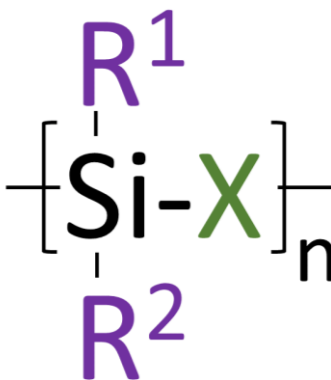
Figure 1.4: Example of the polymer backbone of a pre-ceramic polymer illustrating the variety of possible functional groups attached to the silicon atom

1.2.3   Additive Manufacturing of ceramics

Here, we describe the AM technologies used for the fabrication of ceramic parts. Selective Laser Sintering (SLS), three-dimensional printing (3DP), Selective Laser Melting (SLM), Fused Deposition Modeling (FDM), Laminated Object Manufacturing (LOM), Direct Inkjet Printing (DIP) and many other AM technologies are being used for shaping ceramic parts by using different types of feedstocks, in solid, liquid or powder form [22], [40]–[42].

Liquid-based AM technologies include photo-polymerization, material jetting and extrusion methods. In VAT photopolymerization, the object is built by polymerizing a photocurable material. More specifically, in Digital Light Processing (DLP), each layer is printed at once with a projected pattern from a digital micro-mirror device (DMD). The building plate moves upwards (or downwards) a few micrometers, allowing the unexposed liquid to flow again inside the area of interest and the next layer gets solidified upon the next light exposure. In Stereolithography (SLA), the difference is that the laser beam is scanned point by point to produce a layer. The shape of the part, for both technologies, is determined by layered construction [43]–[46]. In Figure 1.5.a, a simplified scheme of a DLP printer is presented [47] and in Figure 1.5.b and c the Lithoz light-based 3D printing system is shown with some examples of ceramic 3D printed objects [41].
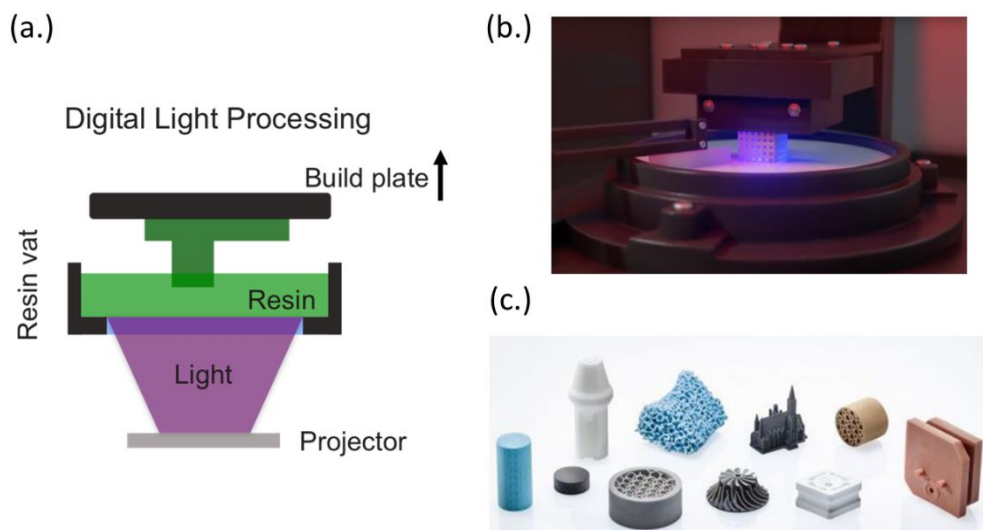
Figure 1.5: (a.) Simplified illustration of a Digital Light Processing 3D printer, (b.) Lithoz UV-based 3D printer using PCP material, c.) printed and pyrolysed 3D objects by Lithoz.

The final polymer derived ceramic (PDC) occurs after the pyrolysis step. At that step, the green body is inserted in an oxygen-free furnace which can reach high temperatures, usually above 800 °C. An inert atmosphere is used to avoid combustion and create a successful polymer to ceramic conversion [39], [49]. However, for green bodies, it is also possible to fire in air in order to obtain advanced oxide ceramics.

1.3   Two-photon lithography

1.3.1   Basic concepts

Optical Susceptibility

The interaction between electromagnetic radiation of light (visible and near-Infrared (IR) light) and matter results in the oscillation of the electrons of the atom, that follow the applied electric field of the light. In the semi-classical view, the electrons are bound to the nucleus thanks to the electrostatic potential (approximated as harmonic function), and they are displaced from their position of "rest" by the Coulomb force generated by the electric field of the light. The latter induces an electric dipole moment.

The contribution of the many dipoles introduces the macroscopic term of the electric polarization $P(t)$:

$$e.\ 1: \quad P(t) = \varepsilon_0[\chi^{(1)}E(t) + \chi^{(2)}E^2(t) + \chi^{(3)}E^3(t) + \cdots]$$

where ε_o is the vacuum electric permittivity, $\chi^{(n)}$ is the nth order non-linear optical susceptibility, and each product is the nth order polarizability. If the applied electric field is weaker than the electrostatic potential, only the first term is contributing (linear optical phenomena). For a stronger applied field, this dependence becomes non-linear and the electron cloud moves further from the equilibrium position, where the binding potential is no more harmonic. The imaginary parts of the odd-order susceptibilities ($\chi^{(3)}$ and $\chi^{(5)}$) describe the non-linear absorption of photons (two-photon and three-photon absorption respectively) [50].

Two-photon absorption

Two-photon absorption is a nonlinear process for which the atom absorbs two photons of half-energy ($\Delta E=E_1+E_2$) simultaneously. Because of this absorption, the valence electron is excited from its ground state to a higher energy state and that specific energy gap ΔE is larger than the energy of each absorbed photon. For this to be achieved, the two photons must be absorbed by the atom within 1 femtosecond of each other.

This is the reason an ultrafast focused laser beam is required since it can produce a high number of photons in a small surface. For example, 5×10^8 photons are produced in a single pulse for a light beam with average power 10 mW, 80MHz repetition rate and 100 fs duration. In two-photon absorption, the rate of the energy absorption is proportional to the square of the field intensity I [51].

$$e.\ 2: \qquad \frac{dE}{dt} = \frac{8\omega\pi^2}{c^2n^2}I^2 Im[\chi^3]$$

where E is the absorbed energy, t is the time, ω denotes the frequency of the photons, c is the speed of light, n is the refractive index of the medium, I is the light intensity and $\chi^{(3)}$ is the third-order nonlinear susceptibility. This square dependence on the light intensity explains that the absorption of light is localized in a tiny volume in the proximity of the focus of light beam.

When the light beam is focused into a photopolymer, containing a molecule that can be excited by TPA, the nonlinear absorption leads to the production of a so-called "free radical". The free radicals are capable of "cutting" specific chemical bonds of the monomers and oligomers to produce a radical-ended monomer that can be linked to other monomers via a chain reaction.

After a certain fraction of chemical bonds have been consumed, there is a phase transition from liquid to solid [52] . This process is initiated by two-photon absorption of the photoinitiator and the subsequent local polymerization of the resin creates a 3D solid structure by scanning the focus spot. Hence, the technique is referred to as 2 photon polymerization (2PP).

Photosensitive resins for 2PP contain a photo-initiator, a monomer or an oligomer (molecule which consists of a few monomers) and optionally inhibitors or photosensitizers. The addition of inhibitors aims to prevent uncontrolled polymerization and the use of photosensitizers aims to improve the sensitivity of the resin to specific wavelengths. Figure 1.6 illustrates the classic difference between single and two-photon absorption.
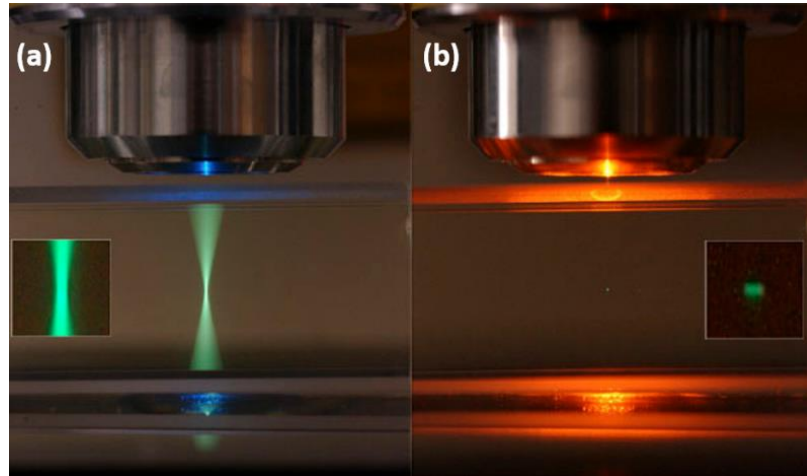
Figure 1.6: (a.) single-photon absorption, (b.) two-photon absorption (TPA). The fluorescence emitted is due to a photoactive solution. Source: Image by SteveRuzin and Holly Aaron, UC Berkeley [53]

The resolution of a printed structure is determined, by the smallest optical spots that can be generated (Abbe diffraction limit) according to the following formula:

$$e.\ 3: \quad R = \frac{\lambda}{2NA} = \frac{\lambda}{2n sin\theta}$$

Where, lambda λ is the wavelength of the light and NA is the numerical aperture of the lens focusing the light and n is the refractive index of the material. Additionally, the resolution also depends on the kinetics of the chemical polymerization process. The combination of both yields the minimum feature size that can be printed (voxel).

Ultra-short pulses for multiphoton phenomena

Multi-photon phenomena require high light intensity as mentioned above. In continuous laser (CW) sources parameters such as optical power, intensity and

energy remain constant in time. In a pulsed wave, the electric field only exists during the duration of the pulse and is zero in other times. So, for equivalent average power, a pulse laser has a higher power during the pulse than a CW laser. The peak power is inversely proportional to the pulse duration as Figure 1.7 illustrates.

The shortest pulse duration is achieved in mode-locked lasers. Instead of delivering a single pulse, mode-locked lasers deliver a stream of periodic pulses. The time between two consecutive pulses (period T) is given by the length of the laser cavity L (T=2L/c), where c is the speed of light. The inverse of the period is called the repetition rate of the cavity. In typical femtosecond lasers, the cavity is approximately 2 meters giving rise to a repetition rate of 80 MHz (12.5 ns period).
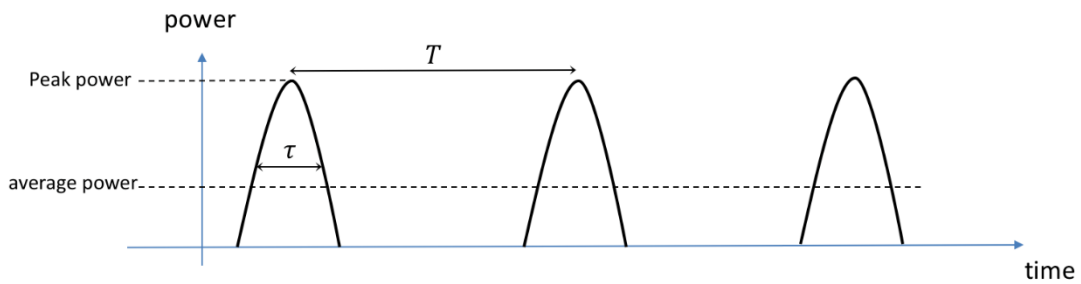
Figure 1.7: A mode-locked femtosecond laser produces a stream of period pulses of duration tau and period T. The peak power of a single pulse is related to the average power by *e. 4*.

$$e. \ 4: \ P_{peak} = P_{av} \cdot \frac{T}{\tau}$$

The mechanism for forming the pulses is related to locking the phase of all the oscillating modes in a laser cavity. The number of optical modes that can lase is proportional to the spectral width of the gain curve. Naturally, the minimum pulse duration is inversely proportional to the number of oscillating modes, which is proportional to spectral width of the gain curve. [50], [54]

Thanks to the high intensity that can be generated by focusing a femtosecond pulse, a relatively modest average power can be used (typically 10-50 mW) and consequently the deposited heat is low to minimize heat effects. Two-photon polymerization hence yields high-resolution microstructures.

1.3.2 State of the art

Following the TPA mechanism discovered first by Maria Goeppert-Mayer in 1931, who received the Nobel prize for this discovery in 1963, it was only 27 years later, in 1990 that the first application of TPA, two-photon imaging, was demonstrated [55]. A few years later, in 1997, three-dimensional microfabrication by two-photon polymerization was demonstrated by Kawata et al. A light beam from a Titanium sapphire mode-locked femtosecond laser operating at 790 nm with a pulse width of 200 fs was focused into a photosensitive resin through an objective lens of numerical aperture 0.85. This resulted in the initiation of the polymerization by radical generation after the absorption of two near-IR photons. The sample was scanned by using a stage under computer control. The structure was observed from the side of the resin with another objective lens of NA 0.4. When the fabrication was completed, the sample was washed with a solvent and all the liquid and unexposed resin was removed [56], [57].

The optical resolution is defined by the equation (e.3). However, in 2009 Fourkas et al. presented structures with $\lambda/20$ printing resolution inspired by stimulated emission depletion (STED) fluorescence microscopy. In STED, fluorescent molecules are first excited by a focused short laser pulse. A second longer wavelength laser pulse de-excites the excited molecules using a doughnut shaped beam around the first focused spot by stimulated emission. This depletion pulse arrives after vibrational relaxation is completed in the excited state and right before significant fluorescence occurs. In this way, the phase shaping of the doughnut-shaped depletion beam causes de-excitation everywhere except in a region at the center of the original focal volume. The size of this region depends on the intensity of the depletion beam and on the degree of saturation of the stimulated emission. The structures were printed with a higher printing resolution but at the cost of a second beam [58].

A higher spatial resolution can also be achieved by utilizing the nonlinear dose response of the material. In addition, the use of inhibitors such as TEMPO or oxygen controls the radical generation, which yields to a lower voxel size [59].

1.4 Digital control of light in an optical fiber

1.4.1 Basic concepts

Optical fibers and propagation of light

An optical fiber has typically a cylindrical shape and consists of the central core surrounded by a cladding layer and sometimes a protective jacket layer. The refractive index of the core is slightly higher than the refractive index of the cladding. This refractive index difference is important because it ensures light propagation inside the fiber core by total internal reflection. Depending on the size of the core, the index contrast and the wavelength of light, optical fibers can guide a single mode or multiple modes.

In this work, we are interested in multimode fibers (MMF). These fibers support many optical modes. MMF are further categorized as step-index and graded-index and this categorization is related to the shape of the refractive index inside the core. For a step-index multimode fiber, the refractive index is constant inside the fiber-core and makes an abrupt change with the refractive index of the cladding. For a graded-index multimode fiber (GRIN MMF), the refractive index forms a parabolic profile with the highest index value in the center of the core [60], [61]. In Figure 1.8, we illustrate (a) the two groups of MMF and (b) the light propagation in both groups by total internal reflection.
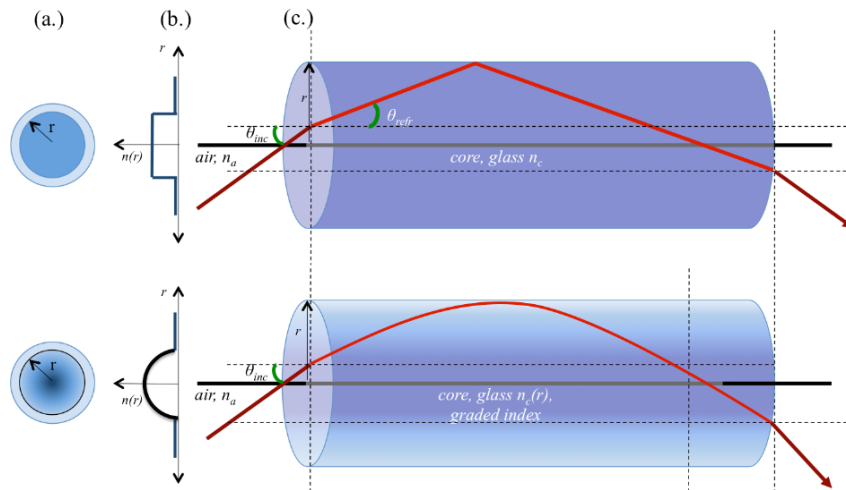
Figure 1.8: (a.) cross section of a (top) step-index and (bottom) graded-index MMF, (b.) n(r): refractive index profile vs fiber radius (c)total internal reflection (top) step-index and (bottom) graded-index MMF.

Important parameters for characterizing an optical fiber are: (a) The relative core-cladding index difference Δ and the V parameter which is related to the number of modes supported by the fiber.

$$e.\ 5: \quad \Delta = \frac{n_c - n_{clad}}{n_c}$$

$$e.\ 6: \quad V = k_0 * r * (n_c^2 - n_{clad}^2)^{1/2}$$

where $k_0 = 2\pi/\lambda$, r is the core radius, λ is the wavelength of light and the last term in brackets which is in square root represents the numerical aperture (NA) of the fiber. The number of modes M that can be supported in a MM fiber is given by the approximate expression (for V >>1): M= V^2/2. For a graded-index MMF, the rays are illustrated curved because of the gradual change of the refractive index [50].

Modal scrambling

In a homogeneous medium, the propagation of a plane wave has a constant direction. In the case of inhomogeneous medium, the refractive index is not constant everywhere which changes the light direction at each scattering event. This phenomenon causes randomization of the polarization, phase and amplitude (if there are absorbers) as well. Consequently, at the exit of the medium, the sum of all the scattered fields yields a so-called speckle pattern of light [62].

Similarly, we observe a speckle pattern at the output of a multimode optical fiber (Figure 3.5). The reason for that is that, at the entrance facet of a MMF, the light field is decomposed into the modes of the fiber. The electric field of a mode is a solution of the Helmholtz equation and is written as a spatial amplitude that depends on the radial direction and azimuthal angles in cylindrical coordinates. After propagating a length L in the fiber, at the exit of the fiber, the resulting electric field is the sum of all the modes (field component).

$$e.\ 7: \ \mathrm{E}_{out}(\mathbf{x}, \mathbf{y}, \mathbf{t}) = \sum_{l=1}^{M} a_l J_l(k_T r) e^{il\varphi} e^{-i\beta_l L} e^{i\omega t}, \text{ r<a } [50]$$

Due to the different propagation constants and some coupling between modes that occur due to scattering impurities in the fiber, the resulting superposition resembles

a speckle pattern [60]. The bright and dark areas in the speckle pattern is the result of constructive and destructive interference.

The spatial pattern at the input of the MMF loses its original spatial shape along the propagation path because of different propagation constant of the modes. A "collateral" effect, related to time is that the group velocity depends on the propagated mode or in other words different fiber modes travel with different group velocities. If a short pulse is sent at the input of the fiber, the pulse duration is increased after propagation through the multimode fiber. The modal dispersion in a MMF is typically much larger than the chromatic dispersion. When a short pulse is used, the speckle pattern at its output has less contrast than in a longer pulse because its coherence length is shorter.

Off- axis holography and Wavefront shaping in optical fibers

The word holography originates from the Greek word ολογραφία (< όλος+γράφω) and it means "recording of the whole". In physics, it was Gabor who began his experiments in holography at the Research Laboratory of the British Thomson-Houston Company before 1947. His setup was based on a two-step lensless imaging process. In a first step, he recorded an interference pattern photographically. This pattern was the result of the sum of the scattered quasi-monochromatic source of the object with the unscattered beam (reference wave). The second step is the reconstruction of the image, which is accomplished by illuminating the recorded photo with the reference wave. The image (and its twin) is the result of the diffraction of light by the photographic plate [63].

In digital off-axis holography, the interference (hologram) is recorded, not by film like in Gabor's case, but with a digital camera (Figure 1.9). To record a digital hologram, the light is also split into two arms by a beamsplitter. One of the arms illuminates the object (object arm). The light scattered by the object is directed towards a camera. The second (reference beam) is directed on the camera sensor at an angle with respect to the object beam. This is the so-called off-axis geometry. Both waves interfere at the camera plane. The interference pattern is recorded as an intensity pattern by the camera. The intensity pattern is the square of the sum of the electric field of the two waves:

$$e.\ 8:\ I(x,y) = |E_O(x,y) + E_R(x,y)|^2$$

which results in

$$I(x,y) = E_R(x,y)E_R^*(x,y) + E_0(x,y)E_0^*(x,y) + E_R(x,y)E_0^*(x,y) + E_0(x,y)E_R^*(x,y)$$
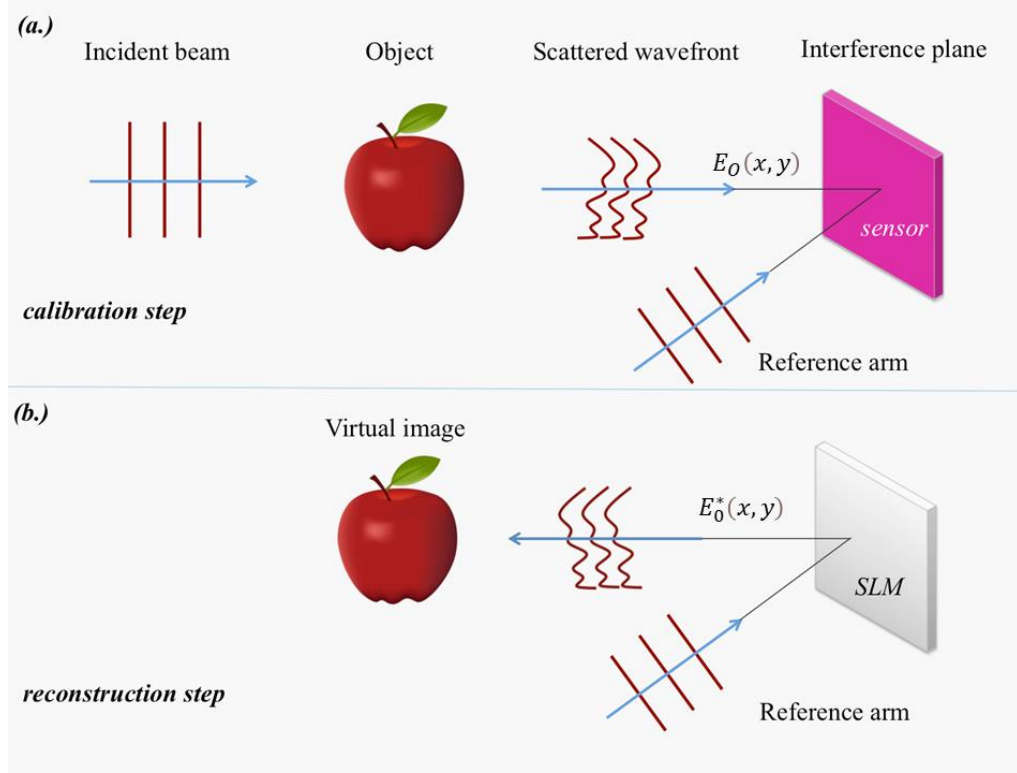
Figure 1.9: (a.) calibration step, (b.) reconstruction step

If this intensity was recorded on a film, the conjugate of the reference wave $E_R^*(x,y)$ would be used to reconstruct the object i.e:

$$E_R^*(x,y) \cdot I(x,y) = E_R(x,y)[E_R^*(x,y)]^2 + E_R^*(x,y)E_0(x,y)E_0^*(x,y) + E_0^*(x,y) + E_0(x,y)[E_R^*(x,y)]^2$$

The term $E_0^*(x,y)$ is the conjugate of the object beam. It is propagating "backwards" and reconstructs a virtual image of the object at the original place of the object. A viewer of camera placed at the original place of the object would see it.

With the digital implementation, one can keep the direction of the reference wave and instead compute the conjugate of the object beam in the computer. This is implemented by computing first the Fourier transform of the recorded intensity pattern. There are three terms as illustrated in Figure 1.10. One of the terms is the

Fourier transform of the conjugate of the object. By isolating this term with a mask in the Fourier domain, one can obtain the conjugate of the object by an inverse Fourier transform.

The conjugate of the object is then obtained and the phase part is then multiplied in the computer with the conjugate of the reference wave and displayed on a phase spatial light modulator (SLM). Upon illumination with the reference wave, one obtains the conjugate object wave:

$$E_R(x,y) \cdot (E_R^*(x,y) \cdot E_0^*(x,y)) = E_0^*(x,y)$$
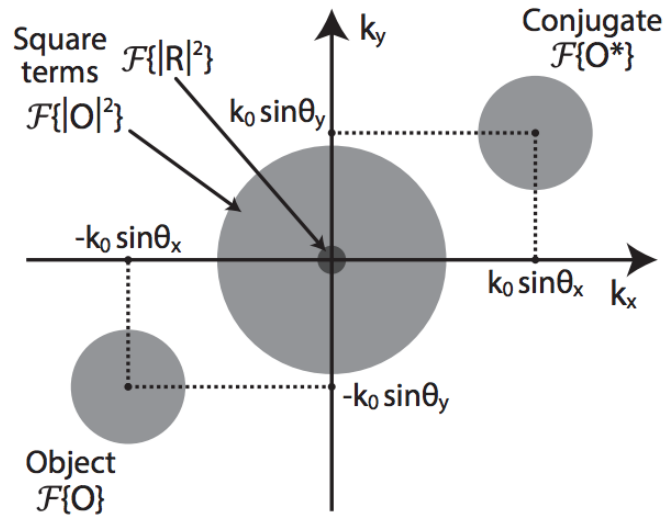
Figure 1.10: Separation of the various terms in the Fourier transform of an off-axis hologram, the off-axis angle is θ. Image courtesy of [64].

Another method for the characterization and control of light propagation for a scattering medium is the Scattering Matrix method. In this framework, a linear operator S relates an incoming wave to an outgoing wave the process. In the case that these states are expressed as vectors in a properly selected basis, the relationship is a matrix operation $\Psi_{in} = S\Psi_{out}$, where S is named scattering matrix. The interactions in the scattering matrix are allowed in any direction. More specifically, if reflections from the object back to the source can be neglected, only a part of the full scattering matrix is considered, then we are referring to the Transmission Matrix. When an input pattern X is coupled inside a multimode optical fiber, it undergoes a linear transformation characterized by the linear matrix operator T. The output

pattern Y at the output of the fiber is related to the input pattern as Y=TX. X and Y are vectors of complex coefficients, in a given selected basis, which are the amplitude and phase of the optical field at the input and output of the MMF respectively [64].

In the transmission matrix method, a linear relationship between input and output waves is assumed. This assumption is valid as long as the polarization is linearly related to the optical driving field. This means that for low intensity, the term in the polarization is neglected. On the other hand, in the transmission matrix method many parameters are required. Despite this, the transmission matrix in practice remains convenient because in addition to modal scrambling, it captures imperfections of experimental setups such as aberrations, misalignments etc. It is also useful for several types of fibers, such as multi-core fiber, or graded index fibers.

The transmission matrix, which is used and explained in the experiments of Chapter 3 is measured in the following way. We apply a set of inputs to the system through the spatial light modulator (SLM). This means that we know this set of inputs which are sent from the SLM to the input of the fiber, and we record a corresponding set of outputs. It needs to be underlined that this set of outputs is basically interference patterns and not exclusively the output pattern of the fiber (speckle pattern). In this way, the transmission matrix is later able to predict which phase pattern must

The basis used for this experiment is the "Fourier basis", which means that the input patterns is a set of plane waves with varying angles. This type of patterns can be displayed very accurately by a phase-only modulator. Furthermore, each phase mask like this, covers the whole field of view on the SLM, consequently the maximum amount of light is guided to the fiber during the measurement.

To calculate the required input wavefront, the first step is to invert the transmission matrix. The algebraic inverse T^{-1} cannot be used due to measurement noise. In phase conjugation, the Hermitian transpose of the matrix can be used as its inverse $T_{inv} = T^{+}$. By using T^{+} is equivalent to performing optical phase conjugation which required less computation. In the Tikhonov inversion, the inverse of the transmission matrix is calculated as $T_{inv} = (T^{+}T + \lambda I)^{-1} T^{+}$ [64].

1.4.2   State of the art

New imaging techniques have been developed thanks to digital phase conjugation and the transmission matrix method by using optical fibers. At first, Papadopoulos et al. showed the generation and the scanning of a focused spot at the output of a multimode fiber by using a CW source at 1064 nm [65]. This work was followed by developing this system for endoscopic imaging through a multimode fiber and by using a CW laser source at 532 nm [66]. A pulsed laser source was used for digital phase conjugation through a multimode fiber in the work of Morales et al.[67] and two-photon imaging and 3D printing was accomplished as well [29], [68].

The transmission matrix method was used for imaging and 3D printing purposes. Loterie et al. acquired confocal images through a multimode fiber by controlling light propagation through them [69]. Single-photon additive manufacturing through a multimode fiber was demonstrated after that in the work of Delrot et al. by combining oxygen radical scavenging [70]. Both the digital phase conjugation and the transmission matrix method are based on digital holography. One important advantage of the transmission matrix compared to the digital phase conjugation is that there is no need of pixel-to-pixel alignment between the spatial light modulator and the camera.

1.5   Volumetric 3D printing

1.5.1   Basic Concepts

Volumetric 3D printing is a newcomer in the field of 3D printing. The working principle is inspired by computed tomography (CT). In Computed Tomography, a set of X-ray radiographs of a human or object are acquired from different angles. The obtained projections are later processed with a tomographic algorithm (inverse Radon transform) to reconstruct a cross-sectional image of the object. These reconstructed images represent the distribution of absorbed X-ray dose inside the object. In volumetric-tomographic 3D printing, this method is used in reverse. In particular, the digital model of the desired object is processed in a computer to generate the set of angle projections. All these projections are displayed one-by-one by using visible light and a projector. Typically, a reflective projector using a Digital

Micromirror Device is used. The projected patterns are imaged in the center of a rotating vial which contains the liquid photopolymer. The cumulative absorbed dose distribution in 3D results in the solidification of the liquid when the dose is above the required threshold. In this way, the three-dimensional object is formed inside a transparent resin [71].

Radon Transform and Sinogram

The Radon transform was introduced by Johann Radon in 1917 and it is widely used in Computed Tomography. It can be simply explained in the following way, referring to Figure 1.11: consider a two-dimensional object defined by the function f(x,y) in a Cartesian coordinate system and a line on the same system which is called the detector line which records the intensity of the projection through the object $p_\vartheta(d)$.
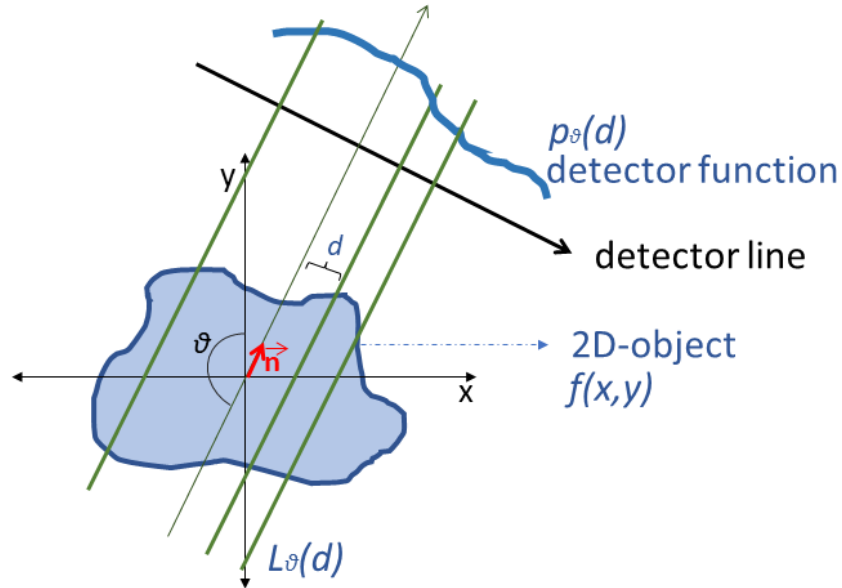
Figure 1.11: Projection imaging geometry in Computed Tomography

At first, we select a fixed projection direction ϑ and calculate the line integral of the object for all the positions d of the projection line. Repeating the projection for many angles by rotating the pair source and detector around the object, we obtain the discretized Radon transform [72], [73].

$$e.\ 9:\ Rf(\theta, d) = \int_{L(\theta,d)} f(x,y)ds$$

The Radon transform represented in the coordinate system of ϑ and d is called a sinogram. In Figure 1.11, it is illustrated what it was described above for a fixed projection direction. To recover the object, each projection needs to be first filtered in Fourier space by a linear ramp. Figure 1.12 below illustrates an object (Figure 1.12.a) and the projections represented as a sinogram (Figure 1.12.b). A smeared projection is shown for one angle, which is the 1D projection in one axis and "stretched" in the orthogonal direction (Figure 1.12.c). This smeared projection is filtered in Fourier space and after filtering, the inverse Fourier transform yields the filtered projection (Figure 1.12.d). For volumetric printing, only the positive values of the filtered projection are required since light intensity is positive.
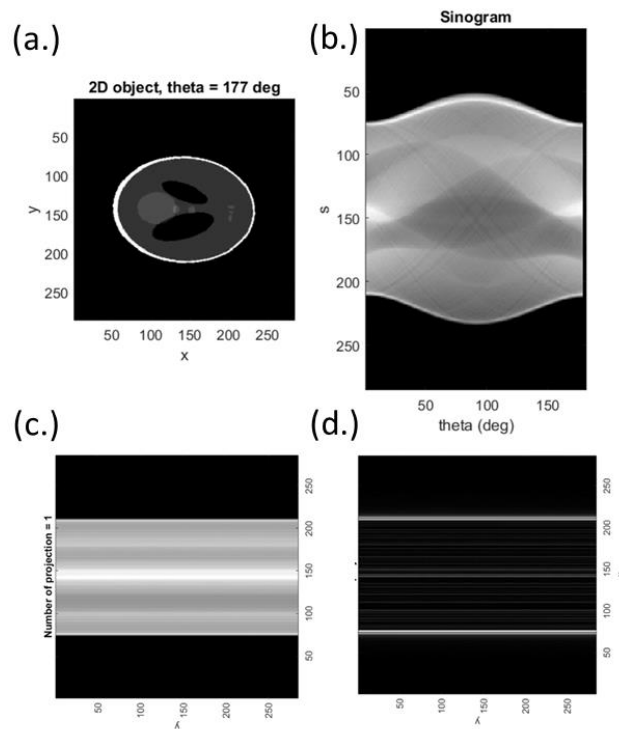
Figure 1.12: Tomographic 3D printing :(a.) 2D object, (b.) sinogram, (c.) a smeared projection (1D projection), (d.) filtered projection.

Single-photon polymerization

The Volumetric Tomographic 3D printing method solidifies the liquid polymer based on single photon absorption. Single photon absorption is linear, which means that the absorption coefficient is independent of the optical intensity [74][75]. The

attenuation of light intensity *I* inside a material, for the case of single-photon absorption, is described by the following equation:

$$e.\ 10: \quad \frac{\partial I}{\partial z} = -\alpha I$$

If the cumulated single-photon absorbed dose is higher than the polymerization threshold, then polymerization occurs and the liquid polymer is solidified.

1.5.2   State of the art

Volumetric additive manufacturing was reported by M. Shusteff et al. in 2016. In this work, three beams are incident simultaneously in a resin [76][77]. This work evolved to utilizing the Radon transform by illuminating a resin-filled rotating vial with a dynamically evolving light pattern from a DMD [78]. Loterie et al. demonstrated high resolution tomographic volumetric additive manufacturing by using a spatially coherent light source and integrating a feedback system to control accurately the photopolymerization kinetics over the entire build volume to improve the fidelity of the part [79]. The method works well with transparent and homogeneous resin. Scattering transparent resins distort the direction of the projections and thus degrade severely the fidelity of the printed objects. Madrid-Wolff et al. studied how light is distorted by a scattering curable resin. Applying a digital correction to the light patterns effectively mitigates the effect of scattering [80]. In my work in chapter 4, the resins were transparent and non scattering, as it will be shown. Thus, there was no need to perform pattern correction.

Chapter 2   Additive micro-manufacturing of crack-free PDCs by two-photon polymerization

This chapter reports my work on the fabrication of low-shrinkage and crack-free ceramic microstructures by two-photon polymerization. More specifically, I demonstrate the fabrication of high-resolution (~350 nm) polymer-derived ceramic microstructures through TPP of an inexpensive, highly viscous preceramic polymer, which belongs to a single class of PCPs, namely polysiloxanes without addition of fillers or other additives. Some of the material presented in this chapter can be found in the following publication [81]:

Georgia Konstantinou, Eirini Kakkava, Lorenz Hagelüken, Pradeep Vallachira Warriam Sasikumar, Jieping Wang, Malgorzata Grazyna Makowska, Gurdial Blugan et al. "Additive micro-manufacturing of crack-free PDCs by two-photon polymerization of a single, low-shrinkage preceramic resin." Additive Manufacturing (2020) by Elsevier.

2.1   Background

The fabrication of ceramics with complex shapes is a challenging task but can be achieved by several 3D printing methods which are categorized based on the feedstock and the material processing technique (thermal, optical or chemical etc.). As an example, in Stereolithography (SLA), Digital Light Processing (DLP) and Inkjet Printing (IJP), a slurry-based feedstock is used (resin or ink). Selective Laser Melting and Sintering (SLM/S) are powder-based techniques whereas in Fused Deposition

Modelling, solid-based raw materials are used [10], [18], [43]– [45]. The resolution range in AM technologies is wide, depending on the material, the size and the application of the 3D printed part. For the technologies mentioned above and for materials which are not ceramics, the resolution is lower for FDM and SLS/M (100–300 μm) and higher for SLA, IJP and DLP (25–100 μm). The best resolution (100–200 nm) can be achieved using two-photon polymerization (TPP/2PP) technique [56], [82], [85], [86].

The applications of ceramics are found in a variety of fields. For instance, the fabrication of devices for chemical or biological analysis (separation devices, high performance liquid chromatography or rRNA sequence analysis), for aerospace engineering (pumps and propulsion components, fans, gas turbines), electronics fabrication (transducers, RF ceramic capacitors), for automotive engineering (Piezo-ceramic components with ceramic substrates for sensors like anti-lock braking system (ABS) or traction control system (TCS/ASR systems), implant components or tools fabrication for biomedical applications (e.g. orthopedic or dental devices) [87]–[89].

To produce micro-parts and micro-devices, light-based AM techniques are selected because they can ensure high resolution compared to more traditional AM technologies such as FDM. 3D AM-based technologies have successfully demonstrated the microfabrication of polymer-derived ceramics (PDCs) based microcomponents [90]–[92] . In micro-stereolithography of preceramic polymers (PCPs), the raw materials are based on liquid organosilicon polymers.

Polymer derived ceramics were tested for the fabrication of advanced ceramics in the 1960s [93] and new formulations are being developed until today [83]. They are synthesized thanks to polymer-to-ceramic conversion of single source preceramic polymer precursors (PCPs). The properties of a PDC microstructure can be tailored by modifying the chemical composition of the polymer precursors [94], [95].

The silicon-containing PCPs comprise several classes such as polyborosilanes, polysilazanes, polysiloxanes, polycarbosilanes etc. The difference between these classes is related to the polymeric backbone structure as the latter influences the reactivity, the cross-linking behavior, the type of ceramic it is converted into and correspondingly the properties of the final PDC [93]. In other words, the molecular structure and the type of PCP influence the composition, the number of phases and

the phase distribution of the final ceramics, which implies variability in their overall resulting properties [96]–[101]. For example, polyorganosilanes are composed of a Si-Si backbone and organic substituents attached to the silicon atoms. The various side group (alkyl, phenyl or metal alkoxide) can be attached to the polymer backbone of the starting preceramic precursors and to improve the properties of the final PDC (e.g. magnetic, electrical, porosity, mechanical, energy storage capacity etc.).

To achieve high resolution ceramic parts, two-photon printing of various classes of preceramic polymers were achieved 3D structures with resolution <200 nm [90], [91], [96], [102]. The non-linear effects in two-photon polymerization lead to polymerization volume (voxel) better than the optical resolution.

In the work of Brigo et al. [90] a polysiloxane was used for the fabrication of microstructures and after pyrolysis at 1000 °C, a linear shrinkage >50% was observed with no significant shape distortion. In the work of Park et al. [102] and Wang et al [103], a polycarbosilane in combination with an organometallic-type additive and/or silica nanoparticles as filler was used. Despite the versatile properties of the latter one and the low shrinkage observed after pyrolysis at 600 °C, severe cracks were observed for temperatures higher than that. Pham et al. [104] used a type of polysilazane in purified argon atmosphere for similar purposes. At high pyrolysis temperatures they observed severe volume shrinkage and significant weight loss and densification.

Polysiloxanes can often be used under ambient conditions, compared to polycarbosilanes and polysilazanes, as they are chemically stable at room temperature. SPR-684 is a carbon-rich polysiloxane with methyl, vinyl and phenyl functionality. It is transparent in the visible and near infrared spectrum and yields a silicon oxycarbide ceramic after pyrolysis at 1000 °C [94]. Oxycarbide describes a chemical structure in which silicon has a bond to carbon and oxygen, forming tetrahedral structural units of $SiO_{4-x}C_x$ (x = 1-4). These units build up an amorphous and heterogeneous Si-O-C network phase, in which free carbon might be dispersed and likewise SiO_2-enriched regions can form. After the pyrolytic transformation, there is release of carbon-containing volatile units which results a decrease of the intensity of the C in the spectrum obtained by X-ray photoelectron spectroscopy (XPS) [39], [92], [95], [101], [105].

The pyrolysis of preceramic structures of my work was performed in a tubular furnace under argon atmosphere. As mentioned before, a linear shrinkage of 60%-70% of the TPP derived green body structure is usually reported after the pyrolysis step [90], [91] with peak temperatures in the range of 800 – 1000 °C and the shrinkage percentage can be improved by additives in the initial mixture [102]–[104]. A linear shrinkage of only 30% is observed for the PCP (no additives or mixtures with other polymers) used in this work, which shows low porosity, no cracks and no significant shape distortion. A larger shrinkage can hinder detailed printing and deform the green body, which makes the resin formulation used in this work an attractive option.

In the following paragraphs, we further elaborate on the fabrication of the preceramic resin, on the methods employed for TPP 3D printing and on the pre-processing and post-processing protocol, which consists of the developing and the pyrolysis step. The green bodies and the final pyrolysed ceramic structures are imaged by Bright Field (BF) and Scanning Electron Microscopy (SEM). The ceramics are chemically characterized by X-ray photoelectron spectroscopy analysis (XPS). The elemental composition and the final ceramic parts are additionally imaged by X-ray tomographic microscopy to provide structural information.

2.2   Experimental setup and methods

A two-photon printer (Nanoscribe Professional GT 3D) was used to conduct the experiments on the preceramic resin. The laser source is a frequency doubled ultrafast erbium doped fiber laser system provided by Toptica Photonics AG, with central wavelength (λ) at 780 nm (second harmonic generation), pulse duration 100 fs, repetition rate 80 MHz and maximum average output power 140 mW.

This 3D printer operates in two printing modes: a) Continuous and b) Pulsed Mode. In the Continuous printing mode (which is usually selected with the STL import of a 3D model but can be also selected in a coded file), the laser is turned on at the first voxel and turned off when reaching the last voxel. In the Pulsed Mode, the laser is continuously turned on and off for every voxel. In Continuous Mode, the light power and the stage speed can be modified to provide a given light dose per voxel, whereas in the Pulsed Mode, the power and the exposure time can be set for each voxel. A

file with voxel coordinates, power values and exposure times per voxel or per group of voxels is used by the printer.

In Continuous mode, along xy, the line-by-line distance, which is called "hatching" can be preset. The hatching distance can be set for the x and y direction in the Continuous Mode operation. In the orthogonal direction to the xy plane, the layer-by-layer distance is called "slicing distance". In Pulsed Mode, the spacing between the 3D voxels are specified by coordinate values. In experiments, I selected this mode in the voxel dose tests [106].

In this experiment, the oil-immersion configuration with a 63x objective lens (with numerical aperture NA 1.4) allowed avoiding aberrations. The maximum power delivered through this objective lens is 50 mW. In the Continuous mode, xy scanning was performed by using the galvo mirrors installed in the 3D printer within a speed ranging from 700 μm/s to 900 μm/s. The z scanning was performed with the piezo stage of the printer and the minimum tested z motion was 100nm.

The photosensitive preceramic resin is deposited on a quartz slide (thickness: 170 μm, refractive index: 1.45). Quartz slides were used because quartz melts at ~1700 °C and has a high glass transition point (~ 1200°C). They are thus resistant to a temperature of 1000 °C, which is necessary for the pyrolysis step. The printing process is monitored through a camera installed in the 3D printer and by using the embedded bright field microscope.

After the end of the 3D-printing process, the unexposed preceramic polymer (PCP), which remains in liquid form, is removed via a chemical development with toluene. This is obtained by dipping the quartz slide with the printed structures in toluene for 5 minutes. The slide is removed from the toluene bath and left at room temperature for evaporation.

The quartz slide with the green body microstructures is then placed in an alumina crucible and inserted into a tube furnace (STF 15/450, Carbolite Gero, Germany) for pyrolysis. The tube is purged with argon for 30 minutes and a low argon flow is maintained during pyrolysis. In Figure 2.1 all the steps from printing to pyrolysis are illustrated.

A heating/cooling rate of 5 K/min, a 2 h thermal crosslinking step at 200 °C and 1 h dwell time at 1000 °C is applied. The reason for selecting this pyrolysis temperature

is to achieve optimal polymer to ceramic conversion, which is verified by the detailed characterization of the prepared samples in the following paragraphs.
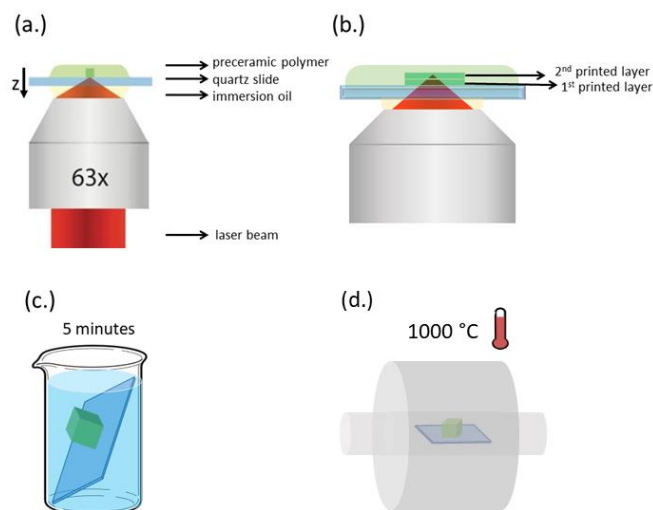
Figure 2.1: (a.) The oil-immersion printing configuration showing the printing of a cube starting from the top interface of the quartz slide. The fabrication is completed by bottom-up printing, which means that when the first layer is printed, the piezo stage moves down as it is shown with the arrow, (b.) a magnified schematic showing which layer was printed first, (c.) toluene bath for 5 minutes to remove the unexposed preceramic resin, (d.) pyrolysis furnace heating for ~9 hours (peak temperature 1000 °C).

2.3   Pre-processing and polymerization mechanism

Commercially available preceramic resins are widely used as single source precursors for synthesis of carbon rich SiOC ceramics [90], [91], [93]. The selected preceramic resin of this work is an inexpensive, commercially available polysiloxane (SPR-684, Polyramic series, Starfire Systems) with a refractive index higher than 1.5, which is close to the index of the quartz slides (n~1.45). This viscous single preceramic polymer (~1000 cps) is tested separately in combination with two different photoinitiators and finally combined with 3.4% w/w concentration of a two-photon active photoinitiator (PI): 4,4'-bis(diethylamino) benzophenone (BDEBP) 99+% photoinitiator (ACROS ORGANICS) to prepare the final photosensitive mixture [56], [94], [95], [107]. No additional fillers were used [102]–[104].

The preparation of the final formulation is divided in 4 steps: a) the PI is dissolved in acetone by using a magnetic stirrer at room temperature for ~6 hours, b) the acetone-photoinitiator solution is mixed with the resin again by magnetic stirring

(1:1 ratio) for ~9 hours, c) while the magnetic stirring process continues, the resin solution is heated for 40 minutes on a hotplate set at ~50 °C and in this way the acetone is removed and d) the final resin is obtained after de-bubbling by vacuum drying for 30 minutes. This process is illustrated in Figure 2.2.
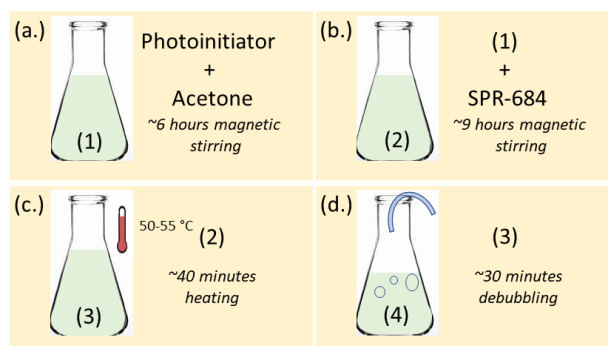
Figure 2.2: The four steps for preparing the final formulation of the preceramic resin. The first step is shown in (a.) and the last step is shown in (d). Each number in parentheses inside the bottle represents the formulation that occurs after following the steps described in the right side of the bottle.

As previously mentioned, polysiloxanes are easy to handle under ambient conditions, which makes their use versatile and cost-efficient by removing the need of an inert (moisture and oxygen-free) atmosphere (N$_2$/ Ar glove box/ Schlenk line) [104], while it promotes repeatability in the production of customized ceramic parts. This finalized protocol was verified after conducting a set of preprocessing tests about the selection and the concentration of the photoiniator and the mixing method. In the following table (Table 1), the results of these tests are summarized:

Table 1: Preprocessing tests for the protocol of the resin formulation.

# Test	(a) Solvent Acetone (g)	(b) Photoin.1 DETC (% w/w)	(b) Photoin.2 BDEBP (% w/w)	(c) Material Polysiloxane resin (g)	Mixing order	Result	Comments
1	x	1	x	0.5	(b)+(c)	x	High viscosity of (c)
2	0.25	8	x	0.5	[(a)+(c)] + (b)	x	Crystallized residues
3	0.5	8	x	0.5	[(a)+(b)] + (c)	x	Crystallized residues
4	0.5	4	x	0.5	[(a)+(b)] + (c)	x	Crystallized residues
5	0.3	0.5	x	0.5	[(a)+(b)] + (c)	✓	Homogeneity issues/bubbles
6	0.3	x	1.3	0.5	[(a)+(b)] + (c)	✓	Homogeneous
7	0.3	x	2	0.5	[(a)+(b)] + (c)	✓	Homogeneous
8	0.5	x	3.5	0.5	[(a)+(b)] + (c)	✓	Homogeneous

DETC: 7-diethylamino-3-thenoylcoumarin

BDEBP: Bis(diethylamino)benzophenone

x: failed

✓ : succeeded

In the first 5 tests, the photoinitiator DETC was used because it is commonly used for two-photon polymerization experiments. The high viscosity of the preceramic resin in combination with this photoinitiator resulted in crystallized residues in the resin. In the printer, the inhomogeneous mixture in generated bubbles and no polymerization. We attribute this to an inhomogeneous density of PI (aggregates) leading to areas strongly absorbing that leads to heating and bubble generation.

Printing tests were conducted with samples 5-8. The best -without bubbles- prints were obtained by using the last protocol and this one was selected to be used for all the following experiments. In this protocol, the photoinitiator BDEBP was at first dissolved successfully inside the solvent and the final resin, which was obtained with the previous mixing steps. The resulting resin was uniform and selected for all following experiments.

The formation of the green body starts with two-photon absorption of the incident light by the PI yielding a radical. Then, the polymerization is propagated via a vinyl polymerization mechanism [95]. Figure 2.3.a shows the first step (initiation), where the double bond of the central oxygen breaks after two-photon absorption. Figure 2.3.b illustrates the molecular structure of this polysiloxane and the propagation step via the cross-linking mechanism of vinyl polymerization [101].
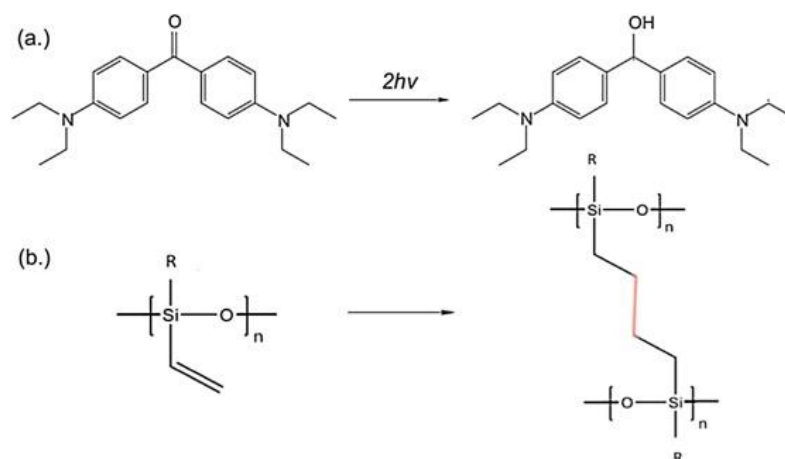
Figure 2.3: (a.) free radical initiation with two-photon absorption by the photoinitiator BDEBP, (b.) propagation step via vinyl polymerization.

In the second step, the propagation of the polymerization is accomplished via vinyl polymerization. The first radical generated at the initiation step (photoinitiator)

activates the radical polymerization of the participant monomer followed by a propagation chain growth. The functional groups do not participate in the crosslinking. Figure 2.4 and Figure 2.5 shows an image of the polymerized structures taken with a bright field camera in the printer. In these images, the protocol was not yet optimized as can be seen from the residues that are found in the resin as dark spots.
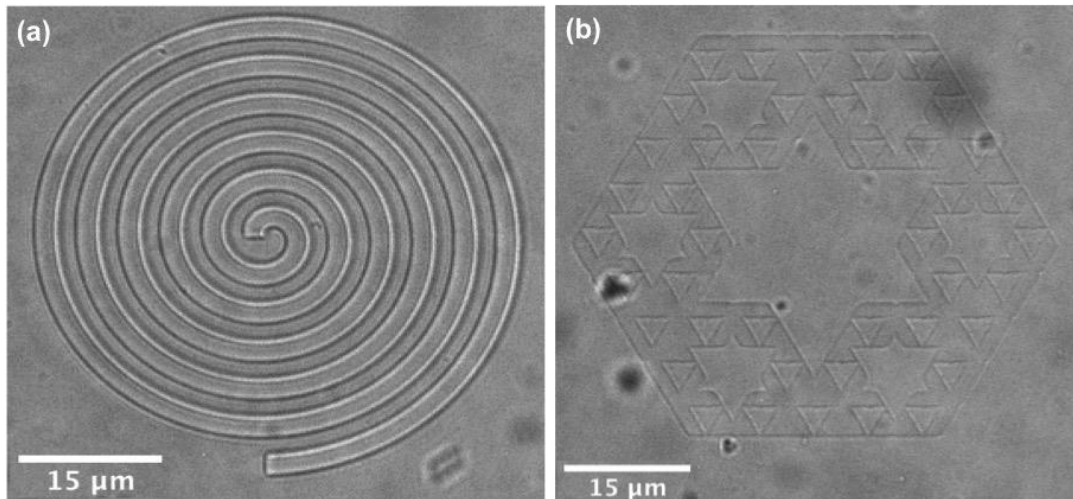
Figure 2.4: (a) Spiral shaped 2D+1structure (height ~10 microns), (b) Fractal shaped structure (single layer), scale bar: 15um. Both of these structures are in green state and are imaged during the polymerization process (before development) with the Zeiss microscope integrated in the Nanoscribe System in bright field mode.

3D Printing test
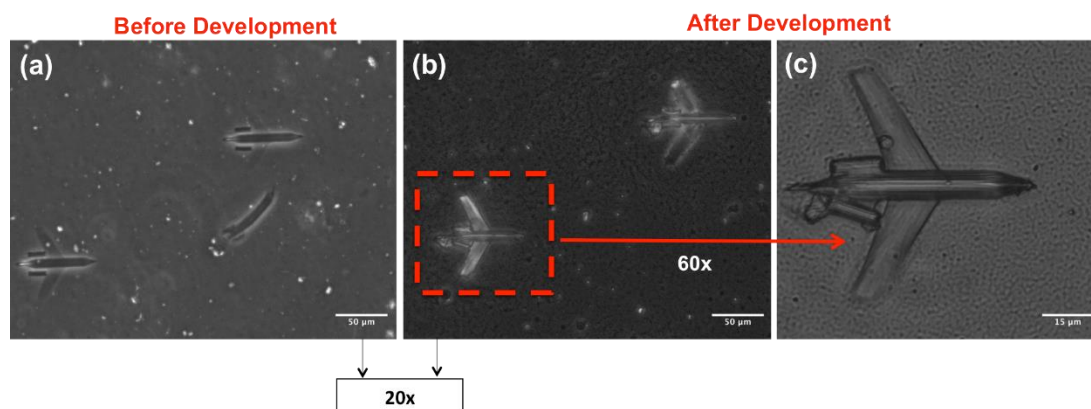
Figure 2.5: (a) Three aircrafts are printed and shown with 20x magnification before development (b) after development, 2 of the aircrafts survived because they were well attached to the glass slide and (c) the left aircraft is shown with 60x magnification. In (a) and (b), scale bar: 50um, in (c), scale bar: 15um. (images obtained with a phase contrast microscope).

2.4   Results and Discussions

2.4.1   Linewidth characterization and polymerization threshold

The objective lens with NA = 1.4 (oil immersion) results in an optical lateral resolution of 280 nm based on the Abbe diffraction limit (e.3). To characterize the dependence of the printed linewidth on the light exposure dose and investigate the polymerization threshold for a single layer exposure, we scanned in galvo-scanning mode a set of 15 lines with 6 different power levels from 5 to 30 mW.

Each line, of 10 μm length, is exposed in a single pass and attaches to the slide (Continuous Mode). The scanning speed ranges from 0.05 μm/s to 10 μm/s. Figure 2.6.a shows the images of the printed lines obtained with a Differential Interference Microscope (DIC) corresponding to the 6 different power levels used. In each image of Figure 2.6.a, the scanning speed is increasing from left to right. We measured the linewidth (FWHM) of each line for all power levels before the chemical development of the sample since the lines are collapsing after dipping into in toluene. In Figure 2.6.b, the linewidth is plotted as a function of the scanning speed for all the power levels in a 2D plot.
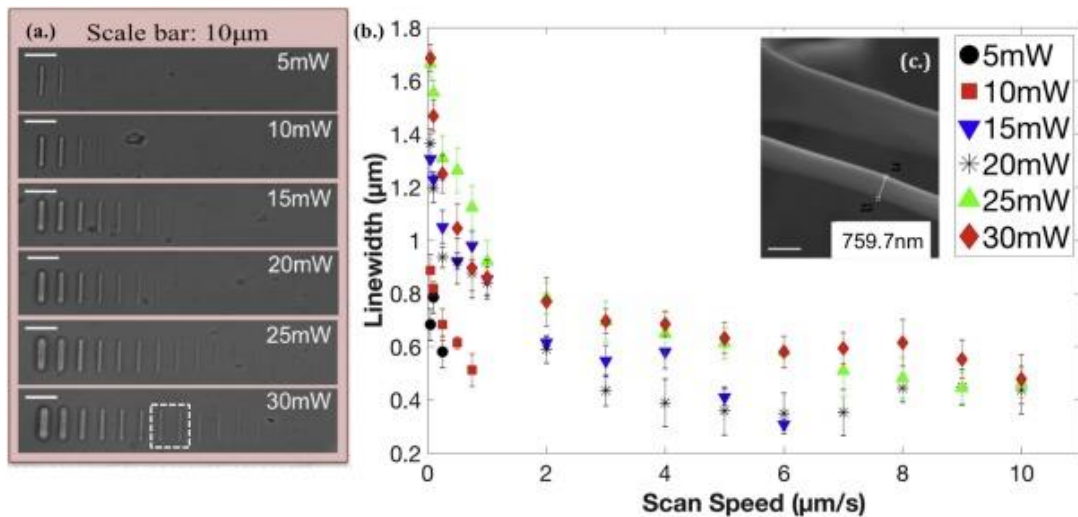
Figure 2.6: (a.) 15 printed lines are shown for increasing power level (images by DIC microscopy). The scale bar is 10 μm. The 7th and 8th line (for power level 30 mW) are highlighted with a white dashed-line square in (c). (b.) The measured line widths (FWHM) are plotted with the error bars and with different shape/color for each power level. (c.) SEM image of the two lines highlighted in (a.), the sample is tilted at 45°. The scale bar in (c) is 1 μm.

In Figure 2.6.b, we can observe that the minimum measured linewidth is ~349 nm (blue triangle with average power 15 mW and scan speed 6 µm/s). The exponential linewidth decrease as a function of scan speed is due to the exponential decay of the monomer concentration upon light exposure [29], [56], [108]. Then, we calculate the minimum exposure dose, which results in an efficient and distinct line printing based on the DIC image shown in Figure 2.6.a, [108]–[113]. The polymerization threshold corresponds to a dose of 8.5-9.9 J/cm^2 for writing a line. Additionally, for higher power and higher scanning speed, we can observe a saturation of the linewidth with negligible differences for the three highest power levels used. The energy per pulse is 0.125 nJ and the exposure dose D is given by [112], [113] :

$$e.\ 11:\quad D = f_{rep}\tau_L\sqrt{\frac{2}{\pi}\frac{P_t}{w_0 v}}$$

where f_{rep} is the repetition rate of the laser, τ_L the pulse duration, v represents the scanning speed, w_0 is the waist of the focal spot and P_t is the average power. In Figure 2.6.c, two lines printed with different scanning speeds (2 µm/s and 3 µm/s) at 30 mW power level, are imaged -after development- by Scanning Electron Microscopy. The linewidth characterization is not a direct indication of the dose required for the fabrication of 3D microstructures. This study only gives us the minimum feature size we can expect in a 3D structure. For this purpose, I performed a set of dose tests with cuboids.

2.4.2 Shape fidelity evaluation with cuboid microstructures

Cuboid microstructures were printed with scanning speeds between 400 and 8000 µm/s (more than 40 times higher than the maximum speed used for single lines in paragraph 3.1) and an average power of 25 mW, which corresponds to a peak intensity of 3.95 TW/cm^2. The slicing and hatching distance (100 nm or 200 nm) along with the cumulative dose resulted in the building of a solid 3D structure. The dose tests are in the range 9.31 to 186.18 mJ/cm^2. The optical spot size is defined by the optical properties of the writing system concerning the lateral optical resolution (e.3) and axial optical resolution (λ/NA^2). The final cured voxel size though –above the threshold energy- depends on the exposure dose. However, in the case of 3D printed structures, the overlap between consecutive lines and layers results in a cumulative

energy deposition around each voxel and therefore the dose needed for the TPP of the whole volume of the structure is significantly lower than those reported for a single line in the previous section.

The fidelity of the structure and the characteristics of the cured 3D volume depend on several parameters such as the linewidth, the layer thickness hatching and slicing distance. All these parameters affect the gradual accumulation of the dose and determine the successful adhesion between the exposed areas [114]. The scheme in Figure 2.7 illustrates the writing of a 3D structure and the dose tests that lead to success or failure. A set of cubes was printed employing different combinations of the above parameters in order to determine the optimal printing protocol to obtain a high-quality 3D structure (Figure 2.7.c) [115], [116]. The parameters that were varied are: a) the hatching distance, b) the slicing distance and c) the exposure dose from D0 to D5 (D0 = 186.18 mJ/cm^2, D1 = 106.39 mJ/cm^2, D2 = 62.06 mJ/cm^2, D3 = 37.24 mJ/cm^2, D4 = 18.618 mJ/cm^2 and D5 = 9.31 mJ/cm^2). This test took place in order to evaluate the optimal conditions that ensure high fidelity of the final solid 3D structure. The criteria for selecting the optimized conditions were based on roughness, shrinkage and porosity after pyrolysis.
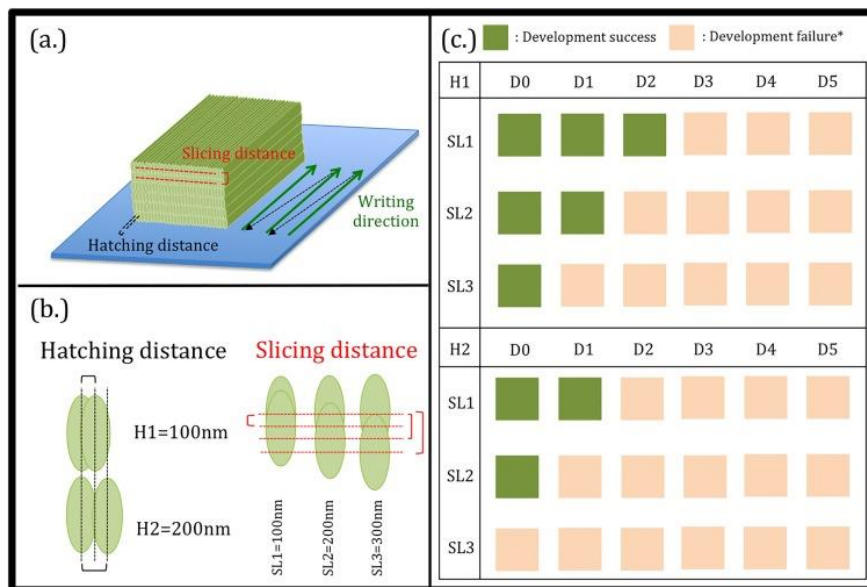
Figure 2.7: (a.) 3D illustration of the writing of a cuboid structure. The green arrows illustrate the writing direction of the scanned line whereas the dashed black arrows show how the writing will be continued for the next line (b.) The hatching is related to the lateral overlap of the voxels on a single layer and the slicing is the layer distance. Both are shown with 2D illustration for all tested values, (c.) Table with Success vs Failure after development for a set of 36 cubes printed with different parameters (dose from D0 = 186.18 mJ/cm^2 to D5 = 9.31 mJ/cm^2). *Development failure: partial or complete.

The set of cubes is first printed and monitored in real time in the Nanoscribe system through the integrated bright field microscope. All cubes were fabricated with support structures (cylindrical pillars) to minimize the stress forces at the interface between the substrate and the cube that would result in severe sample deformations during the next steps. Then, the printed green bodies are dipped in toluene bath as described above. This chemical development step in toluene bath, is a critical step concerning the success or failure of the fabrication of the desired structure.

After this step, we deposit a 20 nm gold layer (DP650, Alliance Concept, France) on the samples to image them with a Scanning Electron Microscope. The pink-colored rectangles (Figure 2.8. a, b, e, f) represent two examples of cubes that collapsed partially after the development, while the cuboids with green rectangles were successfully developed (c, d, g, h).
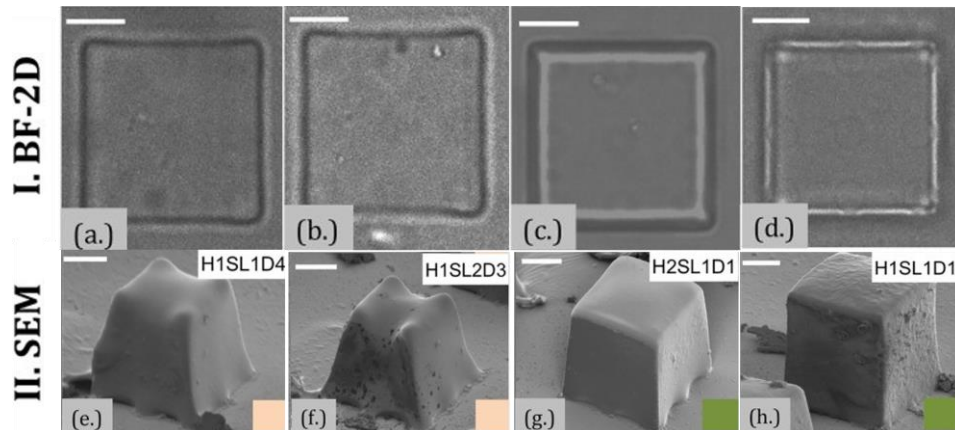
Figure 2.8: I. Bright field images of four different cubes obtained with the Nanoscribe BF microscope, right after the end of the printing process (before toluene bath). II. SEM images of the same cubes after the chemical development (green bodies). Scale bars: 10 µm.

Figure 2.9 presents the experimental linewidth data points (Figure 2.6) versus exposure dose. The expected minimum feature size for the cubes printed with good fidelity was obtained by extrapolation of the mentioned dose range (D0, D1 and D2 resulted in solid cubes- green colored squares).

Based on the extrapolation of the linewidth for the dose values used for the successful fabrication of the solid cuboids, we obtain values of features (linewidth) below the minimum linewidth (350 nm) measured in the case of the single-line

printed samples. This result is expected because we used a dose ~53 times lower than the threshold dose for the exposure of a line on a single layer. The proper selection of the hatching and slicing distance and the cumulative dose result in a subset of solid cubes with good fidelity.

Based on the observations above (Figure 2.8 and Figure 2.9), we selected the subset of cubes that ensure solid, non-collapsed structures after the development procedure as the best candidates for the inert gas pyrolysis. The subset of cuboids, which were imaged by SEM before pyrolysis and for which some samples were presented in Figure 2.8, were not the ones inserted into the pyrolysis furnace. New cuboids with identical printing parameters to the previous ones, were printed a second time. The green bodies were inserted into the furnace for pyrolysis without Au coating on their surface. The two sets of cuboids were at first inspected under a DIC microscope to verify that their shapes were the same as the previous prints to ensure that the final comparison is valid.
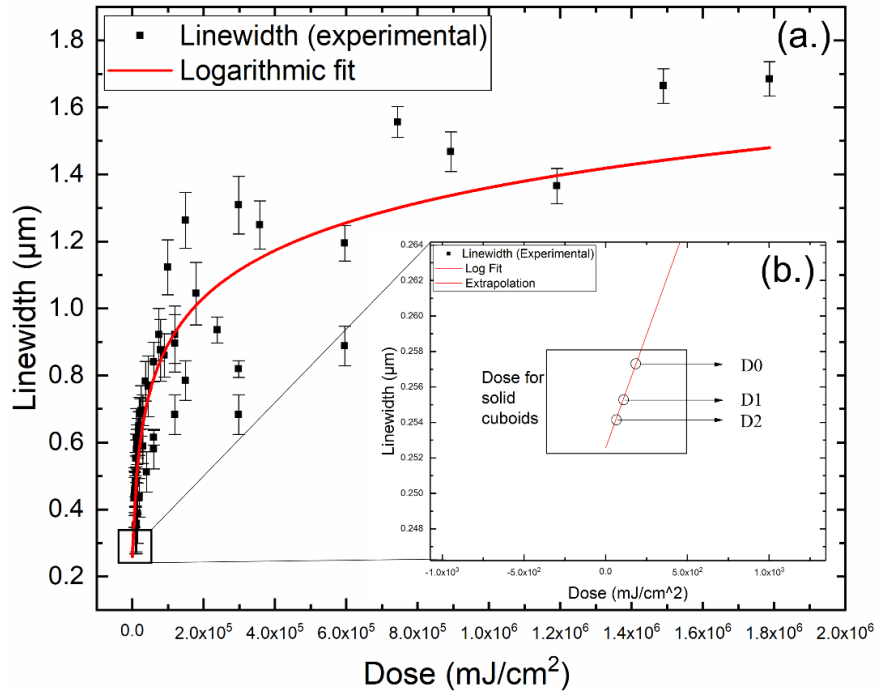
Figure 2.9: (a.) Dependence of the linewidth on the exposure dose, (b.) By extrapolation, the dose used for the fabrication of the cubes (small square) is zoomed in and presented in the same graph.

We performed the second prints to remove the effect of the Au coating on the pyrolysis step, which could affect the final ceramic part. In the 3D design of the

cuboids, nine pillars were also included and were symmetrically located under the bottom layer of the cuboid structures to promote adhesion and reduce the deformation due to the stress between the printed structure and the substrate. The selected cuboid green bodies were converted into SiOC by 1000 °C thermal treatment (as described in detail in paragraph 2.2). To quantify the mean linear shrinkage of these cubes, SEM images of the pyrolysed and Au-coated parts were also collected. Figure 2.10 shows the resulting pyrolysed ceramic cubes. We measured an isotropic shrinkage after pyrolysis with a mean value of linear shrinkage between 32% and 38% (three samples per case). This value is lower than what is commonly found in preceramic polymers (60-70%) and shown for TPP fabricated microstructures until now [90], [91].

Figure 2.10: SEM and AFM images (Col.1,2 and 4) of pyrolysed ceramic cubes printed with different parameters, the corresponding mean values of the linear shrinkage (Col.3) and the average roughness (Col.5) measured with Nanoscope analysis of the Atomic Force Microscope. Scale bar: 10 μm.

This is attributed to the molecular structure of this preceramic polymer, which results in extensive crosslinking and leads to high ceramic yield [94]. The slight differences of the shrinkage between the top and bottom parts of the cube are attributed to the stress forces of the supporting pillars to the bulk solid cuboid structure and it could be controlled more efficiently by increasing the height of the supporting pillars. This result underlines the high potential of the material for controlled fabrication of ceramic components even in the micron scale.

Further measurements to determine the average roughness of the fabricated cuboids shown in Figure 2.10, were conducted on an area of 4 µm x by 4 µm by using a Bruker's FastScan ScanAsyst Atomic Force Microscope system. The range of average roughness, presented in the Col.5 of Figure 2.10, is a bit higher than expected for two-photon fabrication structures (Nanoscribe: minimum surface roughness $R_a \leq 20$ nm) likely because of the pyrolysis process. The reason is that the different printing parameters (a, b, c and d) affect the shrinkage percentage and correspondingly the quality of adhesion between the scanned lines and layers. Moreover, the internal structure of the cuboids after pyrolysis was investigated by performing X-ray tomographic microscopy at the TOMCAT synchrotron beamline of the Swiss Light Source (SLS).

The tomographic scans were performed using a standard detector setup for full field tomography composed of a scintillator, an optical microscope with magnification 40x and a camera, which provides a field of view $0.3 \times 0.4 mm^2$ with 0.1625 µm pixel size. The energy of the used X-ray beam was 20 keV. 1501 projections were acquired over 180 deg with 200 ms exposure time per projection. Figure 2.11.a and b present the results of the tomographic studies after pyrolysis for the structures printed with the same conditions as the green bodies shown in Figure 2.11.e and Figure 2.11.f. Figure 2.11.c and Figure 2.11.d of the tomographic results show the tomography reconstruction corresponding to the successfully developed and pyrolysed cuboid structures printed with the same parameters as the green bodies shown in SEM results in Figure 2.11.g and Figure 2.11.h.

Tomographic studies revealed that in most cases, the volume of the printed cubes was homogeneous and crack-free and only in a few cases, the presence of closed pores was observed, which is illustrated by the yellow feature in Figure 2.11.d of the tomographic results. Both Figure 2.10, Figure 2.11 show the deformation and change of shape of the cubes for different printing parameters. The presented studies lead

to the conclusion that the printing conditions resulting in a solid, low-shrinkage, pore-free and smooth structure, are H1SL1 and H2SL1 within a dose range from D0 to D1. For these conditions, the porosity is expressed as the volume fraction of the pores and was found in the range from 0 to 1.3‰. We measured a porosity of the collapsed cuboid structures one magnitude larger compared to the cuboids, which survived pyrolysis without collapsing.
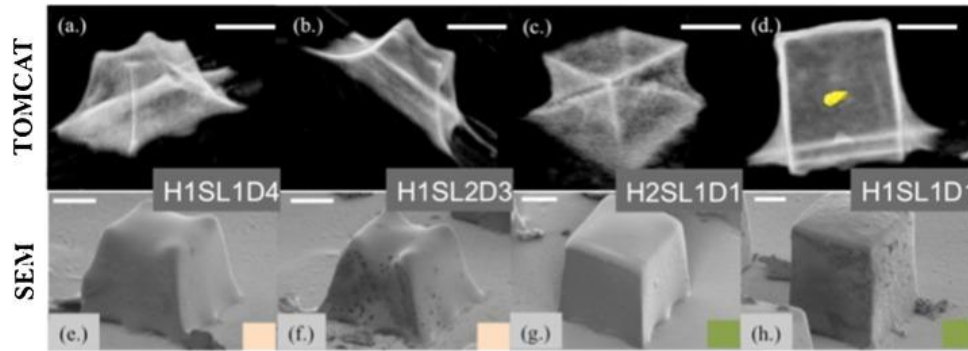
Figure 2.11: Volume rendering of tomographic data (TOMCAT) for the pyrolysed cubes shown in reference to the green bodies (SEM). Scale bar: 10 µm.

Figure 2.12 presents the bar-plot illustrating the effect of the printing parameters used for the samples in Figure 2.10 on the linear shrinkage and average roughness. The configurations with the minimum shrinkage are selected for fabricating complex structures. We show in this graph the isotropic shrinkage [117], [118] that was mentioned previously. The length (L), width (W) and height (H) show similar shrinkage percentages (red, blue and yellow bars).
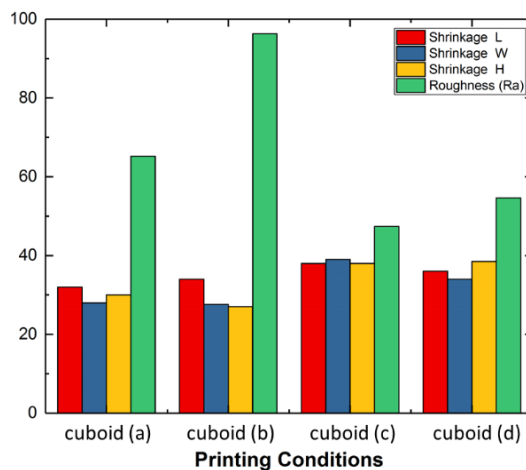
Figure 2.12: Linear shrinkage percentage and average roughness R_a evaluated for the four best printing conditions.

2.4.3   XPS analysis
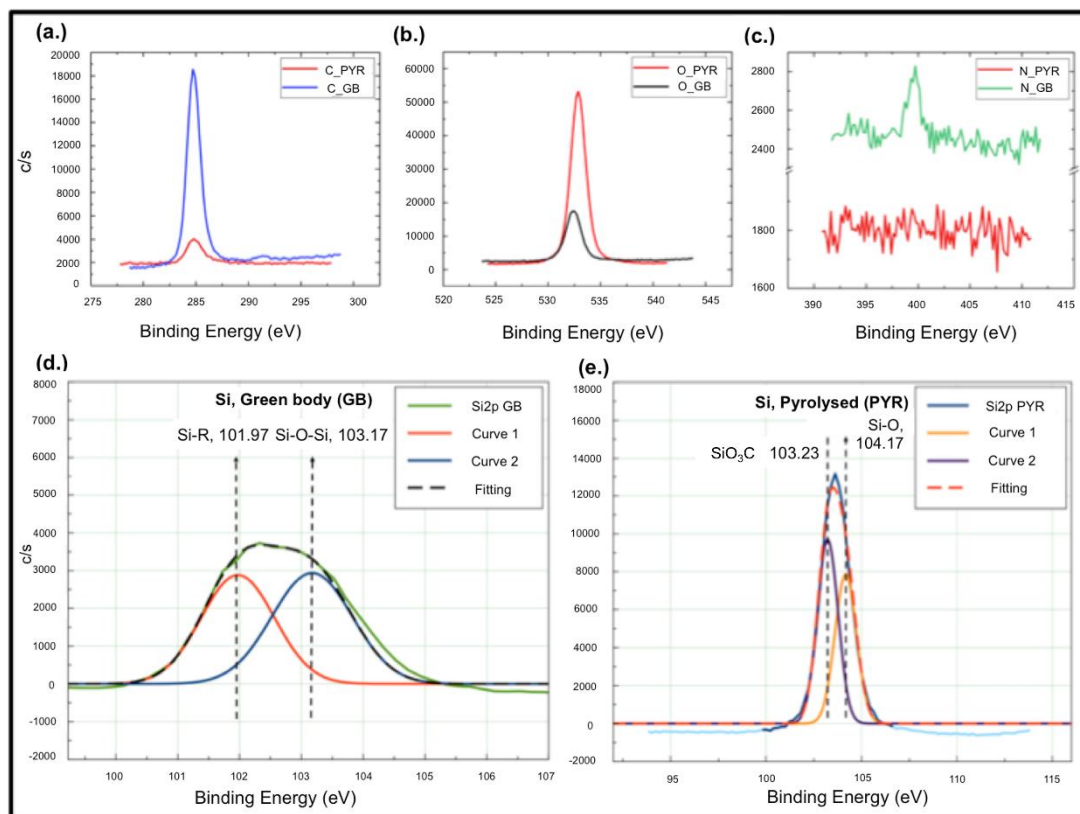
Figure 2.13: (a.) XPS data of the C1s bond in both states (green body (GB) and pyrolysed ceramic (PYR)), (b.) XPS data of the O1s, (c.) XPS data of the N1s (d.) XPS in the Si2p region of the green body, (e.) XPS in the Si2p region of the pyrolysed part.

The XPS spectra demonstrate the presence of Si, C and O atoms in both green body and final ceramic. The presence of C is confirmed by the existence of C1s peak in the XPS spectra. In Figure 2.13.a, a decrease in intensity of C1s is observed for the sample after pyrolysis. This is attributed to the release of carbon containing volatile units during the polymer to ceramic conversion [96]. The oxygen peak can be observed in both states. The difference of the binding energy of the oxygen in the SiO_2 and in the organic compounds is negligible, approximately 0.2 eV (Figure 2.13.b) [119].

From the O1s peak we can identify the percentile amount of oxygen, which is higher in the pyrolysed state. The reason for this large amount of oxygen in the pyrolysed state may be attributed to the presence of small amount of O_2 –which is always expected- inside the tubular furnace during the pyrolysis step. The effect of that

oxygen amount can be significantly higher for a microstructure compared to several larger ceramic structures (e.g. discs). In macroscale, the relative amount would be negligible because the oxygen for both cases (micro- and macro-scale) would diffuse mostly homogeneously [120], [121]. A peak representing nitrogen (Figure 2.13.c) can be seen at ~400 eV in the preceramic state, which is mainly attributed to the presence of residual photoinitiator.

In the Si2p region, the two fitted peaks of the green body are assigned to the presence of Si-O and Si-C bonds within the polymer backbone (Figure 2.13.d). The structure of the starting polymer precursor mainly comprises Si-O-Si units in the polymer backbone along with methyl, vinyl and phenyl functional groups. In the deconvoluted Si2p spectra of the green body, the peak at ~101.97 eV represents the Si-R bonds and the second peak at ~103 eV corresponds to the Si-O-Si bonds from the polymer backbone [122], [123].

The Si2p spectrum of the pyrolysed part (Figure 2.13.e) has mainly two bands at 103.23 eV and 104.17 eV representing mixed silicon oxycarbide units and Si-O bonds from the amorphous SiO_2 units in the final ceramics. The presence of SiO_2 signal leads to the shifting of the fitted curve to higher binding energy levels. In the following table the percentile elemental composition is presented for both states and confirms the aforementioned results [122]–[125]. A significant increase in the percentile amount of Si and O is observed in the pyrolysed sample and a corresponding decrease in the carbon content, advocating to the fact that the PDC is obtained after pyrolysis. In conclusion, the XPS results validate the high ceramic yield from the effectiveness of the pyrolysis process (Table 2).

Table 2: Elemental composition of the green state and the ceramic state of the SPR-684 (Starfire Systems).

State	C1s (%)	N1s (%)	O1s (%)	Si2p (%)
Green Body	57.05	0.94	26.26	15.75
Polymer Derived Ceramic	6.94	0.36	64.12	28.58

2.4.4 Complex 3D microstructures

Based on the obtained results, the laser scanning parameters were optimized, which allowed fabricating complex pyrolysed ceramic 3D microstructures with good fidelity. Figure 2.14 presents the CAD previews of a chess rook and a dragon with the final pyrolysed parts imaged by SEM.
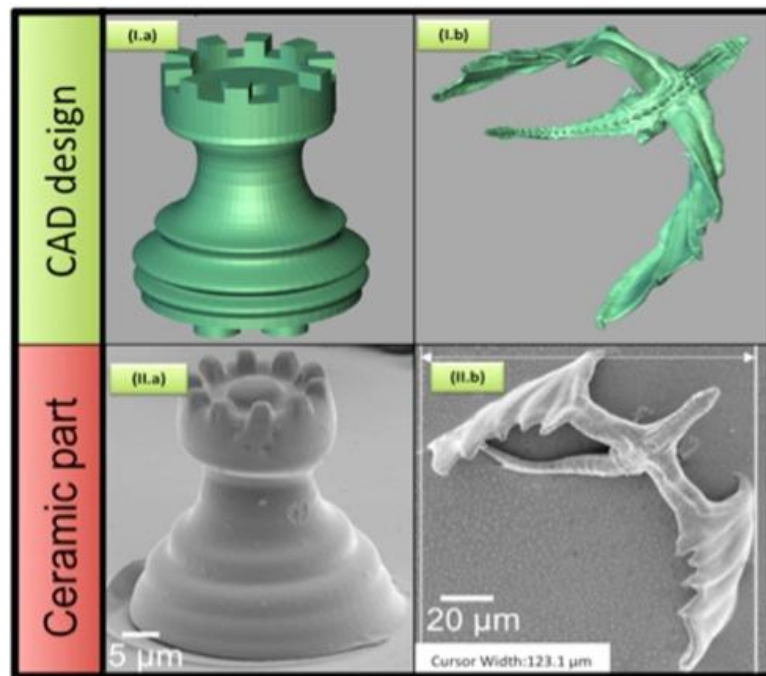
Figure 2.14: The CAD designs of two different structures (Describe © provided by Nanoscribe), II. the final pyrolysed parts.

The printing time of the chess rook (dimensions: 50 μm x 50 μm x 60 μm) was 1 h 50 min. and the printing time of the dragon with dimensions more than double of the chess rook was ~2 h. However, there was some difficulty in reproducing the finer features of the micro-dragon. Additionally, since the tail and wings are thin and without any support structures, they moved during the pyrolysis process. Finally, Figure 2.15 shows the fabricated micro-nozzle tip with 2D cross sections obtained by micro-tomography.

Figure 2.15 II. b reveals that some support structures were detached from the quartz substrate. The printing time of the nozzle tip (dimensions: 85 μm x 85 μm x 50 μm) was ~4 h 30 min. In this part, it was necessary to have a thick outer and inner nozzle (~5 μm each) tube to avoid collapsing of the structure.
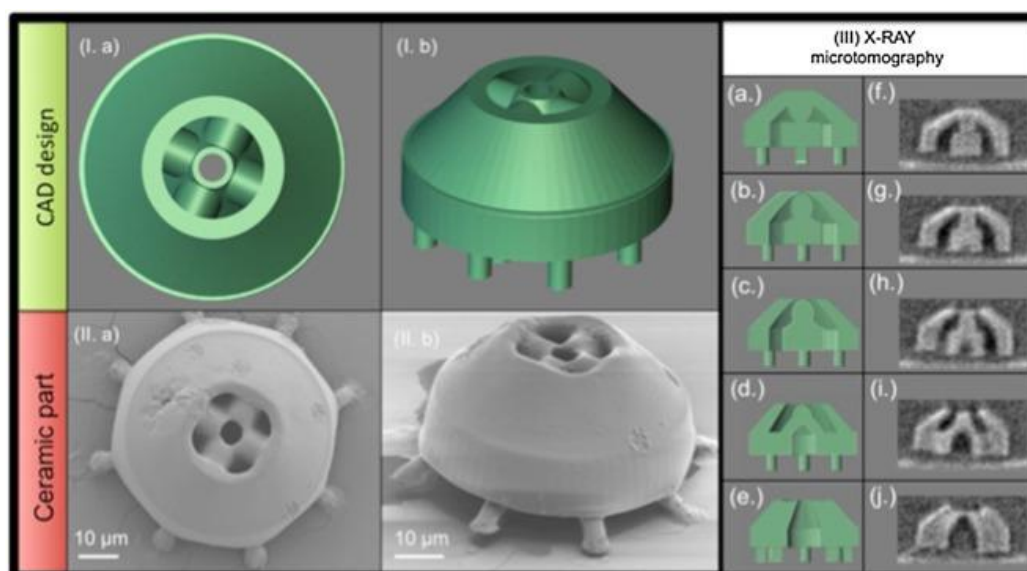
Figure 2.15: The CAD design (I.a and I.b) of the nozzle compared with the final pyrolysed part (II.a and II.b) and SEM images at 0° and 60°. In III (a-j), X-ray micro-tomographic sections of the nozzle are presented and compared with the illustrated cross sections of the nozzle.

By X-Ray micro-tomography with 0.7 µm resolution, we confirmed with the Figure 2.15 III. that the fabricated internal capillaries (∼6-8 µm) did not collapse or block after development or pyrolysis. To our knowledge, this nozzle is the first two-photon fabricated ceramic microstructure where high aspect ratio capillaries survived after development and pyrolysis. Since SiOC ceramics are well known for their mechanical properties and resistance in harsh environments [93], the micro-nozzle tip can be considered as a promising candidate for microdroplets delivery for low viscosity liquids. In this example, the nozzle tip was fabricated on the quartz slide with support structures (pillars) for demonstration purposes. However, it would be also possible to fabricate the nozzle tip directly on the tip of a tube for producing a complete nozzle. By modifying the initial design of the nozzle tip, it would be also possible to attach it properly.

2.5   Conclusion

In this chapter, we investigated the polymerization parameters of a commercially available polysiloxane resin. This resin was prepared by incorporating a two-photon

active photoinitiator and 3D printed with a Nanoscribe Professional GT 3D printer. The printed green body was then developed and pyrolysed in inert atmosphere up to 1000 °C to yield silicon oxycarbide ceramic microstructures (<200 × 200 × 200 μm^3). We observe an isotropic shrinkage with a linear shrinkage value between 32-38% which implies high-controllable ceramics manufacturing. This low shrinkage is attributed to the molecular structure of this preceramic polymer, which results in extensive crosslinking and leads to high ceramic yield.

By optimizing the fidelity of prints using an appropriate combination of exposure dose, hatching and slicing distance, the porosity fraction of these ceramic structures was found very low as demonstrated after synchrotron tomographic imaging and the roughness measured by Atomic Force Microscopy is found to be <100 nm for the final ceramic parts. Based on the results obtained from the test cuboid structures, a specific printing configuration was selected for the fabrication of complex 3D structures and finally a micro-nozzle tip was printed and pyrolysed successfully.

Until now, mostly scaffolds and photonic crystal microstructures have been printed with two-photon polymerization of PCPs with a mentioned linear shrinkage >50%. We demonstrated a ceramic-based micro-nozzle, which could find applications in micro-droplets delivery in harsh environment.

Chapter 3   Smooth and fast microfabrication with a two-photon endoprinter

In this chapter, my work in the microfabrication with a two-photon endo-printer is presented. Specifically, I report the fabrication of smooth microstructures fabricated through an optical fiber by two-photon polymerization. I further present fast microfabrication by point-spread-function engineering. This chapter is part of a manuscript entitled:

"Improved two-photon polymerization through an optical fiber using coherent beam shaping", Georgia Konstantinou, Antoine Boniface, Damien Loterie, Eirini Kakkava, Demetri Psaltis and Christophe Moser

submitted to Additive Manufacturing journal, Elsevier.

3.1   Background

Since the pioneer work of Kawata et al. [56] in 1996, two-photon polymerization (TPP) has experienced spectacular progress and represents now a tool of choice in various fields for fabricating ultraprecise 3D microstructures with up to nanoscale resolution [126]–[139]. A key benefit of TPP is its ability to restrict polymerization to a tiny focal volume or voxel thanks to the non-linearity of the photo-initiator, that requires the simultaneous absorption of two photons to trigger the cross-linking of the resin [128], [134], [140].

Despite these advances, there are limits in the fabrication such as access to confined spaces for which it is difficult to bring the focused light due to the bulky objectives. As an alternative, Morales et al, in our group proposed to use an optical fiber with a sub-millimeter diameter to replace a microscope objective [29], [30]. Among single-mode, multicore and multimode fibers, the latter provides the largest amount of optical modes per area and thus a higher resistance to optical material damage by high power lasers [141]–[143]. Consequently, multimode fibers are the most suited for endo-printing applications. However, the propagation of coherent light through multimode optical fibers creates an intricate figure of interferences at the fiber output also known as speckle.

Furthermore, when using ultrashort pulse of light, the dispersion of the fiber broadens the pulse temporally, which decreases the peak intensity of the pulse and can considerably reduce two-photon absorption efficiency. Although the pulse may be strongly distorted both spatially and temporally, the propagation of light through the fiber is linear, for an intensity below a given threshold, and deterministic and the output speckle field can be expressed as a linear transform of the input field.

Owing to the availability of spatial light modulators (SLM), several wavefront shaping techniques have been developed over the past ten years to manipulate in both, space and time, coherent light at the output of complex media such as scattering materials, biological tissue or multimode fibers [65], [67], [144]–[152].

These wavefront shaping techniques are able to focus light in space and time after propagation through a multimode fiber and in particular, a Digital Optical Phase Conjugation (DOPC) technique has been used to print, via two-photon absorption, a 3D micro-pyramid of base size 89 µm x 89 µm with a 1 µm lateral printing step [29]. DOPC consists of correcting the incident wavefront by recording the scattered light field globally and then playing back the conjugate light field by a SLM. This is illustrated in Figure 3.1.a. However, DOPC [29] requires stringent and precise alignment (pixel-by-pixel alignment between the SLM and the camera) which can be very challenging. In addition, the calibration of the fiber is position-dependent, which means that each focus spot requires its own calibration pattern. This becomes impractical when the print is performed with a small hatching distance (i.e. high resolution). The 3D print in [29] had 1 µm hatching distance which resulted in disconnected voxels.

In this chapter, I have selected the Transmission Matrix method (TM) which consists of sending a set of input patterns and recording the fiber output patterns. The matrix that relates the input to the output is then computed from the set of patterns (see Chapter 1). Once the matrix is computed at several depth plane, an arbitrarily large number of spots can be computed in 3D within the fiber field of view. The TM calibration method has been used with a continuous wave beam for single photon three-dimensional microfabrication [30] and with femtosecond pulses for ablation purposes [153], [154]. This is illustrated in Figure 3.1.b .
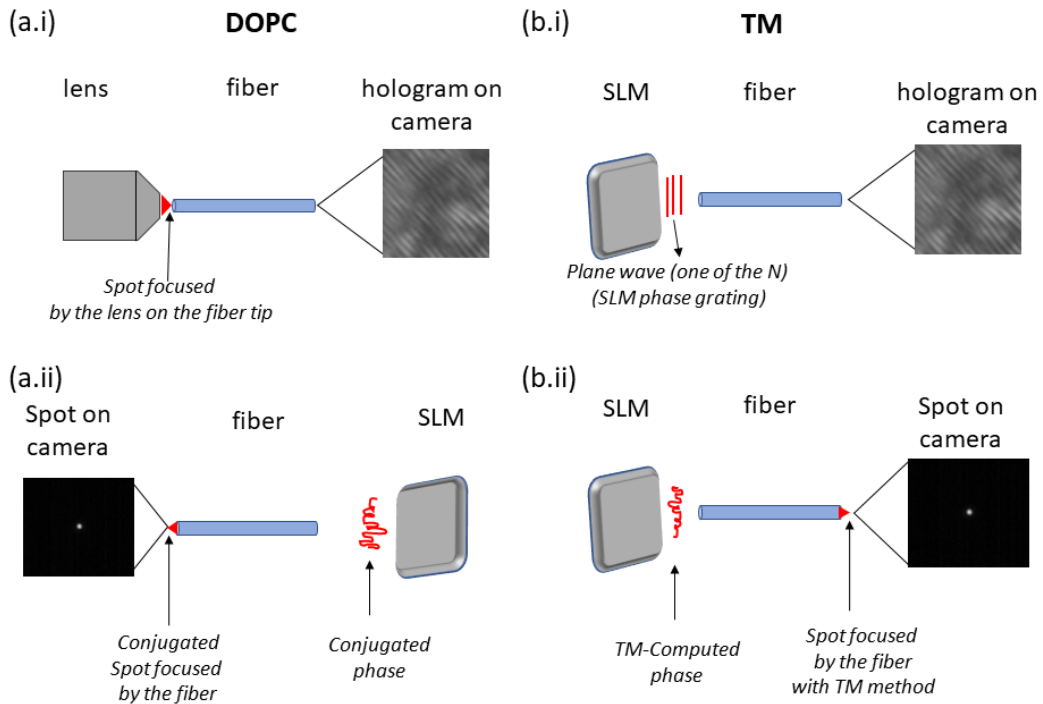
Figure 3.1: (a.i) The calibration step in Digital Optical Phase Conjugation, (a.ii) The reconstruction step in Digital Optical Phase Conjugation, (b.i) The calibration step in Transmission Matrix method showing only one of the N plane waves sent by the Spatial Light Modulator, (b.ii) The reconstruction step in Transmission Matrix method, where the phase is computed to produce the desired pattern.

Compared to other techniques, the TM offers more flexibility in terms of spatial control of the focus spot at the output of the fiber [155], where the photoresist is located. To illustrate this, we show the possibility of printing with diffraction-limited spots but also with multiple foci that results in an extended point-spread function and thus shorter printing time.

We show experimentally that with such approach, the hatching of the voxels and the distance between two consecutive spots can be easily adjusted for either obtaining a smoother and more accurate structure or for achieving faster fabrication. We further demonstrate that the smoothness is improved by using an optical shutter, which is used to prevent transient effect in pattern loading of the SLM, which produces fluctuation in exposure dose.

The chapter is organized as follows: we first present the optical setup, the calibration procedure, the printing method by wavefront-shaping and illustrate the results by 3D printing simple objects. We show the measured optical characteristics of the focused spot at the tip of the fiber, such as spot size, intensity, and dose correction. We present the results with and without the shutter and with and without exposure dose correction and compare the smoothness of square prints. Finally, we show the fabrication of a wood pile structure to illustrate the 3D fabrication potential.

3.2   Experimental setup and methods

We present the fabrication of 3D microstructures through two-photon polymerization by using the TM method and a graded-index (GRIN) multimode fiber with a graded index lens attached to its tip in order to increase the numerical aperture to 0.4. Using the transmission matrix to calibrate the fiber, gives the flexibility to alter the spot size of the focus spot. The hatching distance and the spot size of the focus can be modulated to target either smoother and more accurate structure or faster fabrication.

At first, we present the optical setup, the calibration procedure and the printing method by wavefront-shaping. We then show the measured optical characteristics of the focused spot at the tip of the fiber, such as spot size and intensity. We demonstrate a single focused spot and an elliptical focused spot thanks to PSF engineering, and we illustrate the scanning method.

We further explain in which way the shutter is utilized to improve the smoothness of the structures by providing detailed information about the SLM flickering and we apply the exposure dose correction method voxel-by-voxel. We present the results with/without the shutter and with/without exposure dose correction, and we

compare the smoothness of simple prints by using the PSF-engineering approach as well.
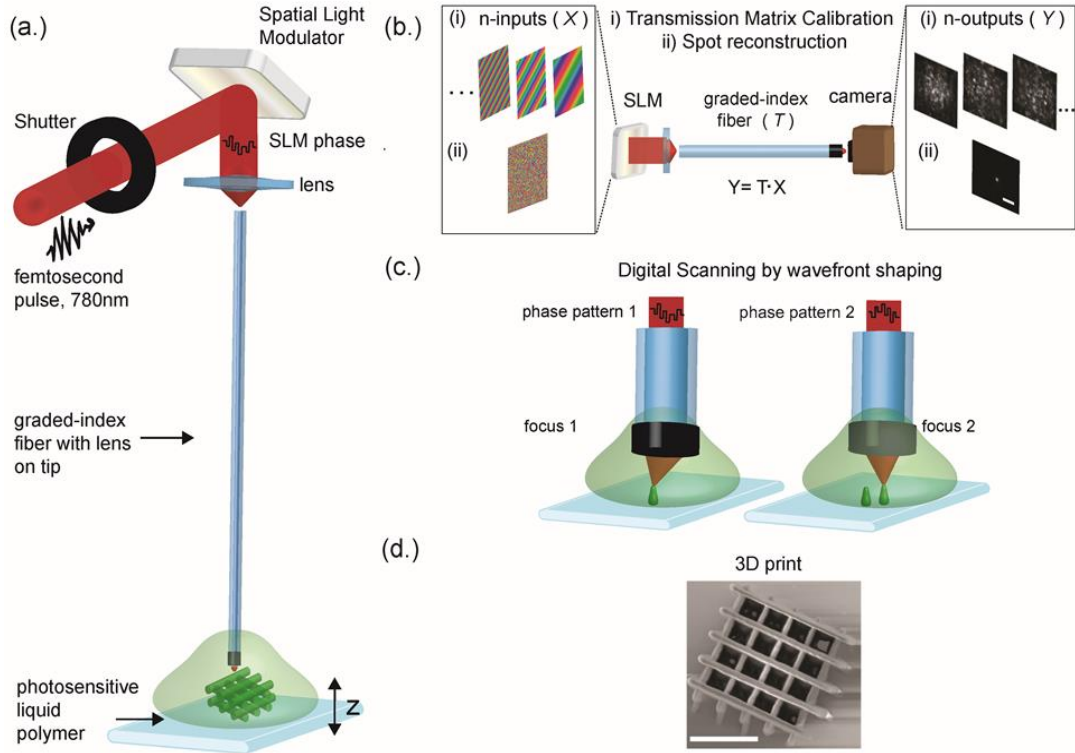
Figure 3.2: (a) The two-photon endo-printer, the slide is moved in z direction with a motorized stage (b) The transmission matrix calibration method, (c) two generated spots illustrating the scanning method and (d.) 3D-printed woodpile.

Finally, we show a 3D printed structure fabricated with the previously mentioned method. In Figure 3.2 the working principle of the fiber 3D-printer is presented. In Figure 3.2.a, the illustration of the fiber used for printing a microstructure is shown and in Figure 3.2.b we explain the Transmission Matrix calibration method, which is used for the characterization of the medium (optical fiber). We additionally illustrate two generated focused spots at different locations such that the digital scanning through the SLM is clarified. In Figure 3.2.d an example of a 3D print is presented.

In two-photon polymerization, two photons are absorbed simultaneously from the atom in the photosensitive resin and the valence electron "jumps" from the ground to the excited state by absorbing the energy $\Delta E = E_1 + E_2$, as explained in paragraph 1.3.1.

I use a MaiTai DeepSee (eHP) femtosecond laser by Spectra Physics. It is a Ti-Sapphire femtosecond laser (mode-locked), with pulse duration <70fs, repetition rate 80MHz, average power 2.9 Watts, operating at 780nm so that it fulfills the requirement of two-photon absorption by the negative tone photoresist (IPL-780 Nanoscribe) and its polarization is horizontal. For wavefront-shaping, I use a phase-only reflective, spatial light modulator (PLUTO-2.1 by Holoeye). It has 1920pixels x1080 pixels with 8 μm pixel pitch. The fiber used is a graded index multimode fiber with core diameter 400 μm and 560 μm cladding diameter and a graded-index lens attached on the fiber tip. In this way, the numerical aperture increases (the reported fiber NA was found 0.37, thus lower than the value in the specifications of the Edmund GRIN microlens (0.54)). A GRIN lens was selected instead of step-index MMF because of the lower modal dispersion.

Transmission Matrix calibration step:

I use the Fourier basis as explained in chapter 1. A set of plane waves (~ 27500 inputs in this system) is generated by the SLM (Figure 3.2.b) and coupled in the optical fiber resulting in a speckle pattern at the fiber output because of modal dispersion.
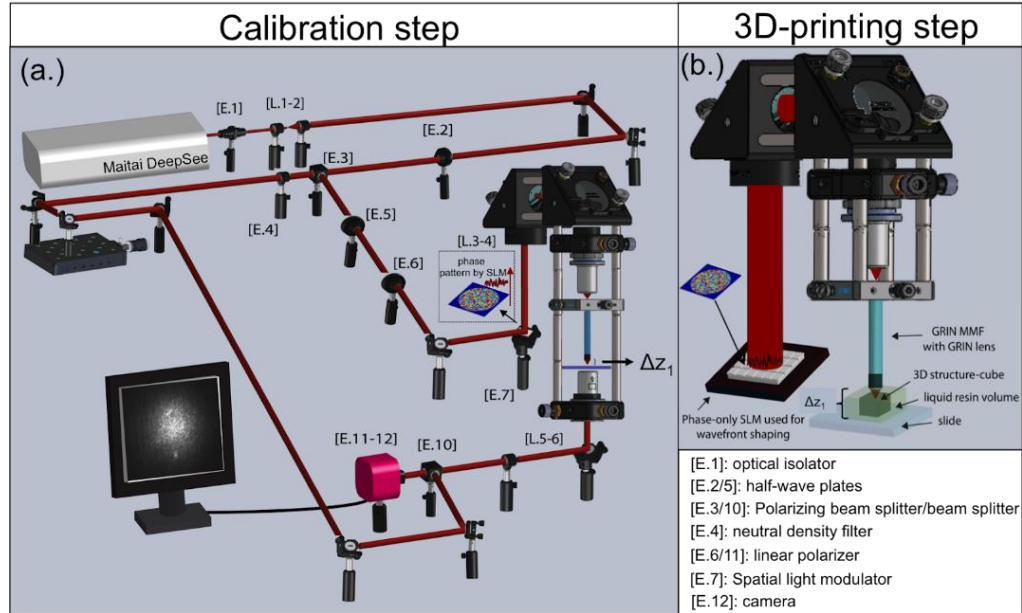
Figure 3.3: (a.) The TM calibration step. In E.3 the beam is divided in two arms, which meet again and interfere through E.10 on the camera plane (E.12). The Transmission Matrix measurement is completed when the pair of sets inputs-outputs is collected, (b.) The 3D-printing step zoomed highlights the specific phase pattern which results a focused spot at the output of the fiber when the calibration step is completed. At this step the reference arm is blocked.

This number of plane waves is close enough to the number of fiber modes (~26800 modes) [50]. Each output pattern is interfering with a reference arm to obtain a corresponding set of holograms (outputs) by off-axis holography. By knowing the set of inputs [X] (phase gratings) and recording the set of outputs [Y] (intensity images), the Transmission Matrix [T] can be calculated ([Y]=[T][X]) [148], [156].

The off-axis holograms are time-gated by the reference femtosecond laser beam implemented with a spatial delay line. A detailed version of the experimental setup that I built is presented in Figure 3.3.

The recorded holograms are intensity images captured on the camera. However, the phase information is also recorded through the fringes of the hologram. To obtain interference, both arms need to have the same polarization. For this reason, a second half waveplate (E.5) is placed in the object arm to rotate the linear polarization to match that in the reference arm. The linear polarizer (E.6) and the half waveplate (E.2) are used so that the ratio between the object and reference is tuned properly. The beam is collimated in both arms and in all cases 4f systems are used.
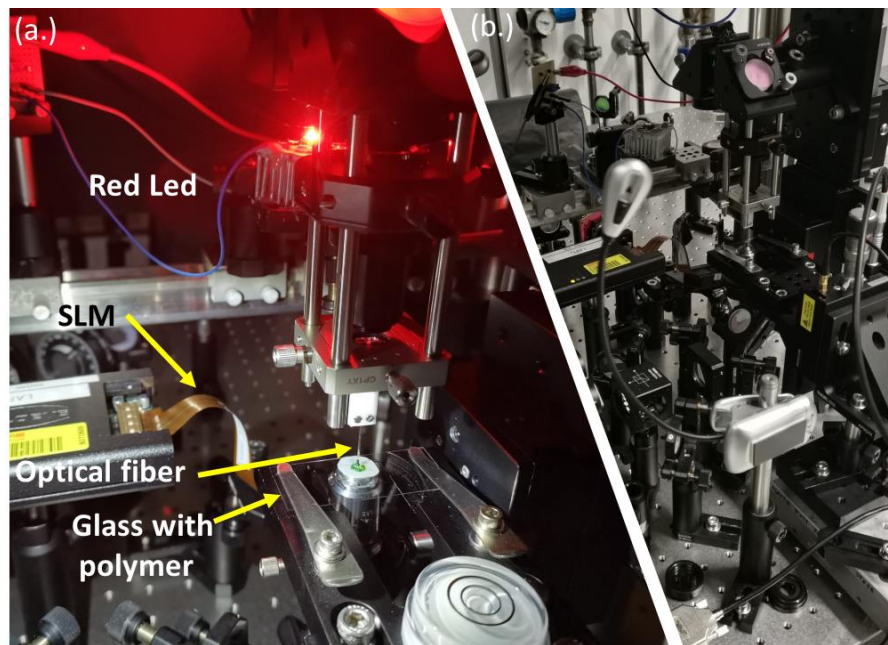
Figure 3.4: (a.) Close look at the components of the endo-printer (SLM, fiber, glass with polymer). The red led is added after the end of a printing test so that we check if the printing was successful, (b.) A part of the setup with the cage system which includes the fiber.

We measure the Transmission matrix of the system that includes a borosilicate coverslip (180 µm) and the liquid polymer in which the MMF is dipped. The coverslip covered with a drop of the photopolymer resin is 40 µm lower than the facet of the fiber. Temperature, air fluctuations inside the room, vibrations on the table or changing room light conditions while the TM measurement takes place, can affect the measurement and the efficiency of the printing system. Hence, care was taken to minimize these effects during calibration and printing. Figure 3.4 shows images of the set-up.

Once the calibration step is completed, the calculated Transmission Matrix can be used to compute which input projected by the SLM provides a desired output (Figure 3.2.c and Figure 3.3.b). In Figure 3.5, we briefly present the steps to measure the time-gated Transmission Matrix. Interference fringes occur when the object and reference beam are overlapping within the coherence length of the beams.
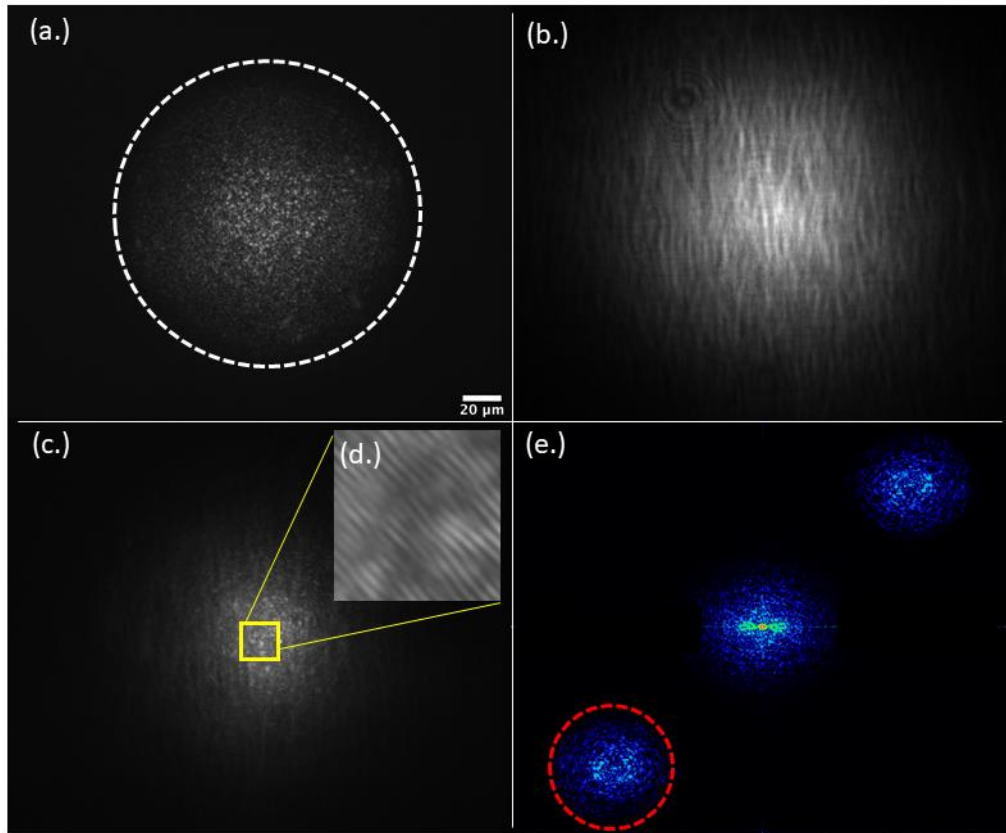
Figure 3.5: (a.) Speckle pattern at the output of the graded-index multimode optical fiber. The circumference of the optical fiber grin lens tip is denoted with a white, dashed-line circle, (b.) Intensity image of the reference beam on the camera, (c.) Interference pattern between the two beams on the camera, (d.) zoom of the interference pattern where the fringes can be observed, (e.) Fourier Transform of the interference pattern in (c.), the object term (+1 order) is filtered. Scale bar 20 µm.

The delay line of the reference beam is scanned until fringes are seen on the camera. Because of the modal dispersion incurred by the propagated beam inside the fiber, the pulse is spread in time and hence the short reference pulse (100 fs) essentially time selects the modes which have similar modal dispersion.

The fringes in Figure 3.5.d provide the phase information that we use in the Fourier space (equation e.6). For each input (plane wave), an output interference pattern with fringes is recorded by the camera. The number of modes for this GRIN MMF is ~26800 and thus we use a number of plane waves slightly larger, 27500, to make sure we sample all modes.
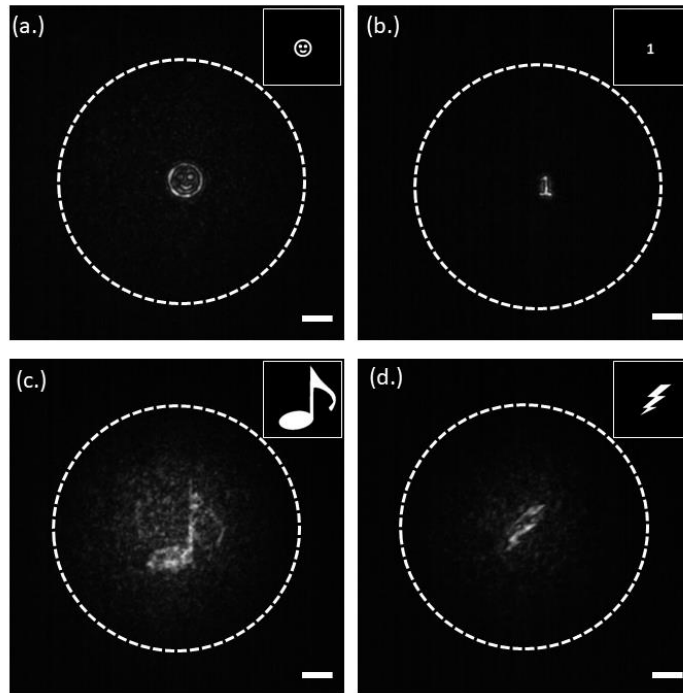
Figure 3.6: (a.) a smile projected at the fiber output, (b.) number 1 projected at the fiber output, (c.) a musical note, (d.) a thunder, scale bars 20 μm. On the top right of each projection the ground truth figure is shown (300 pixels x 300 pixels).

In Figure 3.6, we present examples of patterns projected at the output of the fiber by using a femtosecond laser. Each output corresponds to a different calculated phase pattern through the TM.

In additive manufacturing by two-photon absorption, the highest peak intensity is ensured when the desired pattern is a tightly focused spot on the fiber output. Consequently, the SLM projects a phase-pattern that results in a focused spot at the end of the fiber-grin lens. The focusing efficiency of the spot, defined as the ratio of

the light power in the main focusing lobe divided by the light power overall, is found to be larger for the TM method, compared to DOPC thanks to less complex alignment between the hologram detector and the SLM. This means less waisted light potentially heating the photoresist [64].

The graded-index multimode fiber fabricates the 3D-microstructure by scanning the spot inside the negative-tone photoresist in a bottom-up fashion. During the printing procedure, the reference beam is blocked, and the camera used for the recording of holograms, now monitors the scanning of the spot (Figure 3.3.a and b). At the end of the scanning, a light beam shutter, which is placed on the object arm, is closed.

We temporarily insert a red LED lamp between the SLM and the first element of the cage (lens) to illuminate with incoherent light the sample through the fiber. We verify if the photoresist was polymerized and if the printed structure indeed was attached on the surface of the slide. This in-situ monitoring contributes to the immediate feedback about the success of the print (Figure 3.4.a).

After the end of printing, the slide is removed from the experimental setup and is washed with the solvents PGMEA (~15 minutes) and isopropanol (~5 minutes). In this way, the unexposed photoresist is removed, and the cross-linked, solidified structure remains attached on the slide.

The TM method enables the same light manipulation flexibility through an optical fiber as through a microscope objective with a phase or amplitude modulator. The latter was demonstrated by Zandrini et al. who used a spatial light modulator to produce multifoci [157], and by Somers et al. and Manousidaki et al with a 2D pattern projection [158], [159]. Similar works were presented by Yang et al, Kim et al, Liu et al and Geng et al. [160]–[164].

The highest peak intensity is obtained when output light is tightly focused to a diffraction-limited spot. In this case, the SLM projects a phase-pattern that produces the smallest possible spot one can get at the output of the fiber-GRIN lens. In our system, a focusing efficiency of 11% is enough for obtaining a peak intensity above the polymerization threshold of the material (~45 GW/cm^2). In Figure 3.2.c, the printing step is illustrated. The generated focal spot is a few tens of micrometer away from the fiber-grin lens facet (denoted as Δz_1 in Figure 3.3) so that the polymerized material will not attach nor stick on to the fiber tip. This is achieved by measuring the TM on a plane, which is a few tens of μm away from the fiber tip.

3.3 Results

As it was previously reported, when the Transmission Matrix measurement is completed, it is possible to compute the phase pattern that results a specific output on the fiber tip. We select to present the lateral and axial PSFs of two different outputs in Figure 3.7, generated 40 µm away from the fiber facet. The first one refers to a circular spot and the second one is an elliptical spot. The elliptical spot is generated by projecting three circular spatially distant spots simultaneously.

In Figure 3.7, we show both XZ and YZ planes because they are not identical in the case of the elliptical spot. The PSFs presented in Figure 3.7 were measured in air without any glass or liquid. The image plane was 40 µm lower than the fiber facet so that it was possible to scan along z direction with an imaging objective with NA 0.65. We additionally show the squared PSFs because of the squared intensity in two-photon polymerization. In the circular PSF, the FHWM of PSF_{xy} and PSF_{xy} ^{2} were found to be 1.1 µm and 0.8 µm respectively and the FWHM of PSF_{yz} and PSF_{yz} ^{2} were found to be 9.2 µm and 6.9 µm respectively. Using the *e. 3* : (λ/(2NA) =1.1), we calculate that the NA is 0.351. This reveals that despite the attached microlens with NA 0.54, this NA is not exploited as expected theoretically based on the microlens specifications. This could be explained by the selected modes of the fiber by time gating.

In Figure 3.7 (iv), we demonstrate the x- scanning step of the spots, which is 200nm. For the circular spot, the y-scanning step is the same (200 nm), whereas for the elliptical spot the y- scanning step is 1 µm aiming faster fabrication. The elliptical spot is generated as a combination of three different circular spots, which are generated at the same time with 2 µm distance between the first and the third one.

 The y-scanning step was selected to be half of the long elliptical radius (1 µm). Each one of the two PSFs is used for two-photon polymerization but for different purposes. The circular PSF is used for fine x-y scanning and for the fabrication of smoother surfaces and the elliptical PSF is used for cases where faster micro-manufacturing is needed.
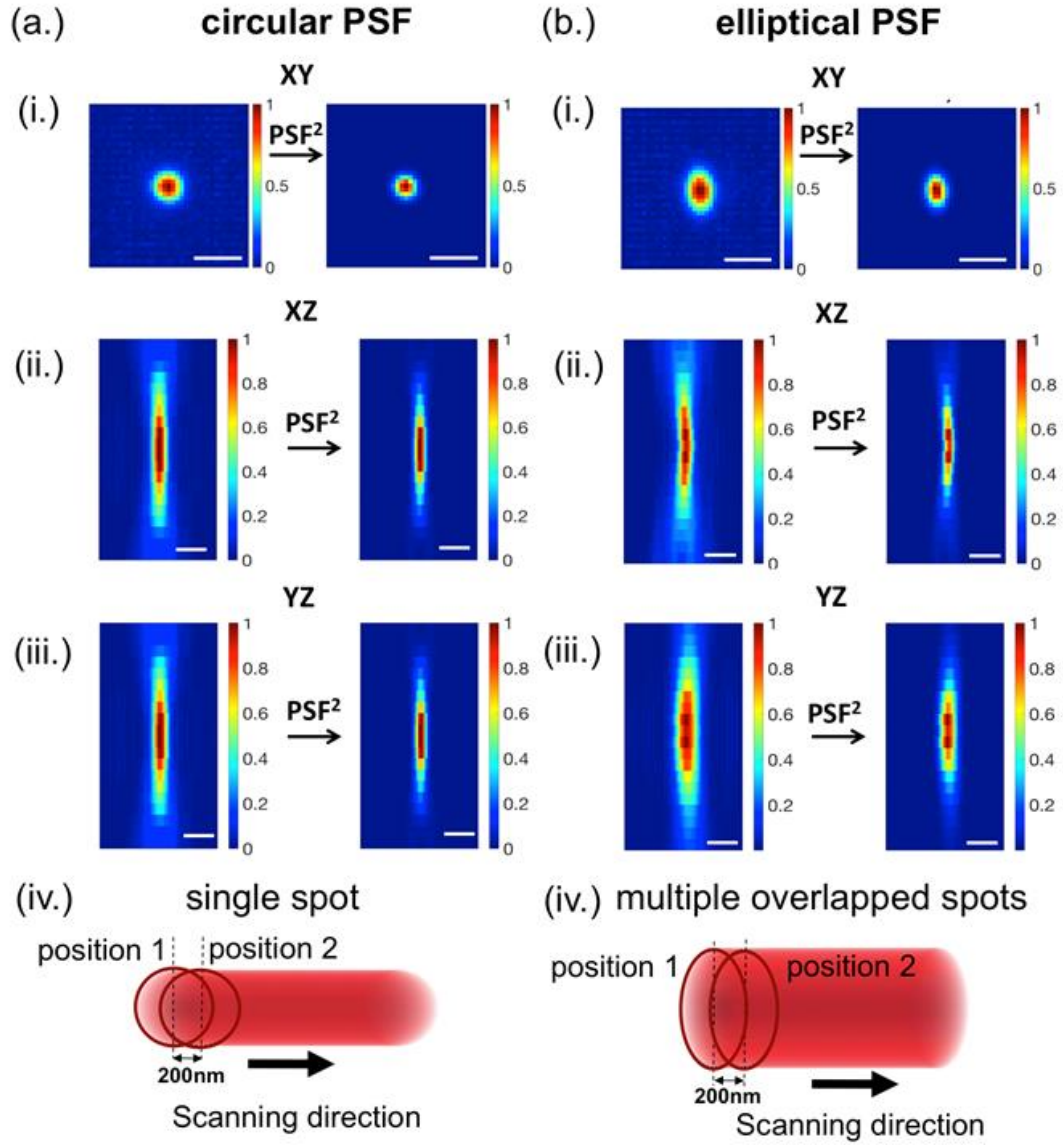
Figure 3.7: (a. i-iii) lateral and axial PSFs of the circular spot, (b. i-iii) lateral and axial PSFs of the elliptical spot, scale bars 2 μm.(a, b.iv) the scanning test with 200nm x-scanning step is illustrated.

A focused spot can be generated at different positions along the FOV of the GRIN microlens, attached on the fiber tip. The focusing efficiency on the central area of the lens is higher than near the edges because the whole NA is exploited in the center. In Figure 3.8, a few generated spots along the fiber FOV are presented and for two of them, the focusing efficiency is provided. The focusing efficiency (f.e.) is defined as the percentage of the total output power that is concentrated in the focused spot.
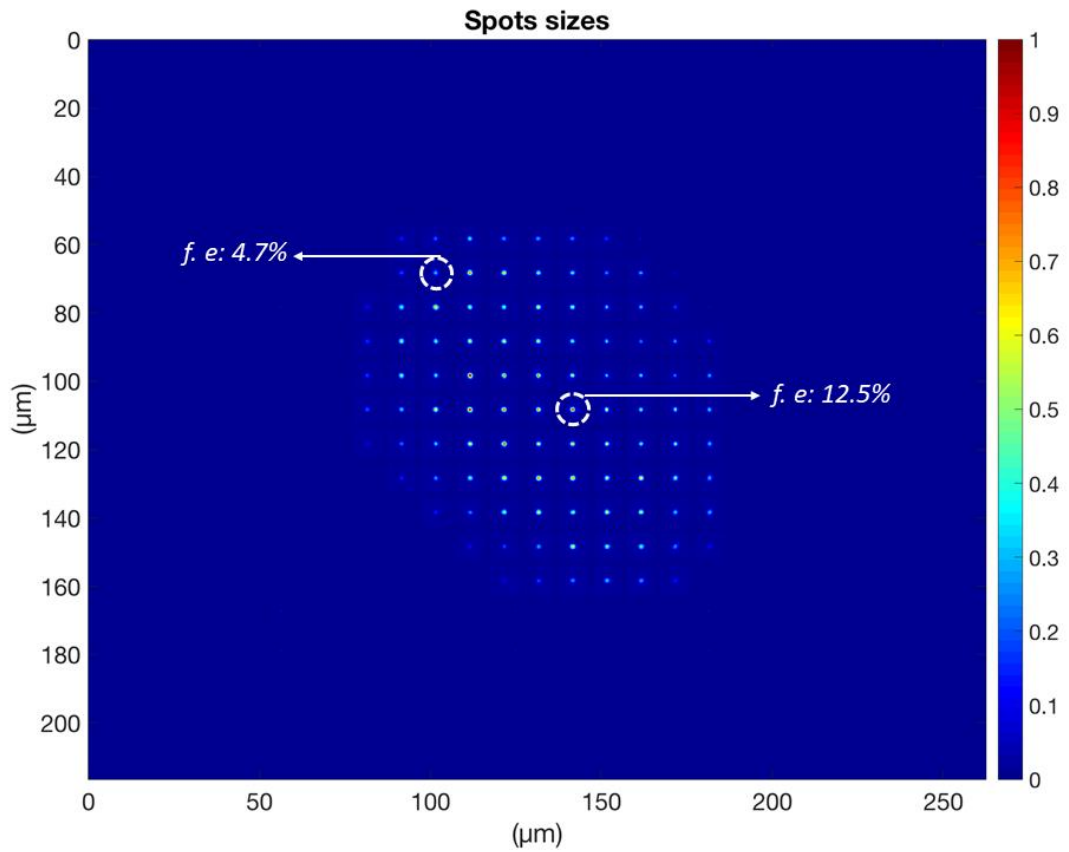
Figure 3.8: A few spots are scanned with 10 μm step and are stacked on the same figure. The focusing efficiency of the spot in the central area of the fiber is higher than in the areas near the edges.

There is a focusing efficiency gradient from the center toward the edge. This is demonstrated with the intensity distribution map with a smaller step in Figure 3.9. If an equal exposure time is used, this means that the same available power at the fiber output can result in a larger voxel printed in the central area than towards the edge. A large printing area of 80 μm with very fine step (200 nm) would require a lot of time to be fabricated because of the refresh rate of the specific SLM (20 Hz), which would be further increased after applying exposure time correction for homogeneity purposes on the printed layer. With a faster SLM, such an area of 80 μm x 80 μm could be printed with high resolution.

For this reason, we select to investigate the printing performance on a small print fabricated at the central area of the fiber. A single-layer square is printed several times. In the first case, no shutter is used in the system. The phase pattern loading transient and flickering of the SLM pixels (phase fluctuation due to electric

polarization of the liquid crystal molecules for this SLM model), is shown to affect the roughness of the square even if it is printed in the central area of the FOV.
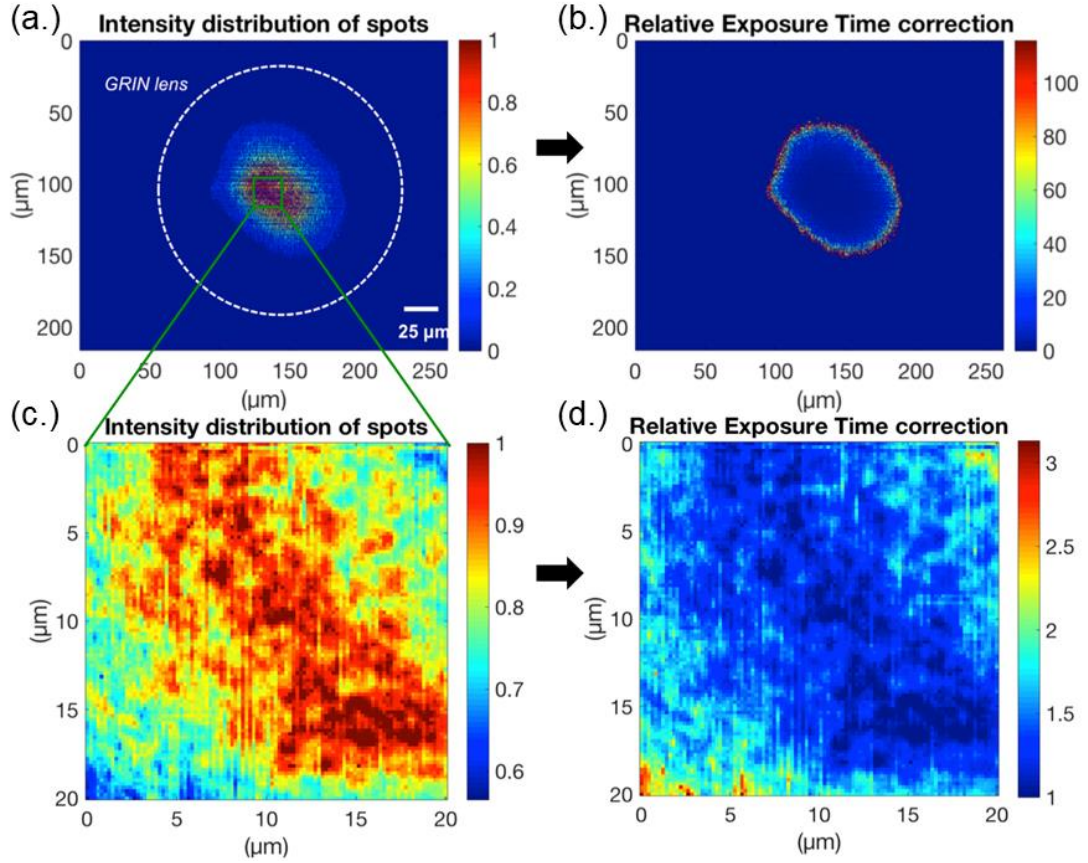
Figure 3.9: (a.) The normalized intensity distribution of spots, scale bar 25 µm, (b.) the relative exposure time correction along the scanned area, (c.) The normalized intensity distribution of a smaller square-area (20 µm x 20 µm), (d.) The relative exposure time correction for the same area of (c.).

In the second case, a shutter is used to block the laser beam during the rise time of the SLM (time until the pattern is loaded completely onto the device) and until the average flickering intensity at the focus shows minimum fluctuations by averaging. In the third case, an exposure time correction is additionally applied.

Figure 3.9 shows the intensity distribution of the focused spots along a large fiber FOV (with step 5 µm) and the corresponding relative exposure time correction which must be applied so that the dose is the same for all spots [165], [166]. We repeat the same procedure with fine step (200nm) for the square structure (small structure denoted in green in Figure 3.9.a).
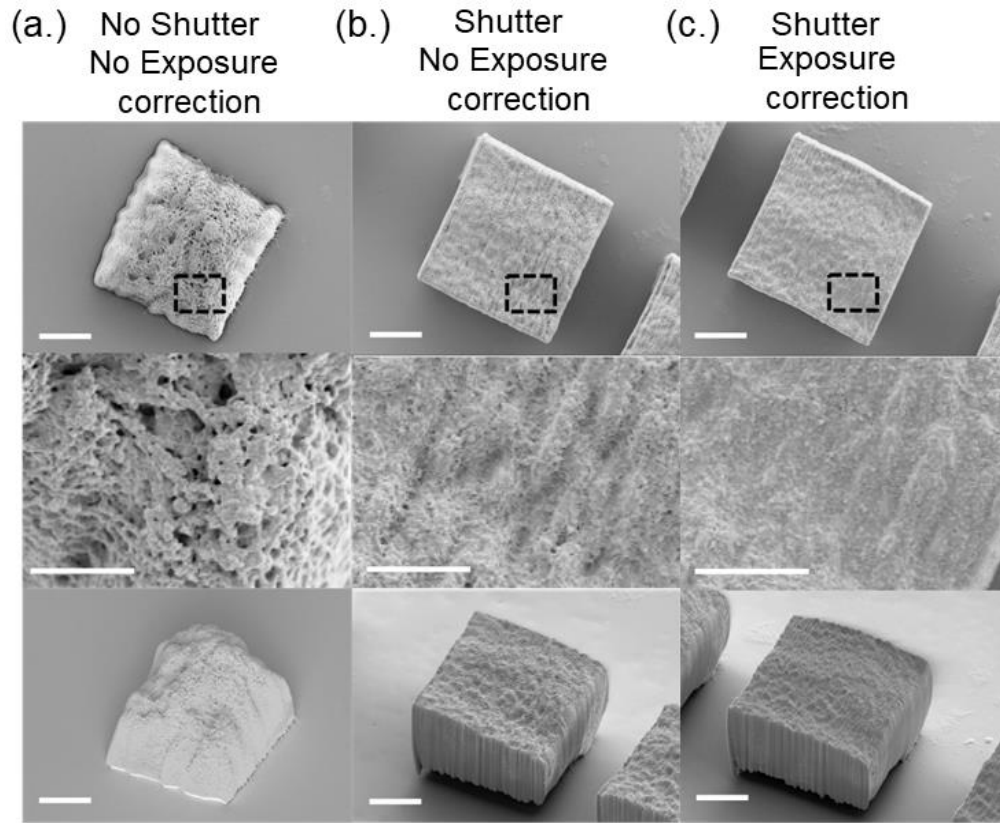
Figure 3.10: (a.) The normalized intensity distribution of spots, scale bar 25 μm, (b.) the relative exposure time correction along the scanned area, (c.) The normalized intensity distribution of a smaller square-area (20 μm x 20 μm), (d.) The relative exposure time correction for the same area of (c.).

The printing results of these cases are presented in Figure 3.10. The smoothness, highlighted in the second row of Figure 3.10, is notably improved from (a.) to (c.). The exposure time per voxel (single focused spot) is in the range of τ= 100 ms for all cases and the available power on spot is 12mW.

For the case (a.) the printing time is ~17 minutes. For the cases (b.) and (c.) the printing time is longer (~29 minutes) because of the fine exposure time corrections and because closing the shutter for 70 ms per spot adds extra time in the whole printing process.

The shutter is used to block the rise time of the SLM including the first periods of the SLM until the averaging of the flickering amplitude is stabilized around a specific value.
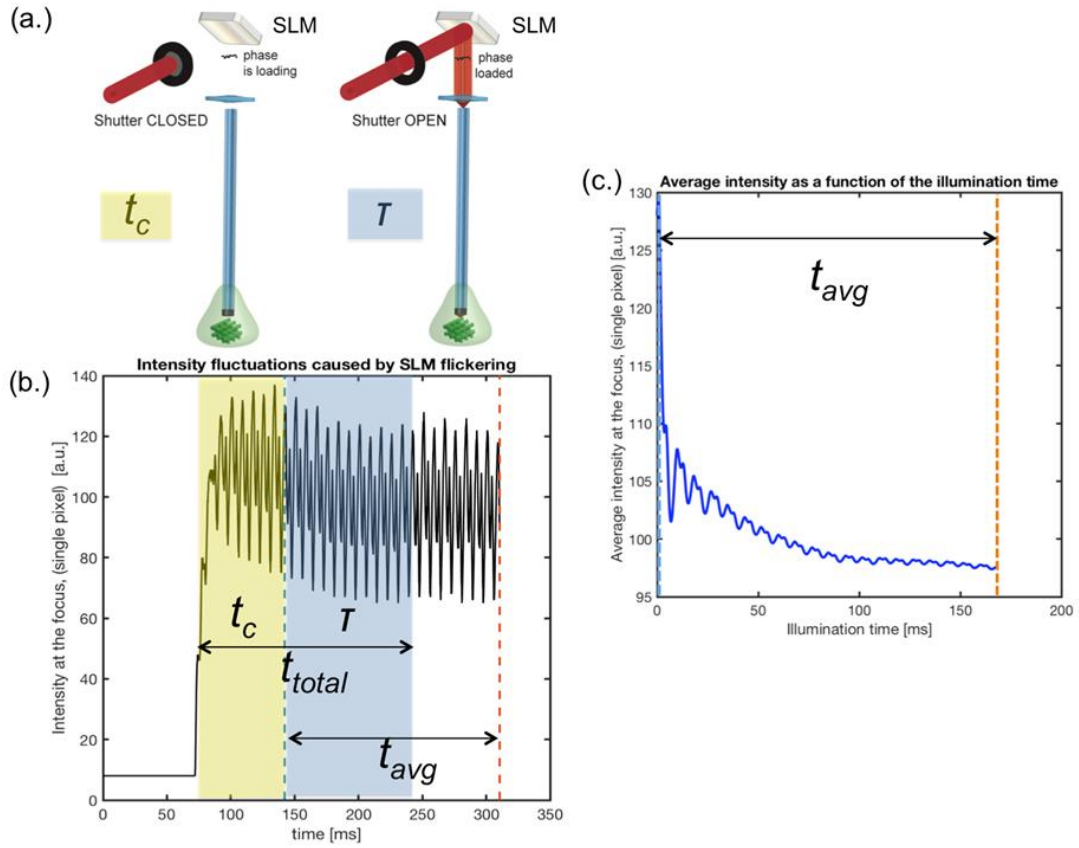
Figure 3.11: (a.) The blocking step is illustrated while the SLM pattern is loading, (b.) the flickering of the SLM is presented and the total time spent per spot t_{total} is 170ms, (c.) The average intensity as a function of the illumination time proves that an exposure time of τ= 100ms is a proper selection for ensuring improved smoothness.

After that, by averaging the intensity as a function of the illumination time, averaging for an exposure time of ~100ms results in nearly constant average intensity. This is illustrated in Figure 1.1.

We deduce that the shutter is necessary even when using other SLMs with non-negligible flicker to avoid transient effects. However, SLMs with higher refresh rate would provide faster fabrication and larger build volumes.

In Figure 3.12 we present two squares printed with the two PSFs (circular and elliptical) described in Figure 3.7. The elliptical PSF provides faster printing (6 minutes) with lower resolution compared to the circular PSF (29 minutes) because the spot size and the y-scanning step are larger. The y-scanning steps explained earlier are also illustrated in the first row of Figure 3.12.
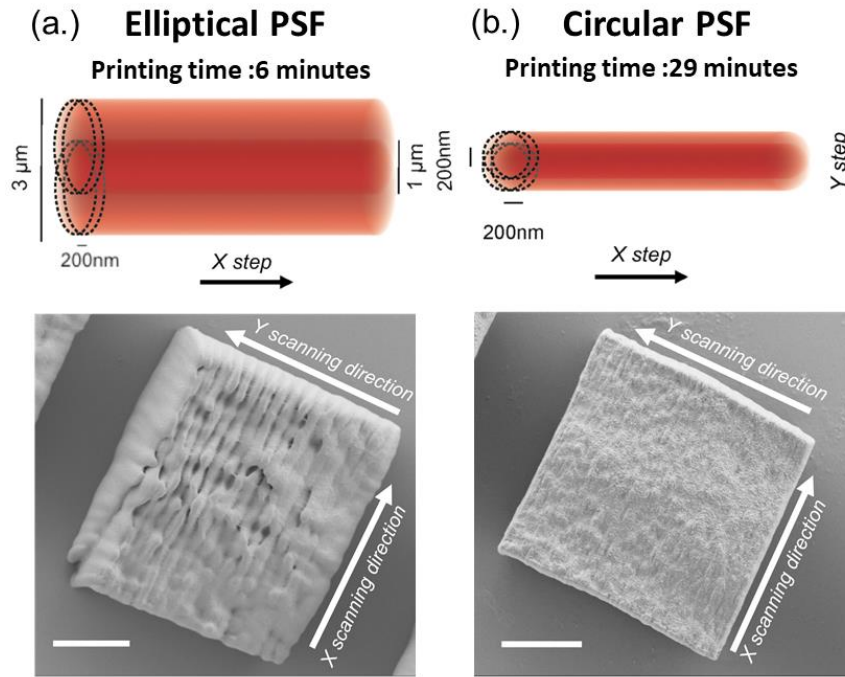
Figure 3.12: (a.) Representation of elliptical PSF scanning and corresponding printed square, (b.) Representation of circular PSF scanning and corresponding printed square, scale bar 5 μm.

Finally, a woodpile is fabricated and presented in Figure 3.13. We show the 3D model, the printed structure imaged by Scanning Electron Microscopy with two-different angles and lastly a zoomed image where the width of a woodpile line is presented to underline the combination of high resolution and improved smoothness compared to the results obtained by DOPC. The total printing time of the presented woodpile is 3.4 minutes. The power provided on the system was 12mW, which corresponds to a dose 1.9 J/cm^2, by applying the approximation for the dose calculation presented in [113].

We can observe that the cumulative dose along z has obvious effect on z-resolution because of the voxel aspect ratio and the selected layer-by-layer step (axial overcure). For this reason, the bottom and top layers are almost connected to each other along z. However, we can observe the voxels on the second layer, which is on the perpendicular direction to the 1st and 3rd layer. The layer-by-layer step was selected to be half of the voxel height (5 μm) so that it is certain that the layers will not collapse after washing (best adhesion possible). The cumulative dose however along z explains that the washing was more efficient along xy plane (hollow squares) than along z direction.
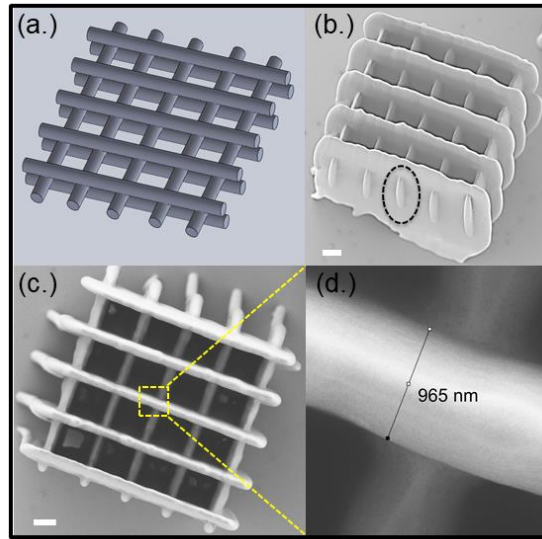
Figure 3.13: (a.) the 3D model of the woodpile, (b.) the printed woodpile imaged by SEM in an angle, the voxel height in the dashed circle is 10.7 μm, (c.) the woodpile imaged from the top and (d.) a selected area imaged with higher magnification. All scale bars 2 μm.

The FWHM of the circular PSF[2] in the axial direction is 7 μm and 0.8 μm in the lateral direction. This confirms the results of the printed structures, imaged by Scanning Electron Microscopy (SEM) with resolution ~5nm, in Figure 3.13.b and Figure 3.13.d. The lateral and axial smoothness of the prints is vastly improved compared to previous work by Morales et al [29]. Along the x-scanning direction of the squares, the smoothness is better than in y-scanning direction (3rd row of Figure 3.10). Along the scanning in the x-direction, the voxel-by-voxel lateral overcure is more efficient because the elapsed time between two consecutive voxels is a lot shorter compared to the time between the first voxel of the line i and the first voxel of the line i+1 (y-scanning direction). This can be justified from Figure 3.12.a as well. By using a microlens with higher NA attached on the fiber tip, higher resolution can be achieved [167], [168].

For this purpose, I designed and fabricated a lens based on the work of Bianchi et al. [167], with dimensions matching the core diameter of the GRIN fiber I am using, to increase the NA from 0.29 (fiber NA) to 0.96. The outer surface of the lens is parabolic, and the internal surface is an arc of a circle. Multiple iterations of CAD design and Zemax simulations were run until we observe focusing ~10 μm away from the lens tip. In Figure 3.14, a schematic is shown in (a.) along the Zemax ray-tracing simulation in (b.). In Figure 3.14.b, the NA was found 0.96 geometrically.
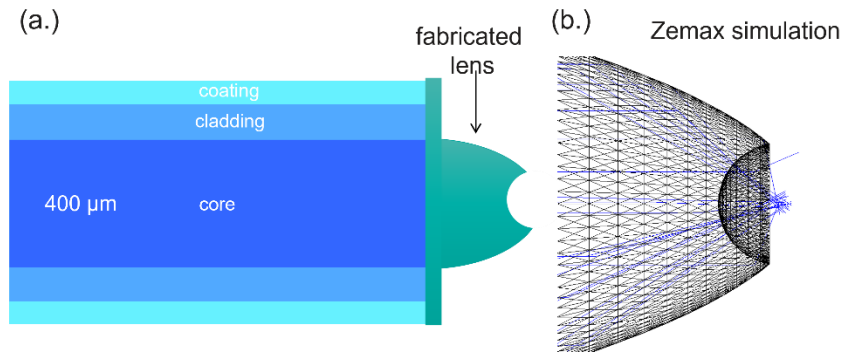
Figure 3.14: (a.) the optical fiber with the fiber tip lens scheme, (b.) focused beam in Zemax simulation - Transmission Matrix Method (linear system characterization) will capture and correct common imperfections such as aberrations

I fabricated this microlens in the Nanoscribe 3D printer using the IP-S Nanoscribe photosensitive resin and the dip-in immersion configuration with the 25x objective lens (NA 0.8). Figure 3.15 shows the CAD model and the fabricated lens with a housing made of the same material to ease the lens attachment on the fiber tip. We tested this lens in the endo-printer set-up with no anti-reflective (AR) coating deposited on the parabolic surface. The experimental spot size is not as small as expected by the NA of the fiber, it is rather similar to the spot size measured with the GRIN fiber. We believe this is caused by the limited set of fiber modes selected by the gating pulse. Based on the work [169], [170], glass high NA lenses can be fabricated on the tip of the fiber and used for endo-printing purposes thanks to higher damage threshold of glass compared to polymers. An anti-reflective coating can eliminate reflections from the surface of the lens. It would be an additional future step to improve the performance of the lens.
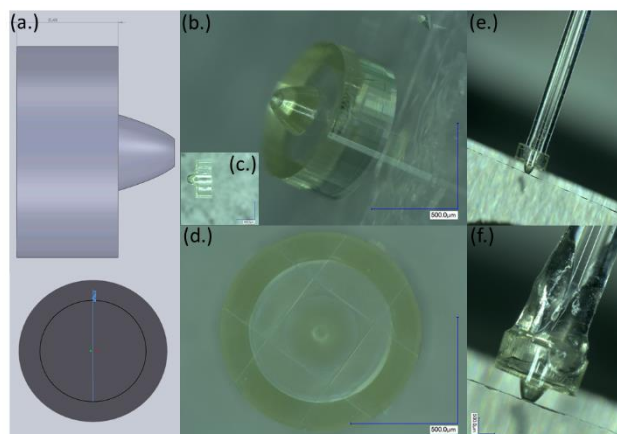
Figure 3.15: (a.) CAD design of the lens (Solidworks), (b-d.) the printed microlens from various views imaged by a digital microscope, (e-f.) Process of attaching the microlens on the fiber tip. All microscopic images scale bars: 500 µm.

3.4   Conclusion

In this chapter, we presented the fabrication of smooth microstructures through a graded-index multimode optical fiber by wavefront shaping, using a transmission matrix calibration and secondly, we demonstrated a factor 5 improvement in fabrication time by PSF-engineering. The tightly focused spots (200 nm hatching distance) are scanned digitally by using a phase-only Spatial Light Modulator. The best results were obtained when the optical beam is blocked for a duration, which corresponds to the rise time of the SLM and stayed open for a period sufficiently long to average the phase flickering of the SLM. The dead time due to flickering can be further reduced with newer SLM with low flicker.

We further improve the surface quality by exposure correction with a fine step of 200 nm. By engineering the PSF to an elliptical focus spot, we showed the fabrication could be decreased by factor corresponding to the larger hatching distance, at the cost of a lower surface quality. We finally present a 3D woodpile fabricated with the fiber printer and the circular PSF. Each hollow square of this woodpile is 4 µm x 4 µm with a smooth surface. With a larger numerical aperture at the tip of the fiber, faster SLMs with low flicker and the flexibility in engineering PSF, we expect similar quality structures and printing times as microscope objectives based two-photon printers.

Chapter 4   Tomographic Volumetric Additive Manufacturing of Silicon Oxycarbide Ceramics

In this chapter, I present my work of the tomographic volumetric additive manufacturing of Silicon oxycarbide Ceramics. A viscous preceramic resin is cured by an ultraviolet source inside a rotating vial. A digital micromirror device projects slices of the object and the 3D-printed green body is shaped. Following this, the polymer to ceramic conversion is achieved in the pyrolysis step and the final ceramic part is obtained.

This chapter corresponds to the manuscript entitled: *"Tomographic Volumetric Additive Manufacturing of Silicon Oxycarbide Ceramics"*, by *Max Kollep, Georgia Konstantinou, Jorge Madrid-Wolff, Antoine Boniface, Pradeep Vallachira Warriam Sasikumar, Gurdial Blugan, Paul Delrot, Damien Loterie and Christophe Moser*, which is published in "Advanced Engineering Materials", Wiley.

I have equally contributed to the design of the experiment, material preparation and manuscript as the other authors. The volumetric printer has been built by previous PhD students. Thus, my work was on the material preparation and processing so that a green body could be printed and a sintered ceramic is obtained with this technology.

4.1   Background

As it was mentioned already in the Introduction, preceramic polymers have been used for the fabrication of polymer derived ceramics (PDCs) since the 1960s. Preceramic polymers are solidified into a rigid green body by stereolithography (SLA) Lithoz GmbH fabricated SiOC ceramic parts by using Digital Light Processing. More precisely, a Digital Micromirror Device is used to project 2D patterns inside a transparent vat with the viscous photocurable ceramic suspension, applied as a thin leveled film by a combination of vat rotation and wiper blade [46].

A similar technology but with a blended formulation of two polysiloxanes was applied by Schmidt et al. They were able to fabricate woodpiles, 2D and 3D grids, cork screws, honeycombs, micro-lattices or Kelvin cell structures, which all maintain their initial shape during pyrolysis at temperatures of 1000 °C [89], [171]. PDCs with micrometer resolution were first demonstrated using two-photon lithography (2PL) by [102] and later more complex structures were also reported with the Nanoscribe 3D printer using higher pyrolysis temperatures [90].

A low-shrinkage preceramic resin ($\sim$ 30 %) was also cured using the Nanoscribe system and resulted in fully dense and crack-free 2PL-PDCs, as reported in the previous chapter. Multiscale ceramic parts were demonstrated by combining DLP and 2PL, for which micrometer resolution was obtained via the latter on the centimeter scale object fabricated by the former [172].

However, overhangs and inner voids are challenging to produce using most AM technologies including vat SLA and DLP. One standard solution is the re-orientation of the printed object compared to the building plate followed by improved control of the exposure dose (e.g., by using a photoabsorber) and another solution is to add supports struts during the printing process.

However, both solutions do not always ensure successful 3D printed structures, especially for 3D models with specific complexity. Moreover, fine and manual post-processing must be performed to remove the support structures, and this limits the freedom of shape [173].

Volumetric 3D printing is a novel light-based technology that eliminates the need for support struts by printing the whole object at once within a vial of resin (see illustration in Figure 4.1.a). The objects fabricated volumetrically are self-supported

within the build volume and are built in a few tens of seconds as opposed to several minutes for DLP or SLA.

 The reason for this decreased building time is that the resin does not have to flow quickly to fill in the surface of the build plate when a new layer is cured. The essence of volumetric 3D printing is to produce a 3D light dose distribution within the volume of the photosensitive material using tomographic back-projections [78], [79], [174] or orthogonal dual-wavelength photopolymerization [175].

Figure 4.1: a. In tomographic volumetric additive manufacturing of silicon oxycarbide ceramics, the 3D model of the desired part is used to calculate a set of light patterns which are projected onto a rotating vial filled with a photo-curable preceramic resin. The resulting solid green body is retrieved from the liquid resin, and pyrolized at T = 1000 °C. b. Schematic representation at the molecular level. A polysiloxane preceramic resin is mixed with a crosslinker and a photoinitiator. After excitation with blue light, a stiff network of polymerized and crosslinked polysiloxane chains forms the green body. A 48h pyrolysis cycle burns out most of the organic components and transforms the part into a silicon oxycarbide ceramic amorphous network [96].

As a 3D printing technology, it is not only faster but also produces isotropic homogeneous polymerized bodies because the whole object is polymerized at once rather than layer-by-layer [174]. Moreover, it allows the fabrication of hollow structures and geometries with large overhangs, which are unprintable with other AM technologies. Recent progress in volumetric additive manufacturing now allow printing different materials including acrylic [79], thiol-ene photoresins [176] or even scattering resins [80], but the 3D printing of ceramics with a tomographic approach has never been reported to our knowledge.

4.2   Methods

4.2.1   Preceramic resin

The preceramic resin that is being used in this work, was prepared by combining a commercially available polysiloxane substituted precursor (SPR 684, Starfire Systems, USA) with 1,4-butanediol diacrylate (BDDA) as a crosslinker (1070-70-8, Sigma Aldrich, USA), and Diphenyl (2,4,6-trimethylbenzoyl) phosphine oxide (TPO) as a photoinitiator (75980-60-8, Sigma Aldrich). The role of the crosslinker BDDA is to speed up the crosslinking process as polysiloxane alone is very slow to respond to photocrosslinking.

The resin preparation consisted of 85 wt% polysiloxane, 15 wt% BDDA and 2mM TPO (0.063 wt%). As a first step, for the production of the resin, a solution of diluted TPO in BDDA is prepared to a concentration of 30 mg/mL, which is then vortexed. Directly after, the polysiloxane precursor is combined with the TPO in the BBDA solution. The components are then simultaneously mixed and degassed using a planetary mixer (Mazerustar KK-250SE, Kurabo, Japan). Finally, the resin is poured into glass vials of 16.5 mm, which are used for printing.

4.2.2   Tomographic volumetric additive manufacturing

A custom volumetric 3D printer [79], built by former PhD students in our group, is used for this work. In the 3D printing setup, the light from 4 laser diodes ($\lambda = 405$ nm)

is coupled into a multimode fiber. Then, the beam is expanded to fill a Digital Micromirror Device, DMD, (VIS-7000, Vialux, Germany).

The patterns for the tomographic reconstruction of the part are displayed on the Digital Micromirror Device (DMD) and projected by a pair of achromatic lenses 9 with focal lengths of f1 = 100 mm (AC254-100-A-ML, Thorlabs, USA) and f2 = 250 mm (ACT508- 250-A-ML, Thorlabs) onto the rotating cylindrical glass vial containing the photopolymer.

The resin vial is dipped in a refractive index matching bath with square footprint to remove the lensing effects of the round vial. A camera is recording the progress of the print in the vial by imaging the sample with an orthogonal 671 nm expanded laser beam.

The patterns for the tomographic backprojection are computed following the algorithm described in Chapter 1. The STL file of the 3D part is voxelized using a python script. Following this, the Radon transform of this digital object is calculated over π rad around one of its axes. The Fourier transform of these patterns is taken and a ramp filter is applied to compensate for the over sampling of the low spatial frequencies.

As a final step, the inverse Fourier transform of these patterns is calculated. Additional corrections for attenuation from the photoinitiator were also performed following [80]. The viscosity of the resin is a key physical parameter in tomographic printing. If the viscosity is too low, the object sediments.

It is therefore important to ensure that the printing is fast enough so that sedimentation does not affect the resolution of the final object. The viscosity of the resin used in this work (873 mPa.s) is lower than those used in previous works (10 Pa.s [79] and 5 Pa.s [78]).

We did not observe any impact on the resolution of our prints. This viscosity is sufficient to prevent sedimentation that is deleterious to print resolution. The data presented in Figure 4.2 show the slow sedimentation of the printed piece over time, less than 200 µm in a minute.
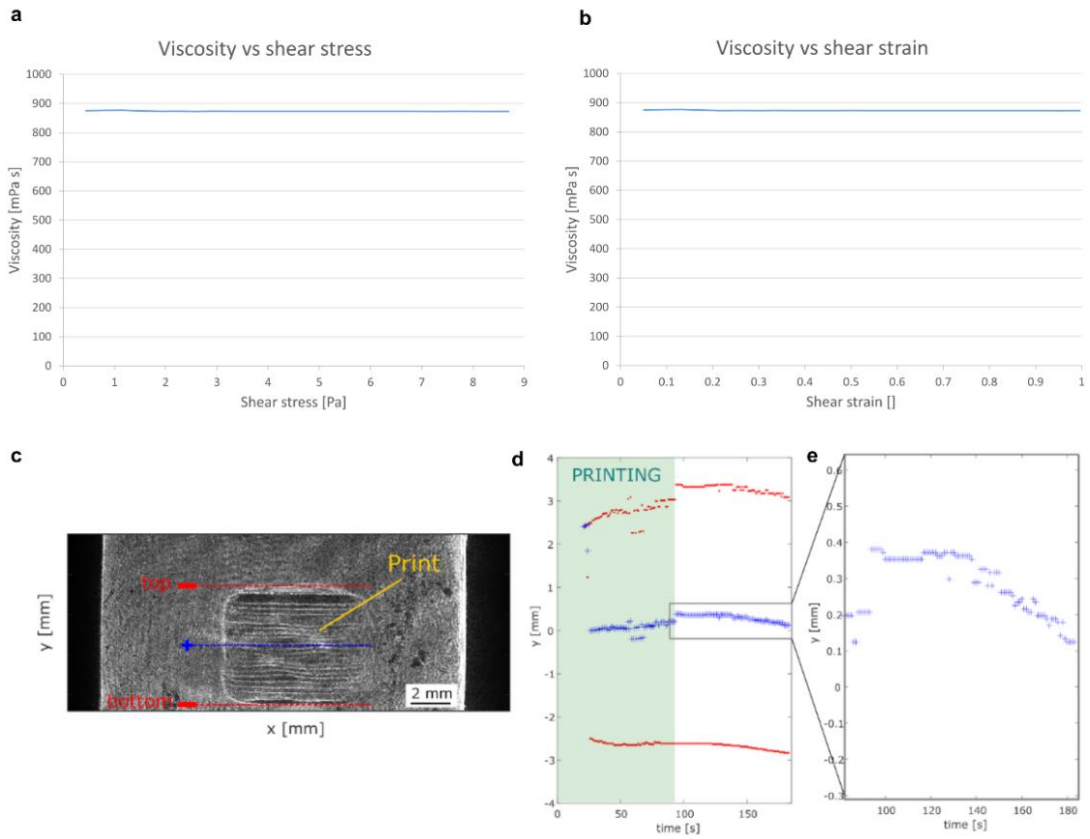
Figure 4.2: Viscosity and sedimentation of parts during printing. a. Viscosity vs. shear stress. b. Viscosity vs. shear strain. c. Typical side view camera image. Due to the solidification of the resin, the polymerized part has a slightly different density, hence refractive index. This translates into some contrast on the transmitted laser beam. d. From this image, we can evaluate the bottom and top part of the print (indicated in red) and track all together with the center of the print, their positions over time. e. A zoom in the graph d. shows the slow sedimentation of the piece over time.

4.2.3 Postprocessing of prints

When the printing is over, the parts are recovered from the glass vials and dipped into a toluene bath, which is manually stirred for 5 minutes until all uncured resin dissolves. After that, the parts are placed in a bath of isopropyl alcohol (IPA) to dilute the toluene and stop the solving action on their surface. The bath is manually stirred again for about 1 minute. The parts are then left at room temperature until IPA gets fully evaporated.

In the next post-processing step, the parts are postcured in a UV curing station (FormCure, Formlabs, USA) for 1 hour at room temperature. After this, all remaining photoinitiator molecules have been consumed, but the surface is still sticky. To remove the stickiness, the green bodies are submerged in a concentrated solution of TPO in IPA (10 mg/mL) and left for 1 hour to allow TPO to diffuse inside. The bath with the parts is then placed for 15 minutes in the UV curing station. The parts are removed from the bath and postcured one last time for 45 minutes in the curing station. After that, the green bodies are placed in an oven for 24 hours at 80 °C to remove most of the solvent soaked into the part.

4.2.4 Pyrolysis

The rinsed, postcured, and aged green bodies are pyrolysed in an alumina tube furnace (STF 15/450, Carbolite Gero, Germany) under argon atmosphere following the temperature profile in Figure 4.3.

The pyrolysis peak temperature was set to T = 1000 °C, for a dwell time of 1 hour, and a total cycle duration of 48 hours.
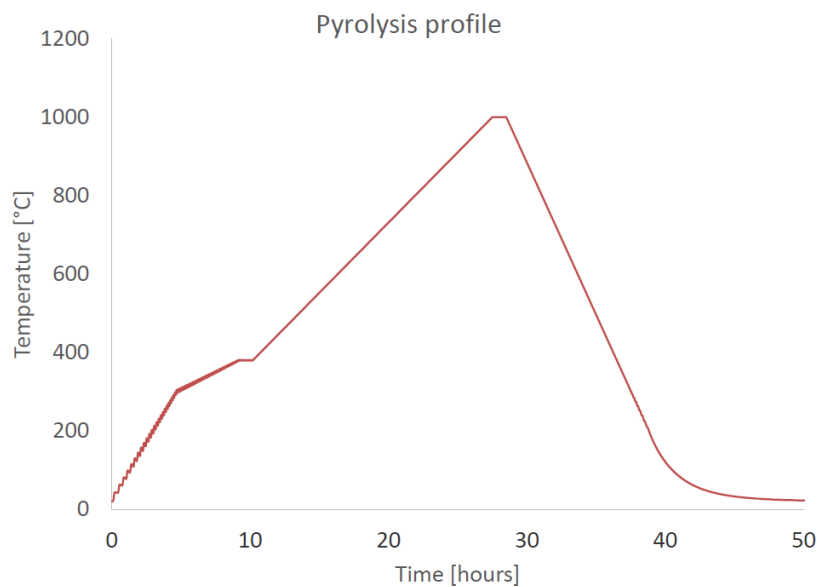
Figure 4.3: Measured pyrolysis temperature profile.

The main dwell time is at T = 1000 °C, which is the temperature at which the preceramic polymer loses all its organic components and converts to silicon oxycarbide. The crosslinker has to be decomposed and evacuated. This is mainly done at the other dwell time at T = 380 °C for one hour. Since the crosslinker is completely decomposed, this resin composition has a lot of matter to be outgassed. This makes the pyrolysis challenging and very prone to cracks and swelling.

In order to hinder these negative effects, the heating and cooling rates are very slow to provide more time for the gases to escape. In this way, the pyrolysis process is gentler and allows for a better success rate. The first heating ramp is done at 1K/min because no component gets decomposed under 300 °C. The second ramp is done at 0.3K/min. At this step, we are approaching the crosslinker decomposing temperature of 380 °C and this has to be completed gently. After the first dwell time of 1 hour, most of the crosslinker is evacuated and so the heating ramp can be brought up to 0.6K/min. After the second dwell time, the parts have been converted to ceramics, so the cooling step can be faster. The cooling rate is 1.3K/min.

After around 40 hours, the cooling is not fast enough anymore to follow the desired rate. Since the furnace does not have active cooling, the temperature decays exponentially. The decomposing temperature of the crosslinker was determined by thermogravimetric analysis, which is provided at the end of the chapter.

4.3   Results

4.3.1   Preceramic resin and polymerization

The formulation of the preceramic resin, being used in these 3D printing experiments, is highly transparent in the visible range, with most of its absorbance coming from TPO. In Figure 4.4, the absorbance measurements of the resin are presented, with and without the photoinitiator. The non-linear dose response of the resin is also provided along. The attenuation profile of the resin over the width of the vial is given when the concentration of the TPO photoinitiator is properly selected.
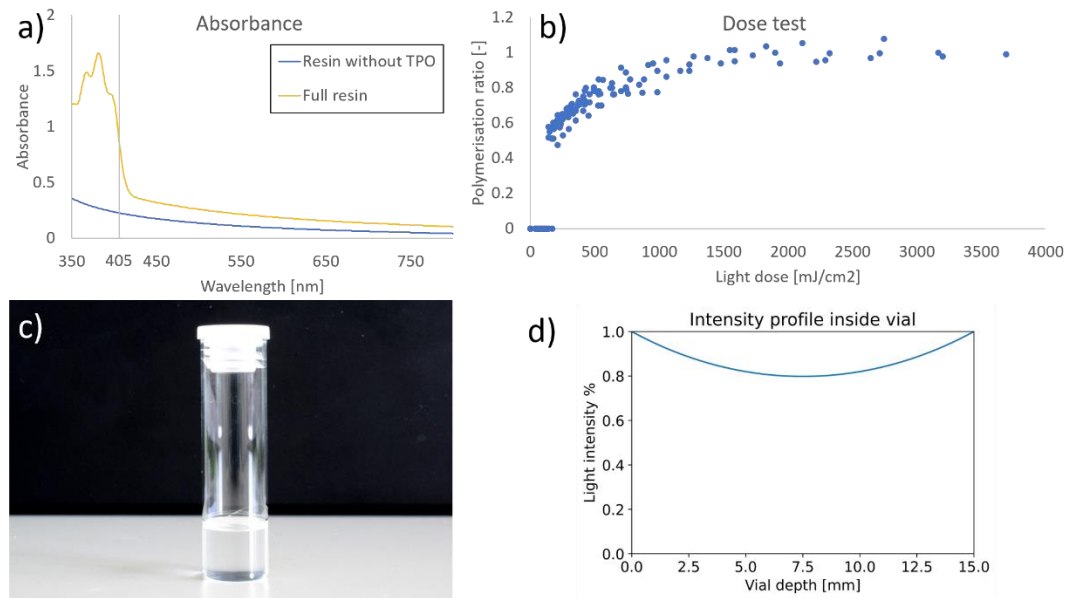
Figure 4.4: Preceramic resin characterisation a) Absorbance measurements of the resin with and without the photoinitiator, (measured in 10 mm wide vials). b) Non-linear response of the resin to the light dose. c) Picture of a 16,5 mm print vial with transparent resin. d) Attenuation profile of the resin over the width of the vial.

This means that the absorbance of the preceramic resin with the TPO should allow the light to penetrate to the center of the vial. If this is not the case, the resin is immediately polymerized on the walls of the vials, inhibiting sufficient fabrication of the desired object. The acrylate-mediated photo-polymerization exhibits a thresholded nonlinear response to light dose, which is fundamental in tomographic volumetric additive manufacturing. Light attenuation can hinder the printability of cm-scale shapes. For this reason, we correct for the optical attenuation following the method described in [80].

The dose threshold is quantified by performing a dose test. The test consists in projecting round dots onto a 1 mm thin vial filled with the resin. The dots have all a diameter of 500 µm and vary in intensity along one axis and in exposure time along the other axis. This array of dots tests simultaneously different doses and this affects the size of the actually printed round dots. The polymerization ratio is determined as the size of the printed dot divided by the size of the projected dot. Some dots were not polymerized at all and some are larger than the projection. This allows determining the dose threshold of the resin.

The radical polymerization mechanism illustrated in Figure 4.1.b begins with single-photon absorption by the photoinitiator (TPO). This generates the primary radicals

(C-centered acyl and P-centered phosphinoyl radicals) after the α-cleavage of the C-P bond [177], [178]. The efficiency of the crosslinking at the propagation step is enhanced thanks to BDDA. More precisely, the primary radicals of the initiation step (TPO) activate the radical polymerization of the BDDA by cleaving the methylene bond. The high reactivity of BDDA assists the chain growth of the PCP by a similar mechanism of methylene cleavage. In this way, the crosslinking propagates to a direction perpendicular to the chain of the PCP. The termination step is ensured when the irradiation stops. After the pyrolysis step, amorphous SiOC is formed and the corresponding bonds are confirmed by X-ray photoelectron spectroscopy [179], [180]. In the volumetric printer, parts are printed within rotating glass vials filled with the photo-curable resin as a set of light patterns are exposed onto it. The used resin has a viscosity of 873 mPas, which is high enough to prevent sinking of the polymerized part within the printing times of 30 to 60 seconds.

The resin shows a nonlinear response to the light dose [181]. Two effects cause this: the gelation threshold of the resin [182] and the presence of an inhibitor in the resin. The inhibitor reacts with the excited photoinitiator, preventing the initiation of the polymerization process. This inhibitor shifts the polymerization to higher light doses since it must be locally depleted for the polymerization to start. In this case, the inhibition is caused by the oxygen naturally dissolved from the atmosphere in the resin. This nonlinear response is crucial for the volumetric printing process because it creates a threshold of light dose that must be surpassed to start the polymerization. Thanks to it, the light projected from the DMD can penetrate the resin without polymerizing it directly at the edges of the vial. Only in the center of the vial where the light dose is cumulated in shorter arcs from multiple exposures at different angles, does it surpass the threshold and polymerizes the resin.

4.3.2   Geometrical characterization of 3D printed ceramic parts

At first, to illustrate the volumetric method, we fabricated polymer-derived ceramic woodpiles measuring 5 mm × 5 mm × 5 mm with 5 layers of rods of square cross section measuring 1 mm × 1 mm and spaced out by voids of the same dimensions, as shown in Figure 4.5.a and b. Micro-CT scans (10 μm resolution) and the SEM image (5nm resolution) of the internal side of a cleaved pyrolysed part show that they are fully dense with no signs of porosity throughout the bulk of the PDC.

Furthermore, the parts retain the design voids inside, even after pyrolysis. Figure 4.5.c shows a series of scanning electron microscopy images (5nm resolution) of the woodpile structure, highlighting the surface quality of the prints. The fabricated ceramics are smooth, as it had been also observed in the two-photon case for the same preceramic resin. It can be observed that the vertical walls of the PDC exhibit some striations when compared to the horizontal ones. These striations are typical of volumetric additive manufacturing and might come from self-writing waveguide effects [183]. We observe that the surface smoothness is higher compared to ceramic structures occurring from Digital Light Processing [184], [185]. Additionally, volumetric additive manufacturing simplifies post-processing of the green bodies due to the absence of a build plate or support structures.
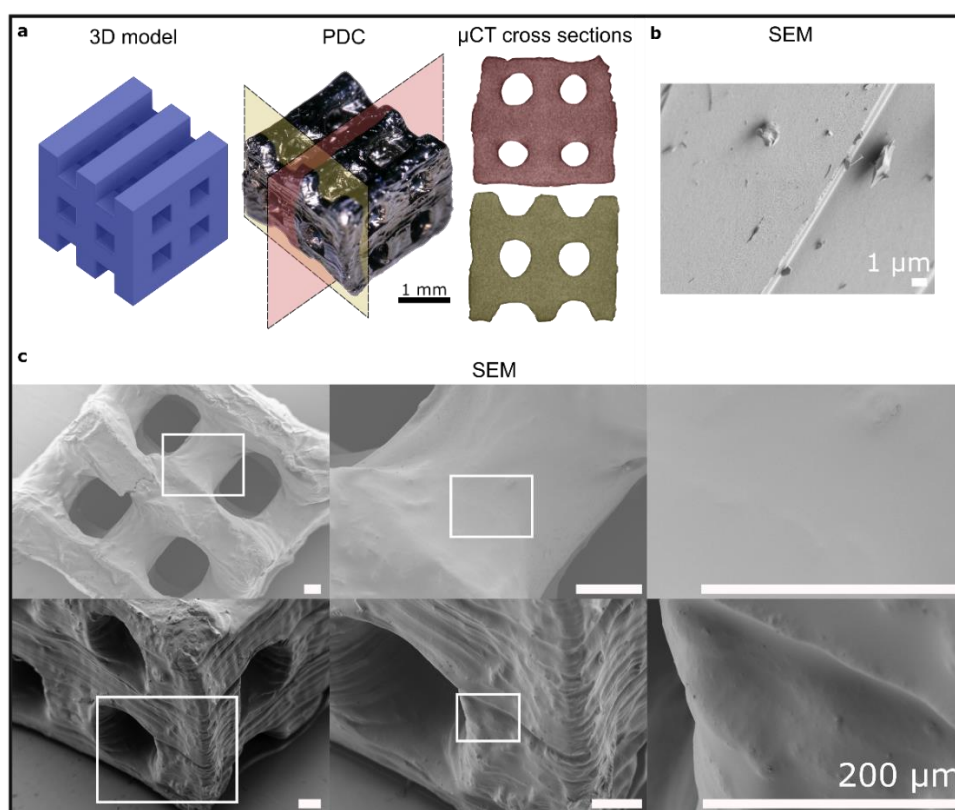
Figure 4.5: Density and smoothness. a. 3D model, microscope image and cross sections from micro–Computed Tomography images of a 5-level woodpile. Scalebar 1 mm. b. SEM image of the internal side of a cleaved ceramic part. Scalebar 1 µm c. SEM images of the printed parts and their surfaces. Scalebars 200 µm.

The pyrolysis step leads to the decomposition of organic units with an escape of volatile gases. Polymer to ceramic conversion usually happens within a temperature window of 400-800 °C. Above 600 °C, there will be rearrangement of bonds to form Si-C rich and Si-O rich regimes. The ceramic formation is completed at 1000 °C.

However, a large mass loss is observed at ~ 600 °C based on the Thermogravimetric Analysis presented in the end of the chapter (Figure 4.11) and this leads to shrinkage between the green body and the polymer derived ceramic.
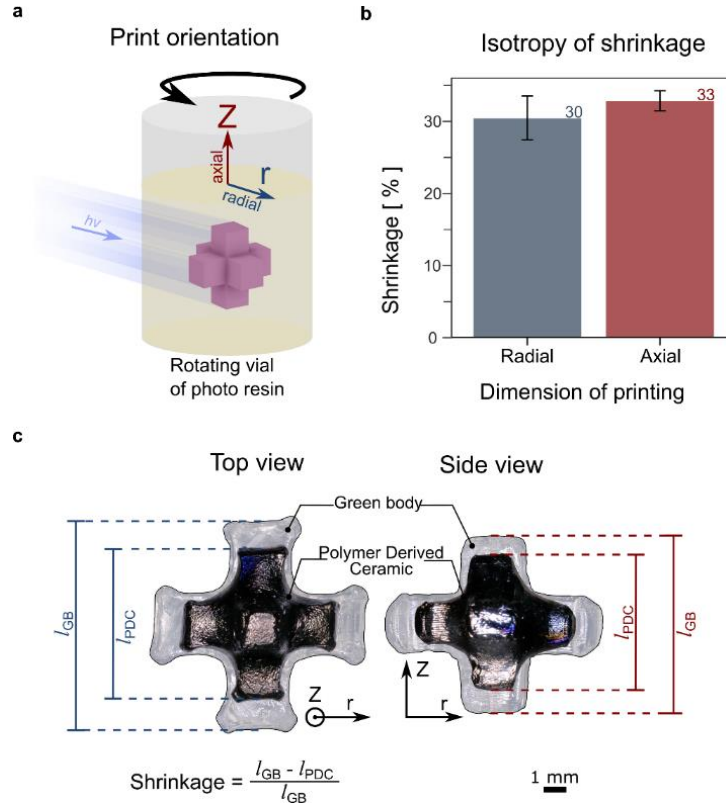
Figure 4.6: Isotropy of shrinkage. a. In tomographic volumetric additive manufacturing, the object is printed upon the simultaneous polymerization of the resin in the rotating vial. Unlike SLA or DLP, the part exhibits isotropic polymerization along cylindrical coordinates. b. Shrinkage along the axial and radial dimensions of prints. An unpaired t-Test shows that there is no significant difference between the shrinkage along the radial and axial dimensions. Error bars indicate a standard deviation. c. Overlay of the green body and polymer derived ceramic of a 3D cross.

Shrinkage poses a difficulty to fabricate functional pieces from preceramic polymers [186]. Recent works measured the resulting shrinkage after pyrolysis and applied corrections to the 3D model to obtain accurate parts [187]. Such corrections are more straightforward if the shrinkage is isotropic. Previous works on volumetric additive manufacturing have shown that tomographic back-projection results in isotropic, smooth polymerization, contrary to extrusion-based printing and DLP [174]. Since the green bodies are formed volumetrically, without a preferential direction, it is expected that the shrinkage is isotropic. Indeed, the pyrolyzed parts did not show significant differences in shrinkage along any direction ($p = 6.3 \times 10^{-6}$).

This allows the PDCs to keep their shape along the axial and radial dimensions of printing, as shown in Figure 4.6. Additionally, we report a shrinkage of 31.0 ± 1.7% and a mass loss of 54.0 ± 0.2% from printing to pyrolysis. These results are in line with those of previous works [186], [188].

4.3.3 Ceramization of the polysiloxane substituted precursor

The SPR-684 is a commercially available polysiloxane which converts to ceramic for pyrolysis temperatures tested already in the range of 1000-1400 ∘C [97], [120], [189]. Both green and ceramic parts were examined by Fourier Transform Infrared Spectroscopy, Raman Spectroscopy and X-ray photoelectron spectroscopy (XPS). In Figure 4.7, the FTIR, Raman and XPS (Si2p) spectra of preceramic and pyrolysed parts are presented.
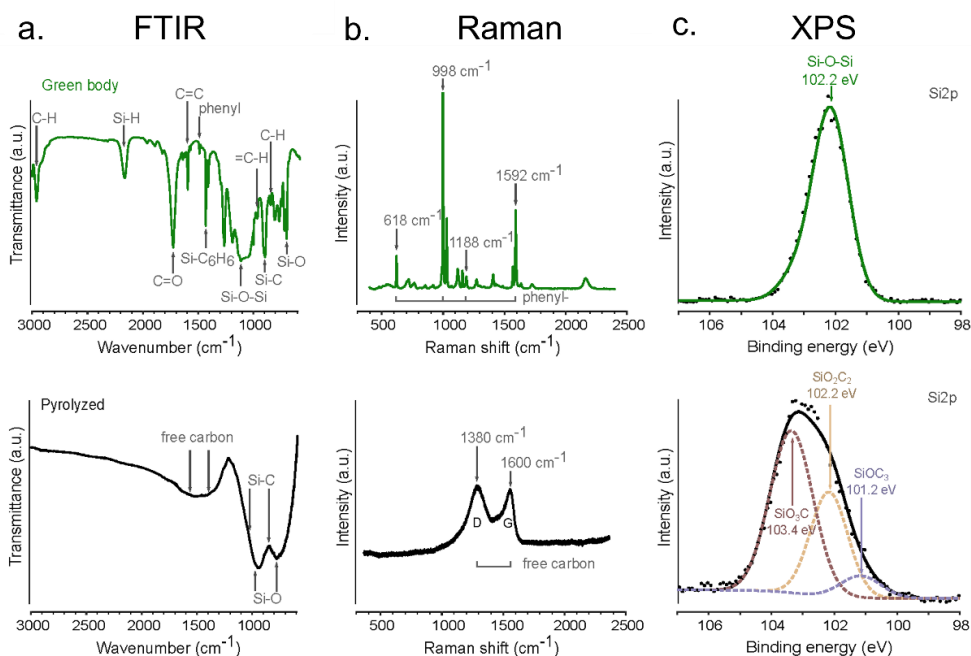
Figure 4.7: a. FTIR spectra b. Raman spectra and c. XPS spectra of the green body and the polymer derived ceramic [180].

In Figure 4.7.a, the FTIR spectra of the green and pyrolyzed state are presented. In the spectrum of the green body, several bands are observed which are mostly

referred to the organic siloxane backbone and its functional groups. In the pyrolysed state, the bands appear as a smoother curve presenting mainly Si-O and Si-C type bonds after ceramization. Both spectra are in good agreement with prior work of the exact same preceramic polymer in the green state, including the added crosslinker and photoinitiator [120], [190]–[198], and in the pyrolyzed state [120], [191], [199].

As seen in Figure 4.7.b, Raman spectroscopy of green bodies and pyrolyzed parts suggests a conversion from an organic to an inorganic material after pyrolysis. The spectrum of the green body shows numerous narrow bands, characteristic of the organic siloxane backbone and crosslinker. Most notably, peaks at 618, 998, 1188, and 1592 cm−1 are likely those of the phenyl group in the backbone [200], [201]. The Raman spectrum of the pyrolyzed parts mainly exhibits two broad bands at 1380 and 1600 cm^{-1}, namely the D and G bands of free carbon [202]. So-called free carbon intrusions have been previously documented in pyrolyzed polymer-derived ceramics [203]–[205]. The organization of this free carbon phase segregated within the microstructure and the gradual degradation of the amorphous Si–O–C network have been linked to higher pyrolysis temperatures. This free carbon, as illustrated in Figure 4.7.b, has been suggested to explain the high thermal resistance of these materials [39].

XPS spectra around the Si2p show a broadening of the peak for the pyrolyzed parts, with respect to the green bodies, as seen in Figure 4.7.c. The spectrum for the pyrolyzed part spans the binding energies that are characteristic to intermediate mixed silicon oxycarbide species, namely SiO_3C, SiO_2C_2, and $SiOC_3$ with binding energies at 103, 102, and 101 eV respectively [206]. Bonds of lower energies, such as SiC [207], might be present in these samples, although at much lower concentrations as the appearance of nanocrystalline SiC has been documented in PDCs only at higher pyrolysis temperatures (>1300 ∘C) [199]. Recent studies have shown that the site of binding between phenyl groups and the silicone backbone may result in mixed Si-O and Si-C bonding, particularly at the interface between the silica rich nanodomains and the free carbon nanodomains [208]. In contrast, the XPS spectrum of the Si2p bond for the green body shows a narrower peak, with an energy distribution that matches that of siloxanes with organic functional groups [209].

4.3.4 Resistance of 3D printed ceramic parts

We tested the physical and chemical properties of the fabricated PDCs. To test their thermal resistance, we exposed the parts to rapid thermal shock cycles of 15 seconds heating up under the flame of a butane torch and 10 seconds of cooling down. The temperature of the flame (T ≈1400 ∘C) is higher than the pyrolysis temperature.

Figure 4.8.a shows a time-lapse sequence of a spherical woodpile under its fifth thermal stress cycle. The first and last frames of the time-lapse show that the part retained its shape and did not crack, even withstanding the stress induced by the holding clamp. To assess the chemical inertness of the parts, we submerged them for 1 hour in aqueous corrosive baths.

Figure 4.8.b shows a 3D cross PDC sitting in a HCl solution of pH = 2 on the left and a 3D cross PDC sitting in a KOH solution of pH = 14 on the right. Both parts retained their mass (within 0.1 mg on a precision scale). This demonstrates and confirms that they are very resistant to high temperatures, rapid heating and cooling for several cycles, and to corrosion, as expected for all SiOC materials.
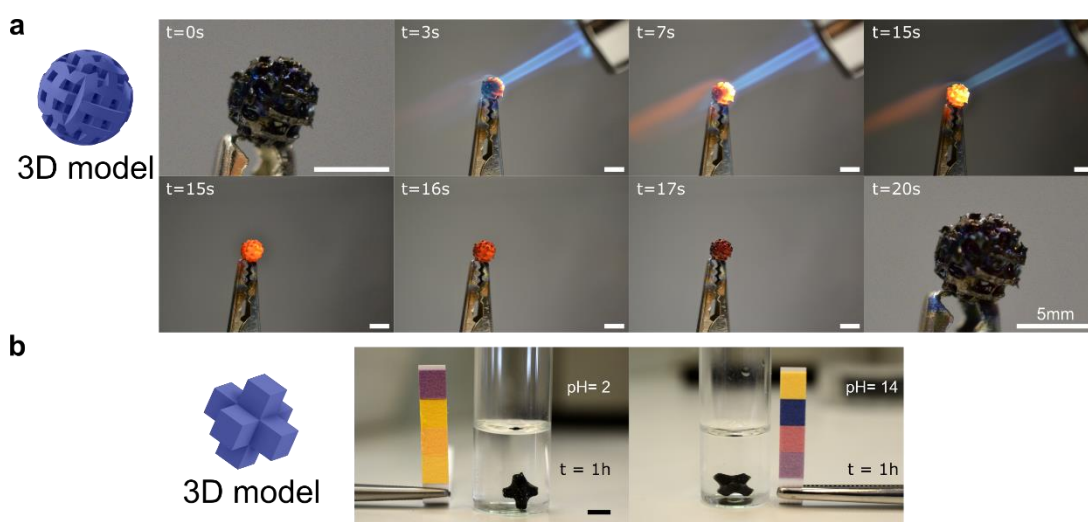
Figure 4.8: Resistance of 3D printed ceramic parts. a. Timelapse of a ceramic part being heated to incandescence with a buthane torch (T= 1400 °C) and then let cool down. The last frame shows the part after five cycles of thermal stress. Scalebars: 5 mm. b. Parts after being immersed for one hour in a strong acid (pH = 2) or a strong base (pH = 14) for 1 hour. Scalebars: 2 mm.

4.3.5 Examples of 3D volumetric printed ceramic parts

Volumetric additive manufacturing enables the fabrication of microcomponents with unique geometries, which are more challenging to obtain with other AM technologies. This is illustrated in Figure 4.9. The top row depicts a 10-level spherical woodpile structure with rods of 1mm in width and height spaced by 1mm, cropped in the shape of a ball. This type of structure would be more challenging to fabricate and de-attach from the building plate of a DLP printer without damage. After pyrolysis, the 31% shrinkage brings the size of the ball down to ≈ 6 mm diameter with features of 700 µm. The shape was successfully pyrolyzed without bubble formation, deformation, or cracks. This shows that relatively large objects can be produced, as long as escape routes are added for the gases in the form of empty channels. The second row presents a screw with 3 full revolutions, 7.2 mm in length, an outer diameter of 6 mm, and with a channel of diameter 1 mm going down its center.
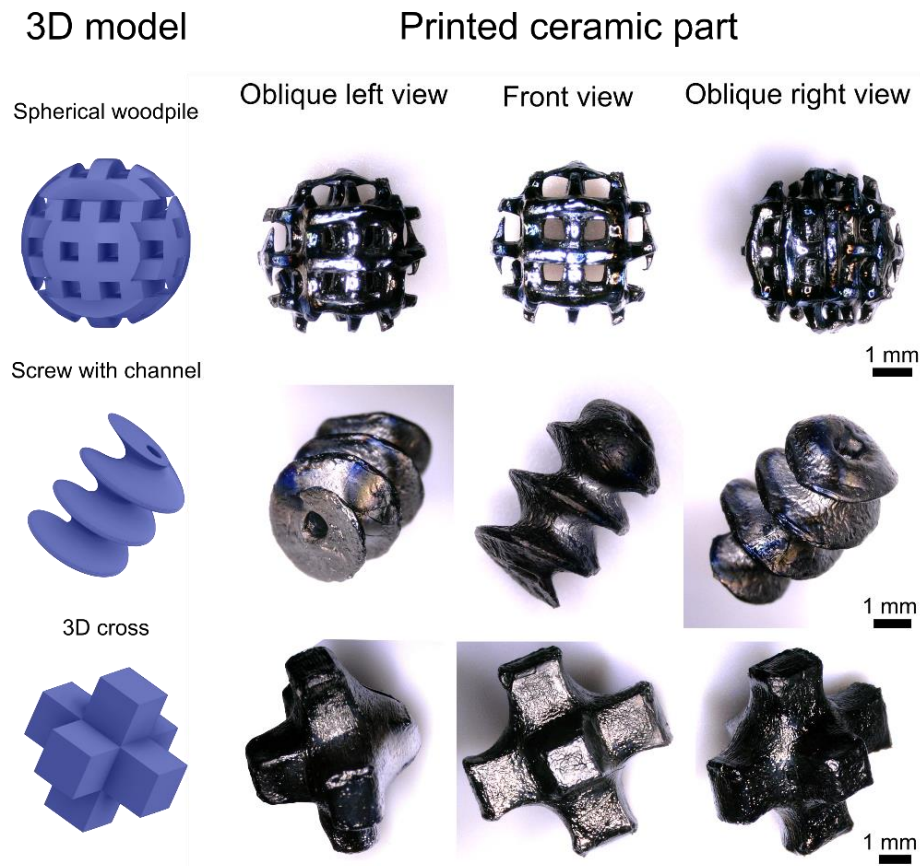
Figure 4.9: Examples of 3D volumetric printed ceramic parts. Top one is a spherical woodpile. Middle one is a screw with a channel. Bottom one is a 3D cross. Scalebar: 1 mm.

After pyrolysis, the channel diameter was reduced to 700 μm and length of the screw reduced to around 5.75 mm. Some air bubbles were trapped within the PDCs during pyrolysis, thus slightly deforming the part. This shape shows that it is possible to have features on the outside of the part while having a void channel in the center. The third shape is a 3D cross with arms of dimensions 3 mm × 3 mm × 3 mm. After pyrolysis, those dimensions got reduced to 2mm × 2mm × 2mm. Again, this shape deformed because of a bubble in its center. The bubble is slightly off center, which gives it this asymmetrical deformation, with one side unaffected and the other with a swollen arm, as it can be observed in the column with the title "oblique left view". Additionally, the 3D cross, presented in Figure 4.9 and in Figure 4.6.c as a green and pyrolysed part, shows curvy details near its center compared to the 3D model. Similarly, the same effect is observed in the woodpile presented in Figure 4.5. This is related to the volumetric 3D printer itself. More specifically, some high frequencies are missing in the calculation of the Radon Transform, resulting a less accurate set of tomographic projections.
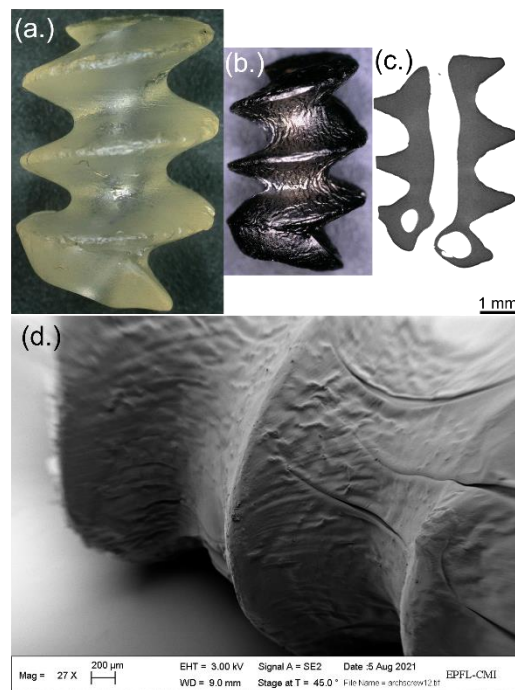
Figure 4.10: (a.) Green part of the screw, (b.) Ceramic screw, (c.) Micro computed tomography slice of a screw with a channel (in the pyrolysed state), (d.) SEM image of the screw (in the pyrolysed state).

The second object presented in the second row of Figure 4.9 was imaged by X-ray micro-tomography (in the pyrolysed state) and Scanning Electron Microscopy (in the pyrolysed state) as well and is presented in Figure 4.10.

4.3.6   Results analysis

<u>μCT Imaging</u>

Printed objects were imaged with voxel sizes of 10 μm × 10 μm × 10 μm under a 160 kV X-ray transmission tomograph (Hamamatsu, Japan). 3D visualizations of the pieces were obtained using Fiji-ImageJ [210].

<u>Photographic Imaging</u>

Green bodies and pyrolyzed parts were imaged with a DSLR camera (D3100, Nikon, Japan) with a f =2.8 macro lens (AF-S Micro Nikkor 40 mm, Nikon), and a digital microscope (VHX-5000. Keyence, USA).

<u>Gold deposition and SEM</u>

The sputtering machine Alliance-Concept DP650 was used for the deposition of a thin gold layer (20nm) on the samples. Following that, the samples were transferred to the Scanning Electron Microscope (SEM LEO 1550) and were inserted into the chamber vacuum for imaging the surface from low to high magnification.

<u>Thermal stress resistance</u>

To show resistance of the ceramic parts to high temperature, a butane torch was heating the ceramic parts (T ≈ 1400 °C) for some seconds until they became incandescent and then let cool down. A typical thermal stress cycle was 20 seconds. The spherical woodpile shown in **Error! Reference source not found.** was subjected to 5 thermal stress cycles.

<u>Chemical resistance</u>

Parts were dipped into vials containing aqueous solutions of HCl and KOH solutions (pH = 2, and pH = 14 respectively) for one hour and photographed at the beginning and the end of the experiment.

<u>Shrinkage</u>

To compare the differences between shrinkage along the axial and radial dimensions of the prints, a set of lengths were measured on green bodies and their corresponding PDCs (nparts = 7, nmeasurements = 14), most of them woodpiles.

Statistical analysis

Statistical analysis of the isotropy of shrinkage was conducted by running a two-tailed t-Test assuming unequal variances (Welch test, α = 0.05) on Microsoft Excel.

Thermogravimetric analysis

The samples were heated with a heating rate of 5 degrees/minute to maximum temperature under controlled argon atmosphere. During the measurement, the mass loss percentage and the Differential scanning Calorimetry are obtained and presented in Figure 4.11. In the calculated Derivative thermogravimetry profile (DTG- blue line) two major decomposition intervals are observed with the appearance of two peaks, first one starting at 375 °C and the second one above 470 °C. The second one is common for PDCs and it appears to be completed above 600 °C. The first mass loss is mainly due to the decomposition of BDDA, which starts above 370 °C. This explains the dwelling step applied at that temperature (to allow smooth release of all the volatile gases) in the pyrolysis profile. Moreover, this step contributes to significantly reduce the formation of bubbles. In the same way, in DSC (gold line) we can observe a small peak around this temperature, which is attributed to this process. The mass loss is completed at ~ 600 °C and there are no more mass losses as seen from the TG curve (mass loss %).
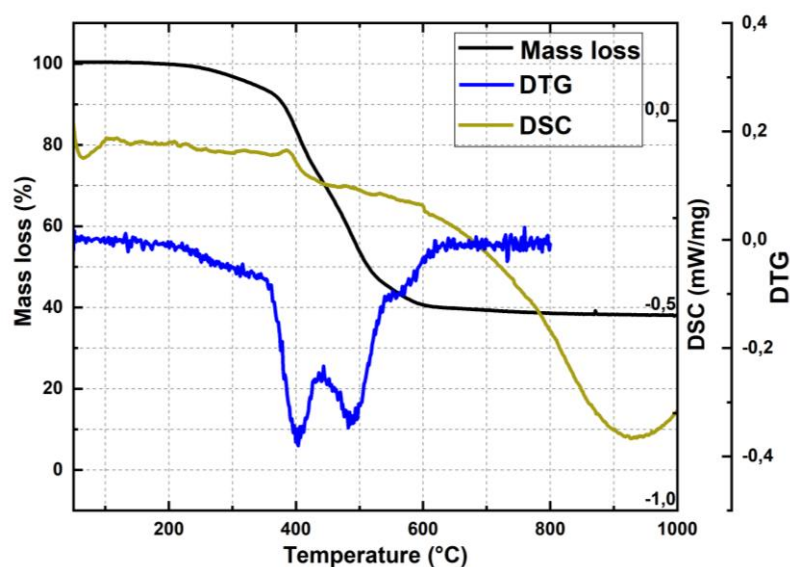
Figure 4.11: Mass loss in percentage (black line), Derivative thermogravimetry (DTG- blue line) and Differential Scanning Calorimetry (DSC- gold line) profiles.

4.4   Conclusion

In this chapter, we demonstrated the fabrication of isotropic, fully dense and crack-free PDCs with volumetric additive manufacturing. We formulated a transparent and highly viscous preceramic resin which is added in a rotating, transparent cylindrical vial photocured with a laser source at 405 nm and using tomographic back-projection. Parts with complex shapes were successfully fabricated and the green bodies were converted to ceramic parts through a pyrolysis step. We reported qualitatively on the density and the smoothness of the parts at the microscopic scale by micro-Computed Tomography and Scanning Electron Microscopy. Based on these experimental measurements, we estimated the isotropy of shrinkage and the mass loss. Lastly, we validated the polymer to ceramic conversion by X-ray photoelectron spectroscopy and confirmed the high resistance to heat and acidic or basic environments.

Ceramics are popular candidates for the fabrication of prototypes with exceptional properties, but traditional AM techniques impose long building time because of their inherent layer-by-layer process. Consequently, both steps of the 3D printing and the pyrolysis are time consuming, which stands in the way of rapidly optimizing a ceramic prototype until specific requirements are met (accuracy, precision and tolerance). Volumetric printing is an emerging 3D printing technology that drastically accelerates the 3D printing step, leads to isotropic shrinkage properties, and opens up a different range of materials and geometries for use in prototyping ceramics. Future work on the accuracy assessment step could provide even faster cycles to optimize prototypes.

Chapter 5   Conclusion

This thesis is largely experimental in nature and presents methods and processes to print micro-scale ceramics with submicrometer resolution using two-photon printing and macro-scale ceramics with approximately 100 μm resolution using a volumetric tomographic printing method. Additionally, I presented major improvements of two-photon printing using a multimode fiber.

Summary of the results and future work

In the first part of the thesis, pre- and post-processing protocols were investigated and applied for the fabrication of ceramic microstructures by two-photon polymerization. A preceramic resin in combination with a photoinitiator was used to fabricate microstructures with maximum size 130 μm x 100 μm x 80 μm. The printing parameters of dose (fabrication speed and peak intensity), hatching and slicing were tested in the printing and the pyrolysis step to obtain the final ceramic part without any deformation, pores, or cracks. By applying X-ray micro-tomography, we validated the success of the process, and a few examples of complex 3D objects were presented.

In the second part of the thesis, a fiber endo-printing tool was built and used for the polymerization of microstructures by two-photon polymerization. This tool had been already used for 3D printing purposes either by single or two-photon polymerization but with low printing fidelity [29], [30]. By applying wavefront shaping, exposure dose correction and by controlling a spatial light modulator properly, I showed a major improvement of the surface quality of 3D printed parts through an optical fiber. In addition, by applying wavefront shaping, larger spots are focused through the optical fiber and in this way faster fabrication of the same surface was achieved.

Finally, a volumetric tomographic 3D printer was used to investigate the printing parameters and fabricate mm- and cm- scale objects by single-photon polymerization of a preceramic resin. It was required to redefine the printing parameters and the pyrolysis step because of the printing technology that was used. Thanks to the viscosity of this resin and the proper photoinitiator used, large-scale ceramic objects were fabricated and pyrolysed. X-ray tomography and Scanning Electron Microscopy were used to evaluate the fidelity of the prints, the low porosity and the crack-free objects. Moreover, performance tests were conducted in acidic and basic environments and in high temperatures (1400 °C).

Ceramics are materials with exceptional properties, hence improving the printing fidelity and performance of ceramic objects will continue attract the attention to the scientific and industrial community.

Combining ceramics and electrically conductive ceramics by AM would enable the fabrication of functional devices such as high voltage sensors and electrodes. Adding electrical conductivity to ceramics in light-based AM is a challenging task because the conductive fillers, such as titanium, make the resins highly scattering. Two-photon dip-in polymerization of conductive pre-ceramic polymers could still be possible due to the infrared wavelength used which is less scattered than the blue light in single photon systems.

Ceramic micro- and macro- parts with complex shapes such as micro-propellers could be used in mini satellites in the harsh environments in Space. Similarly, oceanographic equipment or seismographic equipment could be replaced by smaller, high-performance devices (i.e ceramic sensors, actuators).

A fiber endo-printer which fabricates microstructures can be very interesting for in in-situ tissue engineering. The idea is that the scaffolds are printed in-situ and the body itself is the incubator for the cells. Fast endo-printing by two-photon could be obtained by generating multi-foci and fast scanning, for example by using a digital micro-mirror array.

A further step will be to fabricate three-dimensional microstructures with improved smoothness and higher resolution. Higher resolution can be achieved by increasing the NA of the attached microlens. The fabricated lens demonstrated in Chapter 3 is a polymer lens, hence it is likely that the low damage threshold will require to change the material. In the work of Rapp et al. [169], [170], glass structures have been fabricated with photopolymerization. We expect that high NA lenses can be

fabricated in glass material and could be used for endo-printing thanks to the higher damage threshold of glass compared to polymers. Increasing the number of gated fiber modes is necessary to realize the diffraction limited spot size allowed by a high NA lens at its tip. Reducing the fiber diameter and increasing the gating time window are two options. Since the light intensity is inversely proportional to the pulse width and the spot area, we expect that there is an optimal choice of pulse width which would yield a sufficiently high light intensity and small spot size.

A fast and high-resolution endo-printing tool could give additional freedom in fabricating or modifying spaces where the access with a bulk objective lens is limited. In addition, this system could be used for the fabrication of a microstructured or photonic bandgap fiber, which could be fabricated by pulling out of the cylindrical case containing the resin as Figure 5.1 illustrates. Or to fabricate waveguide structures with varying patterns or decreasing diameters (tapers) along z, which is more challenging to achieve in traditional fiber manufacturing.
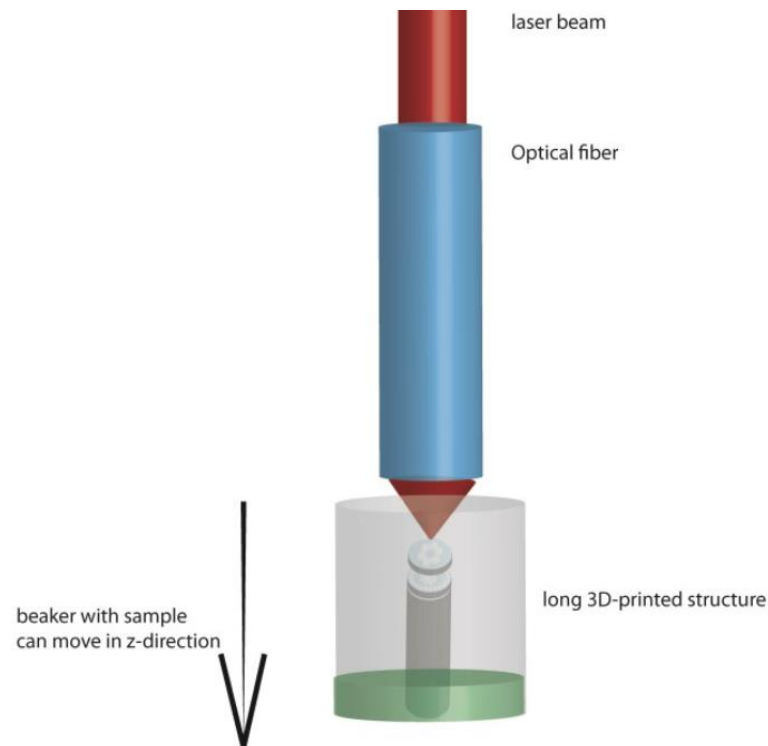
Figure 5.1: Layers of different structures deposited one over the other for fabrication of long structures

References

[1]   T. Wohlers and T. Gornet, "History of additive manufacturing," *Wohlers report*, vol. 24, no. 2014, p. 118, 2014.

[2]   H. Kodama, "Automatic method for fabricating a three-dimensional plastic model with photo-hardening polymer," *Review of scientific instruments*, vol. 52, no. 11, pp. 1770–1773, 1981.

[3]   C. W. Hull, "The birth of 3D printing," *Research-Technology Management*, vol. 58, no. 6, pp. 25–30, 2015.

[4]   M. Bhuvanesh Kumar and P. Sathiya, "Methods and materials for additive manufacturing: A critical review on advancements and challenges," *Thin-Walled Structures*, vol. 159, p. 107228, 2021, doi: https://doi.org/10.1016/j.tws.2020.107228.

[5]   K. v Wong and A. Hernandez, "A review of additive manufacturing," *International scholarly research notices*, vol. 2012, 2012.

[6]   H. Lipson and M. Kurman, *Fabricated: The new world of 3D printing*. John Wiley & Sons, 2013.

[7]   "https://www.3dprintingmedia.network/map-of-additive-manufacturing-technologies/."

[8]   T. D. Ngo, A. Kashani, G. Imbalzano, K. T. Q. Nguyen, and D. Hui, "Additive manufacturing (3D printing): A review of materials, methods, applications and challenges," *Composites Part B: Engineering*, vol. 143, pp. 172–196, 2018.

[9]   M. Mao *et al.*, "The emerging frontiers and applications of high-resolution 3D printing," *Micromachines*, vol. 8, no. 4, pp. 1–20, 2017, doi: 10.3390/mi8040113.

[10]   C. Schubert, M. C. van Langeveld, and L. A. Donoso, "Innovations in 3D printing: a 3D overview from optics to organs," *British Journal of Ophthalmology*, vol. 98, no. 2, pp. 159–161, 2014.

[11]   A. B. Nulty, "3D Printing Part 1-A History and Literature Review Of 3D Printing in Dentistry," 2021.

[12]   C. Xu, J. Liang, and J. Yang, "History of Cardiovascular 3D Printing," in *Cardiovascular 3D Printing*, Springer, 2021, pp. 1–2.

[13]   Q. Yan *et al.*, "A Review of 3D Printing Technology for Medical Applications," *Engineering*, vol. 4, no. 5, pp. 729–742, 2018, doi: https://doi.org/10.1016/j.eng.2018.07.021.

[14]   "https://www.additive.sandvik/en/diamond/."

[15]   N. Shahrubudin, T. C. Lee, and R. Ramlan, "An overview on 3D printing technology: Technological, materials, and applications," *Procedia Manufacturing*, vol. 35, pp. 1286–1296, 2019.

[16]   "https://www.3dnatives.com/en/3d-printing-in-industry-4-0-150220215/."

[17]   B. Berman, "3-D printing: The new industrial revolution," *Business Horizons*, vol. 55, no. 2, pp. 155–162, 2012, doi: https://doi.org/10.1016/j.bushor.2011.11.003.

[18]   A. O. Laplume, B. Petersen, and J. M. Pearce, "Global value chains from a 3D printing perspective," *Journal of International Business Studies*, vol. 47, no. 5, pp. 595–609, 2016, doi: 10.1057/jibs.2015.47.

[19]   M. Attaran, "The rise of 3-D printing: The advantages of additive manufacturing over traditional manufacturing," *Business Horizons*, vol. 60, no. 5, pp. 677–688, 2017.

[20]   S. H. Huang, P. Liu, A. Mokasdar, and L. Hou, "Additive manufacturing and its societal impact: a literature review," *The International Journal of Advanced Manufacturing Technology*, vol. 67, no. 5, pp. 1191–1203, 2013.

[21]   T. Campbell, C. Williams, O. Ivanova, and B. Garrett, "Could 3D printing change the world," *Technologies, Potential, and Implications of Additive Manufacturing, Atlantic Council, Washington, DC*, vol. 3, 2011.

[22]   J. Deckers, J. Vleugels, and J.-P. Kruth, "Additive manufacturing of ceramics: a review," *Journal of Ceramic Science and Technology*, vol. 5, no. 4, pp. 245–260, 2014.

[23]   J. Jang, P. V. W. Sasikumar, F. Navaee, L. Hagelüken, G. Blugan, and J. Brugger, "Electrochemical performance of polymer-derived SiOC and SiTiOC ceramic

electrodes for artificial cardiac pacemaker applications," *Ceramics International*, vol. 47, no. 6, pp. 7593–7601, 2021.

[24]   T. Weigel *et al.*, "A three-dimensional hybrid pacemaker electrode seamlessly integrates into engineered, functional human cardiac tissue in vitro," *Scientific reports*, vol. 8, no. 1, pp. 1–13, 2018.

[25]   G. Li, D. Zhang, S. Wang, and Y. Y. Duan, "Novel passive ceramic based semi-dry electrodes for recording electroencephalography signals from the hairy scalp," *Sensors and Actuators B: Chemical*, vol. 237, pp. 167–178, 2016.

[26]   Dalca, "Microsoft Word - Polymer Derived Ceramics Process in Biomedical Applications Pacemaker Electrode."

[27]   H. Baldus and M. Jansen, "Novel high-performance ceramics—amorphous inorganic networks from molecular precursors," *Angewandte Chemie International Edition in English*, vol. 36, no. 4, pp. 328–343, 1997.

[28]   M. Kakihana, "Synthesis of high-performance ceramics based on polymerizable complex method," *Journal of the Ceramic Society of Japan*, vol. 117, no. 1368, pp. 857–862, 2009.

[29]   E. E. Morales-Delgado, L. Urio, D. B. Conkey, N. Stasio, D. Psaltis, and C. Moser, "Three-dimensional microfabrication through a multimode optical fiber," *Optics express*, vol. 25, no. 6, pp. 7031–7045, 2017.

[30]   P. Delrot, D. Loterie, D. Psaltis, and C. Moser, "Single-photon three-dimensional microfabrication through a multimode optical fiber," *Optics express*, vol. 26, no. 2, pp. 1766–1778, 2018.

[31]   D. B. Conkey *et al.*, "High power, ultrashort pulse control through a multi-core fiber for ablation," *Optics Express*, vol. 25, no. 10, p. 11491, May 2017, doi: 10.1364/oe.25.011491.

[32]   E. Kakkava *et al.*, "Selective femtosecond laser ablation via two-photon fluorescence imaging through a multimode fiber," *Biomedical Optics Express*, vol. 10, no. 2, p. 423, Feb. 2019, doi: 10.1364/boe.10.000423.

[33]   R. Pampuch, *An introduction to ceramics*, vol. 86. Springer, 2014.

[34]   M. W. Barsoum, *Fundamentals of ceramics*. CRC press, 2019.

[35]   W. D. Kingery, H. K. Bowen, and D. R. Uhlmann, *Introduction to ceramics*, vol. 17. John wiley & sons, 1976.

[36]   M. W. Barsoum, *Fundamentals of ceramics*. CRC press, 2019.

[37]   S. Yajima, Y. Hasegawa, J. Hayashi, and M. Iimura, "Synthesis of continuous silicon carbide fibre with high tensile strength and high Young's modulus," *Journal of Materials Science*, vol. 13, no. 12, pp. 2569–2576, 1978.

[38]   S. Yajima, J. Hayashi, and M. Omori, "Continuous silicon carbide fiber of high tensile strength," *Chemistry Letters*, vol. 4, no. 9, pp. 931–934, 1975.

[39]   P. Colombo, G. Mera, R. Riedel, and G. D. Sorarù, "Polymer-Derived Ceramics: 40 Years of Research and Innovation in Advanced Ceramics1)," *Ceramics Science and Technology, Applications*, vol. 4, pp. 245–320, 2013, doi: 10.1002/9783527631971.ch07.

[40]   A. Zocca, P. Colombo, C. M. Gomes, and J. Günster, "Additive manufacturing of ceramics: issues, potentialities, and opportunities," *Journal of the American Ceramic Society*, vol. 98, no. 7, pp. 1983–2001, 2015.

[41]   T. Mühler, C. M. Gomes, J. Heinrich, and J. Günster, "Slurry-based additive manufacturing of ceramics," *International Journal of Applied Ceramic Technology*, vol. 12, no. 1, pp. 18–25, 2015.

[42]   T. Yu, Z. Zhang, Q. Liu, R. Kuliiev, N. Orlovskaya, and D. Wu, "Extrusion-based additive manufacturing of yttria-partially-stabilized zirconia ceramics," *Ceramics International*, vol. 46, no. 4, pp. 5020–5027, 2020, doi: https://doi.org/10.1016/j.ceramint.2019.10.245.

[43]   S. Jang, S. Park, and C. Bae, "Development of ceramic additive manufacturing: process and materials technology," *Biomedical Engineering Letters*, pp. 1–11, 2020.

[44]   P. F. Jacobs, *Rapid prototyping & manufacturing: fundamentals of stereolithography*. Society of Manufacturing Engineers, 1992.

[45]   Z. C. Eckel, C. Zhou, J. H. Martin, A. J. Jacobsen, W. B. Carter, and T. A. Schaedler, "Additive manufacturing of polymer-derived ceramics," *Science*, vol. 58, no. January, pp. 1–10, 2016, doi: 10.1126/science.aad2688.

[46]   M. Schwentenwein, P. Schneider, and J. Homa, "Lithography-based ceramic manufacturing: A novel technique for additive manufacturing of high-performance ceramics," in *Advances in Science and Technology*, 2014, vol. 88, pp. 60–64.

[47]   T. Billiet, M. Vandenhaute, J. Schelfhout, S. van Vlierberghe, and P. Dubruel, "A review of trends and limitations in hydrogel-rapid prototyping for tissue engineering," *Biomaterials*, vol. 33, no. 26, pp. 6020–6041, 2012.

[48] "https://www.lithoz.com/."

[49] P. Colombo, *Polymer derived ceramics: from nano-structure to applications*. DEStech Publications, Inc, 2010.

[50] B. E. A. Saleh and M. C. Teich, *Fundamentals of photonics*. john Wiley & sons, 2019.

[51] T Baldacchini, *Three-Dimensional Microfabrication Using Two-photon Polymerization*. Elsevier, 2016. doi: 10.1016/C2014-0-01016-7.

[52] P. T. C. So, "Two-photon fluorescence light microscopy," *e LS*, 2001.

[53] "https://microscopy.berkeley.edu/courses/TLM/2P/index.html."

[54] P. W. Milonni and J. H. Eberly, "Laser Physics. 2010." John Wiley & Sons.

[55] W. Denk, J. H. Strickler, and W. W. Webb, "Two-photon laser scanning fluorescence microscopy," *Science*, vol. 248, no. 4951, pp. 73–76, 1990.

[56] S. Maruo, O. Nakamura, and S. Kawata, "Three-dimensional microfabrication with two-photon-absorbed photopolymerization," *Optics letters*, vol. 22, no. 2, pp. 132–134, 1997.

[57] L. Li, R. R. Gattass, E. Gershgoren, H. Hwang, and J. T. Fourkas, "Achieving λ/20 resolution by one-color initiation and deactivation of polymerization," *Science*, vol. 324, no. 5929, pp. 910–913, 2009.

[58] L. Li, R. R. Gattass, E. Gershgoren, H. Hwang, and J. T. Fourkas, "Achieving λ/20 resolution by one-color initiation and deactivation of polymerization," *Science*, vol. 324, no. 5929, pp. 910–913, 2009.

[59] J. Stampfl, R. Liska, and A. Ovsianikov, *Multiphoton lithography: Techniques, materials, and applications*. John Wiley & Sons, 2016.

[60] G. P. Agrawal, "Nonlinear fiber optics," in *Nonlinear Science at the Dawn of the 21st Century*, Springer, 2000, pp. 195–211.

[61] L. Thevenaz, *Advanced fiber optics: concepts and technology*. EPFL press, 2011.

[62] P. Sheng and B. van Tiggelen, "Introduction to Wave Scattering, Localization and Mesoscopic Phenomena." Taylor & Francis, 2007.

[63] E. Hecht, *Optik*. Walter de Gruyter GmbH & Co KG, 2018.

[64] D. C.-M. Loterie, "Microscopy and digital light shaping through optical fibers," 2017.

[65]   I. N. Papadopoulos, S. Farahi, C. Moser, and D. Psaltis, "Focusing and scanning light through a multimode optical fiber using digital phase conjugation," *Optics express*, vol. 20, no. 10, pp. 10583–10590, 2012.

[66]   I. N. Papadopoulos, S. Farahi, C. Moser, and D. Psaltis, "High-resolution, lensless endoscope based on digital scanning through a multimode optical fiber," *Biomedical optics express*, vol. 4, no. 2, pp. 260–270, 2013.

[67]   E. E. Morales-Delgado, S. Farahi, I. N. Papadopoulos, D. Psaltis, and C. Moser, "Delivery of focused short pulses through a multimode fiber," *Optics express*, vol. 23, no. 7, pp. 9109–9120, 2015.

[68]   E. E. Morales-Delgado, D. Psaltis, and C. Moser, "Two-photon imaging through a multimode fiber," *Optics express*, vol. 23, no. 25, pp. 32158–32170, 2015.

[69]   D. Loterie, S. Farahi, I. Papadopoulos, A. Goy, D. Psaltis, and C. Moser, "Digital confocal microscopy through a multimode fiber," *Optics express*, vol. 23, no. 18, pp. 23845–23858, 2015.

[70]   P. Delrot, D. Loterie, D. Psaltis, and C. Moser, "Single-photon three-dimensional microfabrication through a multimode optical fiber," *Optics express*, vol. 26, no. 2, pp. 1766–1778, 2018.

[71]   D. Loterie, P. Delrot, and C. Moser, "Volumetric 3D printing of elastomers by tomographic back-projection," *Preprint at https://doi. org/10.13140/RG*, vol. 2, no. 20027.46889, 2018.

[72]   "https://www.sciencedirect.com/topics/earth-and-planetary-sciences/radon-transform."

[73]   S. R. Deans, *The Radon transform and some of its applications*. Courier Corporation, 2007.

[74]   rp photonics, "rp photonics, absorption." 2021. [Online]. Available: https://www.rp-photonics.com/absorption.html

[75]   simphotek, "single-photon absorption." 2021. [Online]. Available: http://www.simphotek.net/bckg/bckg.spa.html

[76]   M. Shusteff *et al.*, "Additive fabrication of 3d structures by holographic lithography," 2016.

[77]   M. Shusteff *et al.*, "One-step volumetric additive manufacturing of complex polymer structures," *Science advances*, vol. 3, no. 12, p. eaao5496, 2017.

[78] B. E. Kelly, I. Bhattacharya, H. Heidari, M. Shusteff, C. M. Spadaccini, and H. K. Taylor, "Volumetric additive manufacturing via tomographic reconstruction," *Science*, vol. 363, no. 6431, pp. 1075–1079, 2019.

[79] D. Loterie, P. Delrot, and C. Moser, "High-resolution tomographic volumetric additive manufacturing," *Nature communications*, vol. 11, no. 1, pp. 1–6, 2020.

[80] J. Madrid-Wolff, A. Boniface, D. Loterie, P. Delrot, and C. Moser, "Light-based Volumetric Additive Manufacturing in Scattering Resins," *arXiv preprint arXiv:2105.14952*, 2021.

[81] G. Konstantinou *et al.*, "Additive micro-manufacturing of crack-free PDCs by two-photon polymerization of a single, low-shrinkage preceramic resin," *Additive Manufacturing*, vol. 35, p. 101343, 2020.

[82] Z. Chen *et al.*, "3D printing of ceramics: A review," *Journal of the European Ceramic Society*, vol. 39, no. 4, pp. 661–687, 2019, doi: 10.1016/j.jeurceramsoc.2018.11.013.

[83] Z. C. Eckel, C. Zhou, J. H. Martin, A. J. Jacobsen, W. B. Carter, and T. A. Schaedler, "Additive manufacturing of polymer-derived ceramics," *Science*, vol. 58, no. January, pp. 1–10, 2016, doi: 10.1126/science.aad2688.

[84] S. M. Cima *et al.*, "Three Dimensional Printing: Rapid Tooling and Prototypes Directly from CAD Representation."

[85] A. Cattoni *et al.*, "Sub-10nm electron and helium ion beam lithography using a recently developed alumina resist," *Microelectronic Engineering*, vol. 193, pp. 18–22, 2018, doi: https://doi.org/10.1016/j.mee.2018.02.015.

[86] Y. Tian, G. Shao, X. Wang, and L. An, "Fabrication of nano-scaled polymer-derived SiAlCN ceramic components using focused ion beam," *Journal of Micromechanics and Microengineering*, vol. 23, no. 9, p. 095035, 2013.

[87] R. Galante, C. G. Figueiredo-Pina, and A. P. Serro, "Additive manufacturing of ceramics for dental applications: A review," *Dental Materials*, vol. 35, no. 6. Elsevier Inc., pp. 825–846, Jun. 01, 2019. doi: 10.1016/j.dental.2019.02.026.

[88] V. v. Mitic *et al.*, "Fractal frontiers in microelectronic ceramic materials," *Ceramics International*, vol. 45, no. 7, pp. 9679–9685, May 2019, doi: 10.1016/j.ceramint.2019.01.020.

[89] P. Colombo, G. Mera, R. Riedel, and G. D. Soraru, "Polymer-derived ceramics: 40 years of research and innovation in advanced ceramics," *Journal of the American Ceramic Society*, vol. 93, no. 7, pp. 1805–1837, 2010.

[90] L. Brigo, J. E. M. Schmidt, A. Gandin, N. Michieli, P. Colombo, and G. Brusatin, "3D Nanofabrication of SiOC Ceramic Structures," *Advanced Science*, vol. 5, no. 12, 2018, doi: 10.1002/advs.201800937.

[91] D. Gailevičius, V. Padolskytė, L. Mikoliūnaitė, S. Šakirzanovas, S. Juodkazis, and M. Malinauskas, "Additive-manufacturing of 3D glass-ceramics down to nanoscale resolution," *Nanoscale Horizons*, pp. 2–6, 2018, doi: 10.1039/c8nh00293b.

[92] A. Vyatskikh, R. C. Ng, B. Edwards, and J. R. Greer, "Additive manufacturing of titanium dioxide for dielectric photonic crystals," in *Advanced Fabrication Technologies for Micro/Nano Optics and Photonics XII*, 2019, vol. 10930, p. 109300H.

[93] P. Colombo, G. Mera, R. Riedel, and G. D. Soraru, "Polymer-derived ceramics: 40 years of research and innovation in advanced ceramics," *Journal of the American Ceramic Society*, vol. 93, no. 7, pp. 1805–1837, 2010.

[94] "POLYRAMIC® RESINS BROCHURE Inorganic polymers for flame resistant and pre-ceramic applications."

[95] R. Riedel and I.-W. Chen, *Ceramics science and technology, volume 3: synthesis and processing*. John Wiley & Sons, 2011.

[96] N. P. Bansal and A. R. Boccaccini, *Ceramics and composites processing methods*. John Wiley & Sons, 2012.

[97] S. Martínez-Crespiera, E. Ionescu, H.-J. Kleebe, and R. Riedel, "Pressureless synthesis of fully dense and crack-free SiOC bulk ceramics via photo-crosslinking and pyrolysis of a polysiloxane," *Journal of the European Ceramic Society*, vol. 31, no. 5, pp. 913–919, 2011.

[98] J. Bauer *et al.*, "Additive manufacturing of ductile, ultrastrong polymer-derived nanoceramics," *Matter*, vol. 1, no. 6, pp. 1547–1556, 2019.

[99] C. Crook *et al.*, "Plate-nanolattices at the theoretical limit of stiffness and strength," *Nature communications*, vol. 11, no. 1, pp. 1–11, 2020.

[100] P. Vallachira Warriam Sasikumar *et al.*, "In Vitro Cytocompatibility Assessment of Ti-Modified, Silicon-oxycarbide-Based, Polymer-Derived, Ceramic-Implantable

Electrodes under Pacing Conditions," *ACS applied materials & interfaces*, vol. 12, no. 15, pp. 17244–17253, 2020.

[101]   G. Mera, A. Navrotsky, S. Sen, H.-J. Kleebe, and R. Riedel, "Polymer-derived SiCN and SiOC ceramics–structure and energetics at the nanoscale," *Journal of Materials Chemistry A*, vol. 1, no. 12, pp. 3826–3836, 2013.

[102]   S. Park, D.-H. Lee, H.-I. Ryoo, T.-W. Lim, D.-Y. Yang, and D.-P. Kim, "Fabrication of three-dimensional SiC ceramic microstructures with near-zero shrinkage via dual crosslinking induced stereolithography," *Chemical communications*, no. 32, pp. 4880–4882, 2009.

[103]   X. Wang, F. Schmidt, D. Hanaor, P. H. Kamm, S. Li, and A. Gurlo, "Additive manufacturing of ceramics from preceramic polymers: A versatile stereolithographic approach assisted by thiol-ene click chemistry," *Additive Manufacturing*, vol. 27, no. February, pp. 80–90, 2019, doi: 10.1016/j.addma.2019.02.012.

[104]   T. A. Pham, D. Kim, T. Lim, S. Park, D. Yang, and K. Lee, "Three-dimensional SiCN ceramic microstructures via nano-stereolithography of inorganic polymer photoresists," *Advanced Functional Materials*, vol. 16, no. 9, pp. 1235–1241, 2006.

[105]   E. Ionescu, "Polymer-Derived Ceramics," in *Ceramics Science and Technology*, John Wiley & Sons, Ltd, 2013, pp. 457–500. doi: https://doi.org/10.1002/9783527631940.ch49.

[106]   N. GmbH, "Nanoscribe Photonic Professional GT - User Manual," 2017. [Online]. Available: www.nanoscribe.com

[107]   B. S. Haq, H. U. Khan, K. Alam, M. Ajmal, S. Attaullah, and I. Zari, "Determination of two-photon absorption cross sections of photosensitizers and its implications for two-photon polymerization," *Applied Optics*, vol. 54, no. 1, p. 132, 2014, doi: 10.1364/ao.54.000132.

[108]   P. J. Flory, *Principles of polymer chemistry*. Cornell University Press, 1953.

[109]   E. E. Morales-Delgado, L. Urio, D. B. Conkey, N. Stasio, D. Psaltis, and C. Moser, "Three-dimensional microfabrication through a multimode optical fiber," *Optics express*, vol. 25, no. 6, pp. 7031–7045, 2017.

[110]   J. B. Mueller, J. Fischer, F. Mayer, M. Kadic, and M. Wegener, "Polymerization Kinetics in Three-Dimensional Direct Laser Writing," *Advanced Materials*, vol. 26, no. 38, pp. 6566–6571, 2014.

[111] P. Delrot, D. Loterie, D. Psaltis, and C. Moser, "Single-photon three-dimensional microfabrication through a multimode optical fiber," *Optics Express*, vol. 26, no. 2, p. 1766, 2018, doi: 10.1364/oe.26.001766.

[112] J. S. Oakdale, J. Ye, W. L. Smith, and J. Biener, "Post-print UV curing method for improving the mechanical properties of prototypes derived from two-photon lithography," *Optics express*, vol. 24, no. 24, pp. 27077–27086, 2016.

[113] B. Cardenas-Benitez *et al.*, "Pyrolysis-induced shrinking of three-dimensional structures fabricated by two-photon polymerization: experiment and theoretical model," *Microsystems & nanoengineering*, vol. 5, no. 1, pp. 1–13, 2019.

[114] Z. Xu, K. Cheng, X. Zhou, J. Lin, and X. Jing, "An adaptive direct slicing method based on tilted voxel of two-photon polymerization," *The International Journal of Advanced Manufacturing Technology*, vol. 96, no. 1–4, pp. 521–530, 2018.

[115] S. H. Park, S. H. Lee, D.-Y. Yang, H. J. Kong, and K.-S. Lee, "Subregional slicing method to increase three-dimensional nanofabrication efficiency in two-photon polymerization," *Applied Physics Letters*, vol. 87, no. 15, p. 154108, 2005.

[116] J. M. Kim and H. Muramatsu, "Two-photon photopolymerized tips for adhesion-free scanning-probe microscopy," *Nano letters*, vol. 5, no. 2, pp. 309–314, 2005.

[117] S. You, P. Wang, J. Schimelman, H. H. Hwang, and S. Chen, "High-fidelity 3D printing using flashing photopolymerization," *Additive manufacturing*, vol. 30, p. 100834, 2019.

[118] X. Tian, D. Li, Z. Chen, and W. Zhou, "Study on the fabrication accuracy of ceramic parts by direct stereolithography: Ceramic parts can be prepared using stereolithography by building composite parts from ceramic powder-loaded resins, followed by simultaneous polymer pyrolysis and ceramic sintering. This paper describes a systematic study into the influence of several parameters on the accuracy of such parts," *Virtual and Physical Prototyping*, vol. 7, no. 3, pp. 195–202, 2012.

[119] J. F. Moulder, "Handbook of X-ray photoelectron spectroscopy," *Physical electronics*, pp. 230–232, 1995.

[120] J. Kaspar, M. Graczyk-Zajac, and R. Riedel, "Carbon-rich SiOC anodes for lithium-ion batteries: Part II. Role of thermal cross-linking," *Solid State Ionics*, vol. 225, pp. 527–531, 2012.

[121] S. Martínez-Crespiera *et al.*, "Fabrication of silicon oxycarbide-based microcomponents via photolithographic and soft lithography approaches," *Sensors and Actuators A: Physical*, vol. 169, no. 1, pp. 242–249, 2011.

[122] S. Yu, R. Tu, and T. Goto, "Preparation of SiOC nanocomposite films by laser chemical vapor deposition," *Journal of the European Ceramic Society*, vol. 36, no. 3, pp. 403–409, 2016.

[123] J. v Ryan and C. G. Pantano, "Synthesis and characterization of inorganic silicon oxycarbide glass thin films by reactive rf-magnetron sputtering," *Journal of Vacuum Science & Technology A: Vacuum, Surfaces, and Films*, vol. 25, no. 1, pp. 153–159, 2007.

[124] A. Vashisth, S. Khatri, S. H. Hahn, W. Zhang, A. C. T. van Duin, and M. Naraghi, "Mechanical size effects of amorphous polymer-derived ceramics at the nanoscale: experiments and ReaxFF simulations," *Nanoscale*, vol. 11, no. 15, pp. 7447–7456, 2019.

[125] G. D. Sorarù, S. Modena, E. Guadagnino, P. Colombo, J. Egan, and C. Pantano, "Chemical durability of silicon oxycarbide glasses," *Journal of the American Ceramic Society*, vol. 85, no. 6, pp. 1529–1536, 2002.

[126] C. Liao, A. Wuethrich, and M. Trau, "A material odyssey for 3D nano/microstructures: two photon polymerization based nanolithography in bioapplications," *Applied Materials Today*, vol. 19, p. 100635, 2020.

[127] M. Farsari and B. N. Chichkov, "Materials processing: Two-photon fabrication," *Nature Photonics*, vol. 3, no. 8, pp. 450–452, 2009, doi: 10.1038/nphoton.2009.131.

[128] A. Selimis and M. Farsari, *Laser-Based 3D Printing and surface texturing*, vol. 3–3. Elsevier Ltd., 2016. doi: 10.1016/B978-0-12-803581-8.09171-2.

[129] K. Lee, D. Yang, S. H. Park, and R. H. Kim, "Recent developments in the use of two-photon polymerization in precise 2D and 3D microfabrications," *Polymers for advanced technologies*, vol. 17, no. 2, pp. 72–82, 2006.

[130] F. Perrucci *et al.*, "Optimization of a suspended two photon polymerized microfluidic filtration system," *Microelectronic Engineering*, vol. 195, pp. 95–100, 2018.

[131] S. D. Gittard, A. Ovsianikov, B. N. Chichkov, A. Doraiswamy, and R. J. Narayan, "Two-photon polymerization of microneedles for transdermal drug delivery," *Expert opinion on drug delivery*, vol. 7, no. 4, pp. 513–533, 2010.

[132] Y.-J. Liu *et al.*, "A simple and direct reading flow meter fabricated by two-photon polymerization for microfluidic channel," *Microfluidics and Nanofluidics*, vol. 18, no. 3, pp. 427–431, 2015.

[133] J.-F. Xing, M.-L. Zheng, and X.-M. Duan, "Two-photon polymerization microfabrication of hydrogels: an advanced 3D printing technology for tissue engineering and drug delivery," *Chemical Society Reviews*, vol. 44, no. 15, pp. 5031–5039, 2015.

[134] A. Tijore *et al.*, "Two-photon lithography and microscopy of 3D hydrogel scaffolds for neuronal cell growth Two-photon lithography and microscopy of 3D hydrogel scaffolds for neuronal cell growth," *Biomedical Physics & Engineering Express*, vol. 4, no. 2, p. 27009, doi: 10.1088/2057-1976/aaab93.

[135] X. H. Qin, A. Ovsianikov, J. Stampfl, and R. Liska, "Additive manufacturing of photosensitive Hydrogels for tissue engineering applications," *BioNanoMaterials*, vol. 15, no. 3–4, pp. 49–70, 2014, doi: 10.1515/bnm-2014-0008.

[136] A. Bertoncini and C. Liberale, "3D printed waveguides based on photonic crystal fiber designs for complex fiber-end photonic devices," *Optica*, vol. 7, no. 11, pp. 1487–1494, 2020, doi: 10.1364/OPTICA.397281.

[137] A. Bertoncini, S. P. Laptenok, L. Genchi, V. P. Rajamanickam, and C. Liberale, "3D-Printed high-NA catadioptric thin lens for suppression of XPM background in Stimulated Raman Scattering microscopy," *Journal of Biophotonics*, vol. 14, no. 5, p. e202000219, 2021.

[138] M. Malinauskas *et al.*, "Ultrafast laser processing of materials: from science to industry," *Light: Science & Applications*, vol. 5, no. 8, pp. e16133–e16133, 2016, doi: 10.1038/lsa.2016.133.

[139] V. Melissinaki, M. Farsari, and S. Pissadakis, "A Fiber-Endface, Fabry–Perot Vapor Microsensor Fabricated by Multiphoton Polymerization," *IEEE Journal of Selected Topics in Quantum Electronics*, vol. 21, no. 4, pp. 344–353, 2015, doi: 10.1109/JSTQE.2014.2381463.

[140] P. J. Flory, *Principles of polymer chemistry*. Cornell University Press, 1953.

[141] Y. Chen, T. Furukawa, T. Ibi, Y. Noda, and S. Maruo, "Multi-scale micro-stereolithography using optical fibers with a photocurable ceramic slurry," *Optical Materials Express*, vol. 11, no. 1, pp. 105–114, 2021.

[142]   T. Ibi, E. Komada, T. Furukawa, and S. Maruo, "Multi-scale, multi-depth lithography using optical fibers for microfluidic applications," *Microfluidics and Nanofluidics*, vol. 22, no. 6, p. 69, 2018, doi: 10.1007/s10404-018-2087-8.

[143]   J. S. Choi, H.-W. Kang, I. H. Lee, T. J. Ko, and D.-W. Cho, "Development of micro-stereolithography technology using a UV lamp and optical fiber," *The International Journal of Advanced Manufacturing Technology*, vol. 41, no. 3, pp. 281–286, 2009, doi: 10.1007/s00170-008-1461-1.

[144]   D. B. Conkey, A. M. Caravaca-Aguirre, and R. Piestun, "High-speed scattering medium characterization with application to focusing light through turbid media," *Optics express*, vol. 20, no. 2, pp. 1733–1740, 2012.

[145]   A. M. Caravaca-Aguirre, E. Niv, D. B. Conkey, and R. Piestun, "Real-time resilient focusing through a bending multimode fiber," *Optics express*, vol. 21, no. 10, pp. 12881–12887, 2013.

[146]   S. Sivankutty, E. R. Andresen, R. Cossart, G. Bouwmans, S. Monneret, and H. Rigneault, "Ultra-thin rigid endoscope: two-photon imaging through a graded-index multi-mode fiber," *Optics express*, vol. 24, no. 2, pp. 825–841, 2016.

[147]   A. Boniface, J. Dong, and S. Gigan, "Non-invasive focusing and imaging in scattering media with a fluorescence-based transmission matrix," *Nature communications*, vol. 11, no. 1, pp. 1–7, 2020.

[148]   S. M. Popoff, G. Lerosey, R. Carminati, M. Fink, A. C. Boccara, and S. Gigan, "Measuring the transmission matrix in optics: an approach to the study and control of light propagation in disordered media," *Physical review letters*, vol. 104, no. 10, p. 100601, 2010.

[149]   I. M. Vellekoop and A. P. Mosk, "Focusing coherent light through opaque strongly scattering media," *Optics letters*, vol. 32, no. 16, pp. 2309–2311, 2007.

[150]   J. Aulbach, B. Gjonaj, P. M. Johnson, A. P. Mosk, and A. Lagendijk, "Control of light transmission through opaque scattering media in space and time," *Physical review letters*, vol. 106, no. 10, p. 103901, 2011.

[151]   M. Mounaix *et al.*, "Spatiotemporal coherent control of light through a multiple scattering medium with the multispectral transmission matrix," *Physical review letters*, vol. 116, no. 25, p. 253901, 2016.

[152]   S. Rotter and S. Gigan, "Light fields in complex media: Mesoscopic scattering meets wave control," *Reviews of Modern Physics*, vol. 89, no. 1, p. 015005, 2017.

[153] E. Kakkava *et al.*, "Selective femtosecond laser ablation via two-photon fluorescence imaging through a multimode fiber," *Biomedical Optics Express*, vol. 10, no. 2, p. 423, 2019, doi: 10.1364/boe.10.000423.

[154] D. B. Conkey *et al.*, "High power, ultrashort pulse control through a multi-core fiber for ablation," *Optics Express*, vol. 25, no. 10, p. 11491, 2017, doi: 10.1364/oe.25.011491.

[155] A. Boniface, M. Mounaix, B. Blochet, R. Piestun, and S. Gigan, "Transmission-matrix-based point-spread-function engineering through a complex medium," *Optica*, vol. 4, no. 1, pp. 54–59, 2017.

[156] S. Popoff, G. Lerosey, M. Fink, A. C. Boccara, and S. Gigan, "Image transmission through an opaque material," *Nature communications*, vol. 1, no. 1, pp. 1–5, 2010.

[157] T. Zandrini, O. Shan, V. Parodi, G. Cerullo, M. T. Raimondi, and R. Osellame, "Multi-foci laser microfabrication of 3D polymeric scaffolds for stem cell expansion in regenerative medicine," *Scientific Reports*, vol. 9, no. 1, p. 11761, 2019, doi: 10.1038/s41598-019-48080-w.

[158] P. Somers, Z. Liang, J. E. Johnson, B. W. Boudouris, L. Pan, and X. Xu, "Rapid, continuous projection multi-photon 3D printing enabled by spatiotemporal focusing of femtosecond pulses," *Light: Science & Applications*, vol. 10, no. 1, p. 199, 2021, doi: 10.1038/s41377-021-00645-z.

[159] M. Manousidaki, D. G. Papazoglou, M. Farsari, and S. Tzortzakis, "3D holographic light shaping for advanced multiphoton polymerization," *Optics Letters*, vol. 45, no. 1, pp. 85–88, 2020, doi: 10.1364/OL.45.000085.

[160] D. Yang, L. Liu, Q. Gong, and Y. Li, "Rapid two-photon polymerization of an arbitrary 3D microstructure with 3D focal field engineering," *Macromolecular rapid communications*, vol. 40, no. 8, p. 1900041, 2019.

[161] H. Kim and S. K. Saha, "Defect control during femtosecond projection two-photon lithography," *Procedia Manufacturing*, vol. 48, pp. 650–655, 2020.

[162] S. K. Saha, D. Wang, V. H. Nguyen, Y. Chang, J. S. Oakdale, and S. C. Chen, "Scalable submicrometer additive manufacturing," *Science*, vol. 366, no. 6461, pp. 105–109, 2019, doi: 10.1126/science.aax8760.

[163] Y.-H. Liu *et al.*, "λ/12 Super Resolution Achieved in Maskless Optical Projection Nanolithography for Efficient Cross-Scale Patterning," *Nano Letters*, vol. 21, no. 9, pp. 3915–3921, 2021.

[164] Q. Geng, D. Wang, P. Chen, and S.-C. Chen, "Ultrafast multi-focus 3-D nano-fabrication based on two-photon polymerization," *Nature communications*, vol. 10, no. 1, pp. 1–7, 2019.

[165] P. Mueller, M. Thiel, and M. Wegener, "3D direct laser writing using a 405 nm diode laser," *Optics letters*, vol. 39, no. 24, pp. 6847–6850, 2014.

[166] J. Fischer, J. B. Mueller, J. Kaschke, T. J. A. Wolf, A.-N. Unterreiner, and M. Wegener, "Three-dimensional multi-photon direct laser writing with variable repetition rate," *Optics express*, vol. 21, no. 22, pp. 26244–26260, 2013.

[167] S. Bianchi, V. P. Rajamanickam, L. Ferrara, E. di Fabrizio, C. Liberale, and R. di Leonardo, "Focusing and imaging with increased numerical apertures through multimode fibers with micro-fabricated optics," *Optics letters*, vol. 38, no. 23, pp. 4935–4938, 2013.

[168] T. Gissibl, S. Thiele, A. Herkommer, and H. Giessen, "Two-photon direct laser writing of ultracompact multi-lens objectives," *Nature Photonics*, vol. 10, no. 8, pp. 554–560, 2016.

[169] F. Kotz *et al.*, "Three-dimensional printing of transparent fused silica glass," *Nature*, vol. 544, no. 7650, pp. 337–339, 2017.

[170] D. Helmer and B. E. Rapp, "Divide and print," *Nature Materials*, vol. 19, no. 2, pp. 131–133, 2020, doi: 10.1038/s41563-019-0594-y.

[171] J. Schmidt and P. Colombo, "Digital light processing of ceramic components from polysiloxanes," *Journal of the European Ceramic Society*, vol. 38, no. 1, pp. 57–66, 2018.

[172] J. Schmidt, L. Brigo, A. Gandin, M. Schwentenwein, P. Colombo, and G. Brusatin, "Multiscale ceramic components from preceramic polymers by hybridization of vat polymerization-based technologies," *Additive Manufacturing*, vol. 30, p. 100913, 2019.

[173] J. Jiang, X. Xu, and J. Stringer, "Support structures for additive manufacturing: a review," *Journal of Manufacturing and Materials Processing*, vol. 2, no. 4, p. 64, 2018.

[174] P. N. Bernal *et al.*, "Volumetric bioprinting of complex living-tissue constructs within seconds," *Advanced materials*, vol. 31, no. 42, p. 1904209, 2019.

[175] M. Regehly *et al.*, "Xolography for linear volumetric 3D printing," *Nature*, vol. 588, no. 7839, pp. 620–624, 2020.

[176] C. C. Cook *et al.*, "Highly Tunable Thiol-Ene Photoresins for Volumetric Additive Manufacturing," *Advanced Materials*, vol. 32, no. 47, p. 2003376, 2020.

[177] J. Lalevée and J.-P. Fouassier, *Dyes and chromophores in polymer science*. John Wiley & Sons, 2015.

[178] A. Eibel, D. E. Fast, and G. Gescheidt, "Choosing the ideal photoinitiator for free radical photopolymerizations: Predictions based on simulations using established data," *Polymer Chemistry*, vol. 9, no. 41, pp. 5107–5115, 2018.

[179] S. Slavin, K. McEwan, and D. M. Haddleton, "Cobalt-Catalyzed Chain Transfer Polymerization: A Review," *Polymer Science: A Comprehensive Reference, 10 Volume Set*, pp. 249–275, 2012.

[180] J. Chastain and R. C. King Jr, "Handbook of X-ray photoelectron spectroscopy," *Perkin-Elmer, USA*, p. 261, 1992.

[181] S. C. Ligon, B. Husár, H. Wutzel, R. Holman, and R. Liska, "Strategies to reduce oxygen inhibition in photoinduced polymerization," *Chemical reviews*, vol. 114, no. 1, pp. 557–589, 2014.

[182] P. J. Flory, "Molecular size distribution in three dimensional polymers. I. Gelation1," *Journal of the American Chemical Society*, vol. 63, no. 11, pp. 3083–3090, 1941.

[183] S. Shoji and S. Kawata, "Optically-induced growth of fiber patterns into a photopolymerizable resin," *Applied physics letters*, vol. 75, no. 5, pp. 737–739, 1999.

[184] Y. Liu *et al.*, "3D printing of ceramic cellular structures for potential nuclear fusion application," *Additive Manufacturing*, vol. 35, p. 101348, 2020.

[185] C. He *et al.*, "Polymer-derived SiOC ceramic lattice with thick struts prepared by digital light processing," *Additive Manufacturing*, vol. 35, p. 101366, 2020.

[186] J. M. Hundley *et al.*, "Geometric characterization of additively manufactured polymer derived ceramics," *Additive Manufacturing*, vol. 18, pp. 95–102, 2017.

[187] U. K. Roopavath, S. Malferrari, A. van Haver, F. Verstreken, S. N. Rath, and D. M. Kalaskar, "Optimization of extrusion based ceramic 3D printing process for complex bony designs," *Materials & Design*, vol. 162, pp. 263–270, 2019.

[188] E. Zanchetta *et al.*, "Stereolithography of SiOC ceramic microcomponents," *Advanced Materials*, vol. 28, no. 2, pp. 370–376, 2016.

[189]   M. Makowska *et al.*, "Cracks, porosity and microstructure of Ti modified polymer-derived SiOC revealed by absorption-, XRD-and XRF-contrast 2D and 3D imaging," *Acta Materialia*, vol. 198, pp. 134–144, 2020.

[190]   G. Liu, J. Kaspar, L. M. Reinold, M. Graczyk-Zajac, and R. Riedel, "Electrochemical performance of DVB-modified SiOC and SiCN polymer-derived negative electrodes for lithium-ion batteries," *Electrochimica Acta*, vol. 106, pp. 101–108, 2013.

[191]   M. Graczyk-Zajac, L. Toma, C. Fasel, and R. Riedel, "Carbon-rich SiOC anodes for lithium-ion batteries: Part I. Influence of material UV-pre-treatment on high power properties," *Solid State Ionics*, vol. 225, pp. 522–526, 2012.

[192]   P. V. W. Sasikumar *et al.*, "Polymer derived silicon oxycarbide ceramic monoliths: Microstructure development and associated materials properties," *Ceramics International*, vol. 44, no. 17, pp. 20961–20967, 2018.

[193]   A. Sonseca and M. el Fray, "Enzymatic synthesis of an electrospinnable poly (butylene succinate-co-dilinoleic succinate) thermoplastic elastomer," *RSC advances*, vol. 7, no. 34, pp. 21258–21267, 2017.

[194]:   "https : / / orgchemboulder . com / Spectroscopy / irtutor / tutorial.shtml."

[195]   "https : / / www . spectroscopyonline . com / view / group-wavenumbers-and-introduction-spectroscopy-benzene-rings."

[196]   "https://www.cpp.edu/~psbeauchamp/pdf/spec_ir_nmr_ spectra_tables.pdf."

[197]   "http : / / www . rsc . org / suppdata / c8 / ra / c8ra02045k / c8ra02045k1.pdf."

[198]   "https : / / www . gelest . com / wp - content / uploads / 5000A _ Section1_InfraredAnalysis.pdf."

[199]   J. Kaspar, M. Graczyk-Zajac, and R. Riedel, "Lithium insertion into carbon-rich SiOC ceramics: Influence of pyrolysis temperature on electrochemical properties," *Journal of power sources*, vol. 244, pp. 450–455, 2013.

[200]   A. Łapiński, J. Spanget-Larsen, M. Langgård, J. Waluk, and J. G. Radziszewski, "Raman spectrum of the phenyl radical," *The Journal of Physical Chemistry A*, vol. 105, no. 46, pp. 10520–10524, 2001.

[201]   L. B. Capeletti, I. M. Baibich, I. S. Butler, and J. H. Z. dos Santos, "Infrared and Raman spectroscopic characterization of some organic substituted hybrid silicas," *Spectrochimica Acta Part A: Molecular and Biomolecular Spectroscopy*, vol. 133, pp. 619–625, 2014.

[202] D. S. Knight and W. B. White, "Characterization of diamond films by Raman spectroscopy," *Journal of Materials Research*, vol. 4, no. 2, pp. 385–393, 1989.

[203] T. Jiang, Y. Wang, Y. Wang, N. Orlovskaya, and L. An, "Quantitative raman analysis of free carbon in polymer-derived ceramics," *Journal of the American Ceramic Society*, vol. 92, no. 10, pp. 2455–2458, 2009.

[204] P. Dibandjo, M. Graczyk-Zajac, R. Riedel, V. S. Pradeep, and G. D. A. Soraru, "Lithium insertion into dense and porous carbon-rich polymer-derived SiOC ceramics," *Journal of the European Ceramic Society*, vol. 32, no. 10, pp. 2495–2503, 2012.

[205] A. B. Kousaalya, X. Zeng, M. Karakaya, T. Tritt, S. Pilla, and A. M. Rao, "Polymer-derived silicon oxycarbide ceramics as promising next-generation sustainable thermoelectrics," *ACS applied materials & interfaces*, vol. 10, no. 3, pp. 2236–2241, 2018.

[206] G. D. Sorarù, G. D'Andrea, and A. Glisenti, "XPS characterization of gel-derived silicon oxycarbide glasses," *Materials Letters*, vol. 27, no. 1–2, pp. 1–5, 1996.

[207] R. J. P. Corriu, D. Leclercq, P. H. Mutin, and A. Vioux, "Preparation and structure of silicon oxycarbide glasses derived from polysiloxane precursors," *Journal of Sol-Gel Science and Technology*, vol. 8, no. 1, pp. 327–330, 1997.

[208] C. Sugie, A. Navrotsky, S. Lauterbach, H.-J. Kleebe, and G. Mera, "Structure and Thermodynamics of Silicon Oxycarbide Polymer-Derived Ceramics with and without Mixed-Bonding," *Materials*, vol. 14, no. 15, p. 4075, 2021.

[209] J. A. Gardella Jr, S. A. Ferguson, and R. L. Chin, "$\pi^* \leftarrow \pi$ shakeup satellites for the analysis of structure and bonding in aromatic polymers by X-ray photoelectron spectroscopy," *Applied spectroscopy*, vol. 40, no. 2, pp. 224–232, 1986.

[210] J. Schindelin *et al.*, "Fiji: an open-source platform for biological-image analysis," *Nature methods*, vol. 9, no. 7, pp. 676–682, 2012.

Curriculum Vitae

<u>Georgia Konstantinou</u>

Date of birth: December 7, 1988
Mobile: +41786952715, e-mail: mgkonstantinou@gmail.com
Currently in Lausanne

Professional expertise

Additive manufacturing (3D printing), photonics, laser material processing, ceramics, preceramic polymers, processing, two-photon polymerization, applied sciences, CAD design, optical fibers, cleanroom, programming, R&D

Education

PhD in Additive manufacturing with light
École polytechnique fédérale de Lausanne (EPFL), Switzerland
Advisor: Prof. Christophe Moser
Thesis: "Additive manufacturing of ceramics by two-photon lithography, volumetric 3D printing, and high-resolution endo-printing."

Master in Microsystems and Nanodevices
National Technical University of Athens, (NTUA) and
Institute of Electronic Structure and Laser (IESL), FORTH, Crete, Greece
Advisors: Dr. Stavros Pissadakis, Prof. Ioanna Zergioti
Master thesis: "Photonic devices based on Whispering-Gallery-Mode resonators wedged in microstructured optical fibers."

Bachelor in Physics
National and Kapodistrian University of Athens, (UOA), Greece
Semester Internship: Hellenic National Meteorological Service

Professional experience

École polytechnique fédérale de Lausanne (EPFL), Switzerland

- Additive manufacturing of ceramic microstructures by two- or single- photon polymerization of preceramic polymers.
- Research in building a fiber 3D-printer and improving the fidelity of 3D printed structures through a minimally invasive endo-printer.

Institute of Electronic Structure and Laser, Photonic Materials & Devices Laboratory, IESL FORTH

- Research in Whispering-Gallery-Mode resonators wedged or attached in microstructured optical fibers for sensing

Skills

Technical competences

- Light and slurry -based 3D printers
- Processing of 3D printing techniques
- Development of optical Setups for 3D printing
- Scanning Electron Microscopy
- Sputtering machine for gold deposition
- Atomic Force Microscopy
- Microwave plasma stripper

- Optical fibers
- Digital holography
- Micro-optics
- Spatial light modulators
- Material processing

Software

- Matlab
- Solidworks
- Origin
- ImageJ
- COMSOL
- Zemax
- Adobe Photoshop
- Adobe Illustrator
- Office Suite

Languages

- Greek (native)
- English (Advanced)
- French (Intermediate)
- Chinese (Beginner)

Articles

- *"3D printing smooth microstructures by two-photon polymerization through a GRIN multimode fiber and PSF engineering for fast microfabrication",* submitted to Additive Manufacturing journal, Elsevier.
- *"Tomographic Volumetric Additive Manufacturing of Silicon Oxycarbide Ceramics". Under review in: Advanced Engineering Materials, Wiley-VCH GmbH, Weinheim, 2021.*
- *"Additive micro-manufacturing of crack-free PDCs by two-photon polymerization of a single, low-shrinkage preceramic resin". Published in: Additive Manufacturing, Elsevier, October, 2020, Volume 35.*
- *"Multiple Light Coupling and Routing via a Microspherical Resonator Integrated in a T-Shaped Optical Fiber Configuration System". Published in: Micromachines, Multidisciplinary Digital Publishing Institute.*